Spring 2018

Microstructure prediction of severe plastic deformation manufacturing processes for metals

Ninggang Shen
University of Iowa

MICROSTRUCTURE PREDICTION OF SEVERE PLASTIC DEFORMATION MANUFACTURING PROCESSES FOR METALS

by

Ninggang Shen

A thesis submitted in partial fulfillment
of the requirements for the Doctor of Philosophy
degree in Mechanical Engineering in the
Graduate College of
The University of Iowa

May 2018

Thesis Supervisor: Assistant Professor Hongtao Ding

Graduate College
The University of Iowa
Iowa City, Iowa

CERTIFICATE OF APPROVAL

_____

PH.D. THESIS

_____

This is to certify that the Ph.D. thesis of

Ninggang Shen

has been approved by the Examining Committee for
the thesis requirement for the Doctor of Philosophy degree
in Mechanical Engineering at the May 2018 graduation.

Thesis Committee: _____
Hongtao Ding, Thesis Supervisor

_____
Christoph Beckermann

_____
Asghar Bhatti

_____
Kyung K. Choi

_____
H.S. Udaykumar

To my parents,
my wife Xin WEN, and our daughter Xiru

ACKNOWLEDGEMENTS

I would first like to express my full gratitude to my advisor, Prof. Hongtao Ding, for his guidance, encouragement, inspiration and care, for being a friend, for helping me shape, model and advance my professional career, for steering me to develop professional skills and mature personality. This work would not have been possible without his guidance or support. His overly enthusiasm and integral view on research has made a deep impact on me. He could not even realize how much I have learned from him. I am sincerely glad that I have come to be his student.

I would also like to thank Professors Beckermann, Bhatti, Choi, and Udaykumar for serving on this examination committee, who monitored my work and took effort in reading and providing me with valuable comments on this dissertation.

I would like to appreciate Dr. Wayne W. Cai for his supervision on the General Motors (GM) sponsored project in ultrasonic welding process modeling and mentorship on my National Science Foundation (NSF) internship at GM Global R&D Center. I appreciate his fatherly and scholarly manner in research and work. Additional thanks are also due to Drs. Teresa Rinker (GM), Thomas Stoughton (GM), Prof. Benxin Wu (Purdue University), and Prof. Jingjing Li (Pennsylvania State University), who always showed their excellent research and great dedication in our discussions. Thanks also goes to Dr. Zhengwen Pu and Prof. I.S. Jawahir from University of Kentucky for providing the experimental data of cryogenic machining. I am grateful to Thomas Moninger, Assistant Director for Central Microscopy Research Facility in the University of Iowa, for helping me with different microscopy testing and analyses.

I would also like to thank my colleagues at the Laser Materials Processing Lab in the University of Iowa, Avik Samanta, Qinghua 'Nicholas' Wang, and Timothy Heiderscheit, for providing such a stimulating and open environment for thinking and research.

I would like to thank National Science Foundation (grant EPS-1101284 and CMMI-1537512) for supporting this work, as well as the NSF 17-091 Dear Colleague Letter: Non-Academic Research Internships for Graduate Students (INTERN) Supplemental Funding for the internship at GM Global R&D Center. I gratefully acknowledge GM Global R&D for the financial and technical support that allowed me to augment my skill set and knowledge base by exposure to an industrial context.

None of these would have been possible without the unconditional love, understanding, and support of my family. I must express my very profound gratitude to my parents and parents-in-law for their constant love and always being supportive no matter what decisions I have made. Finally, but most importantly, I would like to acknowledge and thank my beloved wife, Xin, for her love, support, and the great happiness she has brought to my life.

ABSTRACT

The objective of the research presented in this thesis has been to develop a physics-based dislocation density-based numerical framework to simulate microstructure evolution in severe plastic deformation (SPD) manufacturing processes for different materials. Different mechanisms of microstructure evolution in SPD manufacturing processes were investigated and summarized for different materials under dynamic or high strain rates over a wide temperature range. Thorough literature reviews were performed to clarify discrepancies of the mechanism responsible for the formation of nanocrystalline structure in the machined surface layer under both low-temperature and high-temperature conditions.

Under this framework, metallo-thermo-mechanically (MTM) coupled finite element (FE) models were developed to predict the microstructure evolution during different SPD manufacturing processes. Different material flow stress responses were modeled subject to responsible plastic deformation mechanisms. These MTM coupled FE models successfully captured the microstructure evolution process for various materials subjected to multiple mechanisms.

Cellular automaton models were developed for SPD manufacturing processes under intermediate to high strain rates for the first time to simulate the microstructure evolution subjected to discontinuous dynamic recrystallization and thermally driven grain growth. The cellular automaton simulations revealed that the recrystallization process usually cannot be completed by the end of the plastic deformation under intermediate to high strain rates. The completion of the recrystallization process during the cooling stage after the plastic deformation process was modeled for the first time for SPD manufacturing processes at elevated temperatures.

PUBLIC ABSTRACT

The objective of the research presented in this thesis has been to develop a physics-based dislocation density-based numerical framework to simulate microstructure evolution in severe plastic deformation (SPD) manufacturing processes for different materials. Different mechanisms of microstructure evolution in SPD manufacturing processes were investigated and summarized for different materials under dynamic or high strain rates over a wide temperature range. Thorough literature reviews were performed to clarify discrepancies of the mechanism responsible for the formation of nanocrystalline structure in the machined surface layer under both low-temperature and high-temperature conditions.

Under this framework, metallo-thermo-mechanically (MTM) coupled finite element (FE) models were developed to predict the microstructure evolution during different SPD manufacturing processes. Different material flow stress responses were modeled subject to responsible plastic deformation mechanisms. These MTM coupled FE models successfully captured the microstructure evolution process for various materials subjected to multiple mechanisms.

Cellular automaton models were developed for SPD manufacturing processes under intermediate to high strain rates for the first time to simulate the microstructure evolution subjected to discontinuous dynamic recrystallization and thermally driven grain growth. The cellular automaton simulations revealed that the recrystallization process usually cannot be completed by the end of the plastic deformation under intermediate to high strain rates. The completion of the recrystallization process during the cooling stage after the plastic deformation process was modeled for the first time for SPD manufacturing processes at elevated temperatures.

TABLE OF CONTENTS

LIST OF TABLES

LIST OF FIGURES

CHAPTER 1.

INTRODUCTION

1.1 Rationale

Severe plastic deformation (SPD) usually refers to a group of metalworking techniques involving a complex stress state or a very high shear strain under quasi-static or low strain rates, e.g., equal channel angular processing (ECAP), high pressure torsion (HPT), accumulated roll bonding, and surface mechanical alteration treatment. During these processes, microstructures with a high dislocation density are usually formed, consisting of equiaxed ultra-fined grains (UFG) with a typical size of less than 500 nm or a nanocrystalline structure having a typical size of less than 100 nm [1]. During these SPD processes, mechanical deformation, heat transfer, and metallurgy all inherently couple together, leading to different states of microstructural alterations, which significantly affect the functionality and performance of manufactured products [2–7]. This strong coupling effect is often termed as metallo-thermo-mechanical (MTM) coupling for manufacturing processes [8–10], as illustrated in Figure 1.1 for a hardened steel machining example.

During the machining processes of hardened steels and other difficult-to-machine alloys, machine tools often induce large plastic strains (e.g., a shear strain of ~5-10) inside the chip as well as along the machined surface. The chip forms at a high strain rate, characteristically on the order of 10^5 s^{-1}, for typical cutting speeds of 100-300 m/min. A high temperature gradient also exists in the cutting zone, characterized by a rapid heating rate of 10^5-10^6 °C/s and a fast cooling rate of 10^3-10^4 °C/s. Because of these complex thermomechanical loading conditions, a strong SPD effect coupled with other

microstructure evolution mechanisms is induced on the machined surface, affecting final surface microstructure attributes and functional performances, including corrosion resistance, wear resistance, fatigue resistance, etc.

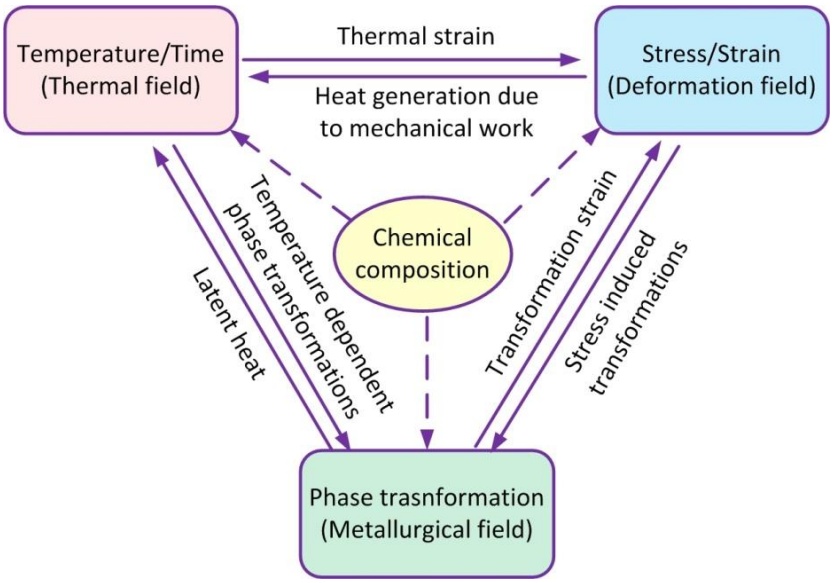

Figure 1.1 Metallo-thermo-mechanical coupling in cutting of steels [11].

A more comprehensive understanding of the MTM coupling effect will enable the process optimization to maintain a desired microstructure and ensure the requisite functionality of the component [12]. However, the MTM coupling effect is not well understood for ultrasonic welding and hard machining under intermediate strain rates (10^0-10^2 s^{-1}) or high strain rates (up to 10^6 s^{-1}), respectively. For these processes, complex thermomechanical process loading usually arise at a localized domain during a short time duration. Hence, it remains very difficult to experimentally study the MTM coupling effect for these manufacturing processes.

Predictive manufacturing process models based on numerical simulations have been used as an effective approach to gain fundamental insight into complicated material behavior during SPD processes. In the past two decades, finite element (FE)-based manufacturing process models have been developed to investigate various SPD processes, such as metal cutting and forming [13–16]. However, these conventional FE models usually focus on the simulation of macroscopic process variables, such as force, heat generation, deformation, and geometry. Generally, these state-of-the-art FE models lack the capability of (1) coupling mechanical deformation and heat transfer with metallurgy and (2) predicting the microstructure evolution during SPD processes.

Recently, more researchers have been interested in the development of numerical models to simulate microstructure evolution during machining processes, using phenomenological material models or empirical relationships to determine the final microstructural attributes, such as grain size and hardness [17–23]. A common shortcoming of these emerging models is that they often require costly calibration or post processing using experimental data to correct or improve model accuracy. These existing FE-based SPD process models are inadequate to capture the implicit, dynamic, non-equilibrium nature of SPD processes. Likewise, the process-microstructure relationship is not modeled in a coupled manner in existing FE-based cutting simulations as well.

This research aims to eliminate these deficiencies by tightly coupling high-fidelity sub-grid simulations within continuum process simulations to determine the microstructure at each process step using local conditions. In particular, the focus of this research effort is the development of a dislocation density-based numerical framework to predict microstructure evolution during ultrasonic welding and hard machining under

intermediate to high strain rates. Multiple microstructure evolution mechanisms, including mechanical deformation-induced grain refinement, discontinuous dynamic recrystallization, surface nanocrystallization, and white etching layer formation, are investigated for different metal alloys under various process conditions. Numerical models are developed for these SPD manufacturing processes to simulate the complex coupling of thermomechanical loadings and microstructure evolution.

This research constitutes the first known comprehensive attempt to systematically investigate microstructure evolution mechanisms during ultrasonic welding and hard machining. The technical focus of predictive relationship development between processing parameters, material composition, and resulting microstructure will greatly reduce experimental iterations and facilitate the design of experiments for optimal microstructure control. This new knowledge will contribute to a better fundamental understanding of manufacturing science, improved knowledge-driven manufacturing process planning, and more accurate prediction of a component's lifetime.

1.2 Mechanical Deformation-Induced Grain Refinement

In recent years, mechanical deformation-induced grain refinement has been extensively investigated for the manufacture of ultra-fine-grained metals by employing SPD processing techniques. Figure 1.2 qualitatively depicts the microstructure evolution mechanism subjected to mechanical deformation-induced grain refinement during a plane-strain orthogonal cutting process. Figure 1.2a shows equiaxed grains typically found in an annealed metal alloy material prior to cutting, which consists of loosely tangled dislocation structures. As the cutting process starts, new dislocations are

generated to accommodate the plastic strain exerted to this grain structure (Figure 1.2b). As the workpiece material enters the primary deformation zone, plastic strains drastically increase, and the dislocation cell structures are greatly elongated due to severe straining as shown in Figure 1.2c. New dislocations dramatically increase on the cell walls, and some are blocked by the subgrain boundaries. As the deformation continues, elongated subgrains break up, and are reoriented into ultrafine equiaxed grains as shown in Figure 1.2d.

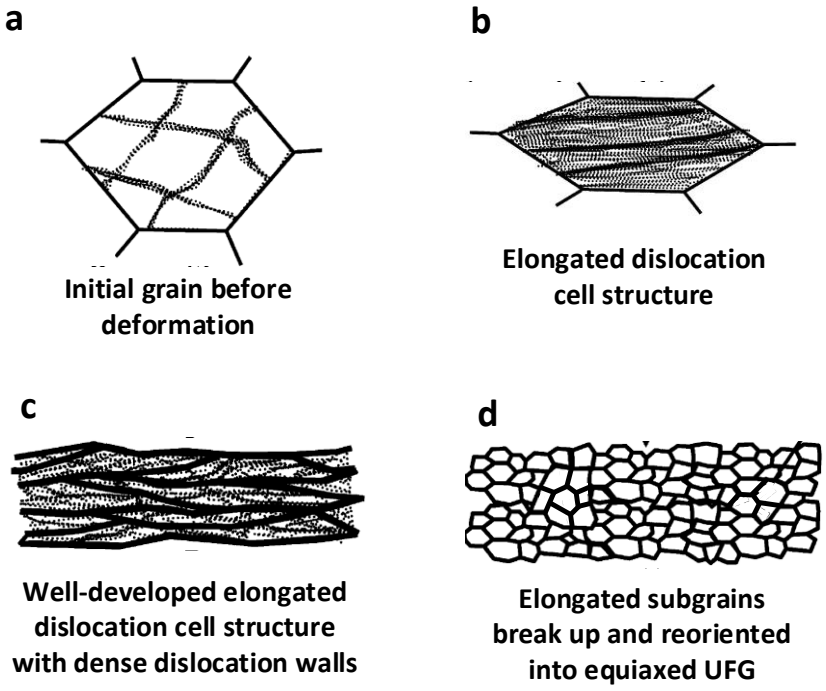

Figure 1.2 Schematic for the mechanical deformation-induced grain refinement mechanism. Figure is adopted from Ni and Alpas [24].

As a flexible and controllable SPD method for producing UFG microstructures, plane-strain orthogonal cutting has been experimentally studied for various polycrystalline metal alloys, such as aluminum alloys [25,26], copper [24,27,28], nickel-

based superalloys [27], steels [27], and commercially pure titanium [29]. In these experimental studies, to keep the cutting temperature low and suppress grain dynamic recovery, low cutting speeds, for example, 0.01 or 0.05 m/s, were usually applied for copper and aluminum alloys in these tests. The large-strain in the chip formation by machining has been generally used as a qualitative measure to the grain size change in the experimental results. However, experimentally observed relationship between strain and grain size in those resultant UFG microstructures usually cannot be simply extended to a different process condition or a different material.

To capture this mechanical deformation-induced grain refinement mechanism, dislocation density-based approaches have been applied for constitutive modeling of metals to couple the material dynamic response with the microstructure evolution during dynamic deformation processes. Estrin et al. [30] and Tóth et al. [31] presented a set of differential equations to evaluate the dislocation density evolution rates and applied the dislocation density-based material plasticity model for grain refinement prediction in the ECAP process of various materials, such as copper [32], aluminum [33] and IF (interstitial-free) steel [33,34]. Ding et al. [35,36] have adapted this plasticity model in the FE-based numerical analysis for orthogonal cutting. Accurate quantitative predictions have been achieved on the grain size and microstructure evolution of metal materials. As shown in Figure 1.3, the nucleation of dislocations due to deformation, annihilation of dislocations due to dynamic recovery, and interaction of dislocations between the dislocation cell interiors and cell walls were evaluated based on the deformation process state variables [37]. The dislocation density-based material plasticity model was compatible with the material constitutive models developed under various conditions of

strain, strain rate, and temperature. Their work was the first quantitative grain refinement model available in literature for plane-strain orthogonal cutting of metals to the authors' best knowledge. The dislocation density-based numerical approach was also applied for other SPD processes, such as hard turning [38], multi-pass cold rolling [39], and laser shock peening [40,41]. Recently, their dislocation density-based approach have been adapted by more researchers to predict microstructure evolution during machining of aluminum alloys, copper, steels, and titanium alloys [42–48]. A good capability of microstructure prediction was achieved using this approach.

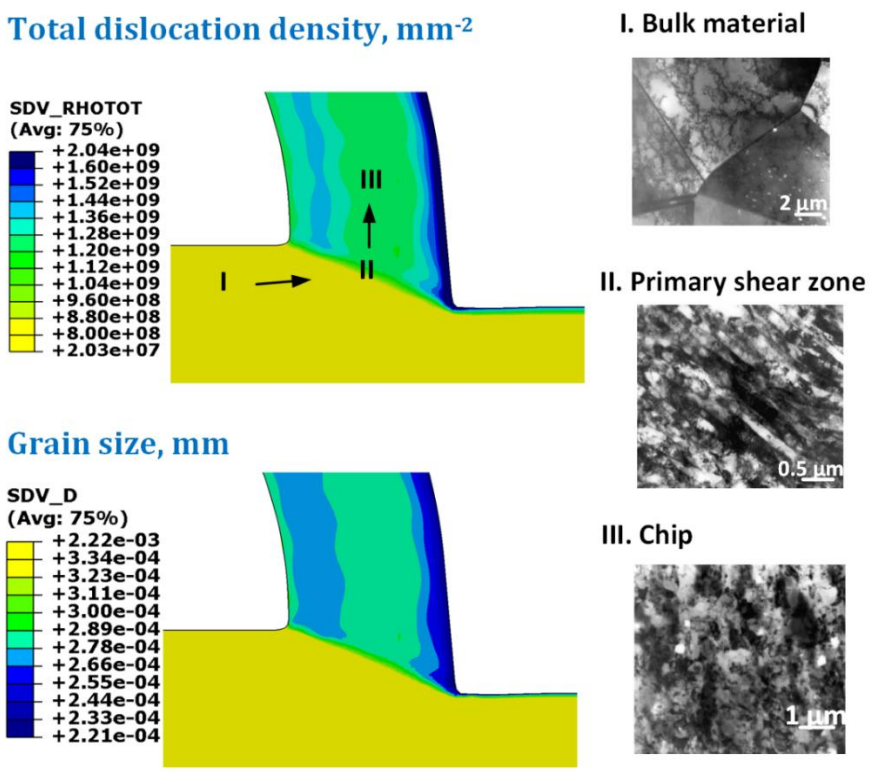

Figure 1.3 Predicted microstructure evolution in cutting of OFHC Cu. Figure is adopted from Ding et al. [35].

The existing dislocation density-based approach mainly focuses on the microstructure evolution dominated by dislocation dynamics. The effects of mechanical twins during SPD processes are usually not considered in the dislocation density-based models. Slip (dislocation) and twinning are the two basic mechanisms of plastic deformation. In particular, hexagonal close-packed (HCP) metal alloys are likely to form deformation twins when subject to large deformation strain [49–51]. Twinning can play a critical role for HCP magnesium (Mg) alloys subjected to SPD processes, particularly at low-temperature and high-strain-rate loading conditions. During cryogenic machining of Mg alloys, the cutting process temperature remains low due to cryogenic cooling, and a high strain rate is produced in the cutting zone due to the high cutting speed. In the following sections, the effects of deformation twins of Mg alloys are discussed.

Two material-dependent factors mainly contribute to the formation of twins for Mg alloys: the number of slip systems and stacking fault energy (SFE) [49,50]. Mg has a slip plane at {0001} and a slip direction of <1120>, which results in a total of three slip systems. Compared with face-centered cubic (FCC) metals such as copper, due to the lack of slip systems, Mg usually requires higher driven force or elevated temperature to activate the operation of non-basal systems [51]. Comparing with other HCP-structured metal alloys with a high SFE, twinning is more pronounced for Mg due to its lower SFE in the range of 60-78 mJ/m^2.

The formation of deformation twins can also be facilitated by high strain rates and low process temperatures [49–51]. At room temperature, a large amount of twinning lamellas are usually observed in Mg at the low strain stage of SPD processes [51,52], or in low-strained domain below the machined surface [52–54]. With a dynamic strain rate,

an increase of twinning has been observed at both room and elevated temperature [52,55]. Watanabe et al. [56] found the deformation of AZ31B Mg alloy at a high strain rate about 10^3 s^{-1} proceeds by plastic flow of both slip and twinning at the same time even at elevated temperatures.

The transition between slip and twinning during cryogenic machining also needs to be investigated. As plastic strain continues to accumulate, instead of deformation twinning, prismatic slip is found as the predominant deformation mechanism at room temperature with high strain rate greater than 10^3 s^{-1} [57–62]. The occurrence of prismatic slip maintains intergranular compatibility between deforming grains [57,58]. It also carries a large amount of the total strain, especially when basal planes are not favorably oriented for slip [57,60,61]. Figure 1.4 qualitatively depicts the microstructure evolution mechanism for HCP Mg alloys subjected to both slip and twinning during an SPD process. At the early stage of plastic deformation, deformation twins divide an initial coarse grain into finer twin lamellas. As the SPD process continues, the accumulated plastic strain activates additional dislocation slip systems, such as prismatic plane system and pyramidal plane system. These newly formed high-density dislocation arrays subdivide the twins into subgrains as shown in Figure 1.4e. Based on the above analysis, both twinning and slip response should be accounted for microstructure evolution modeling of Mg alloys during cryogenic machining.

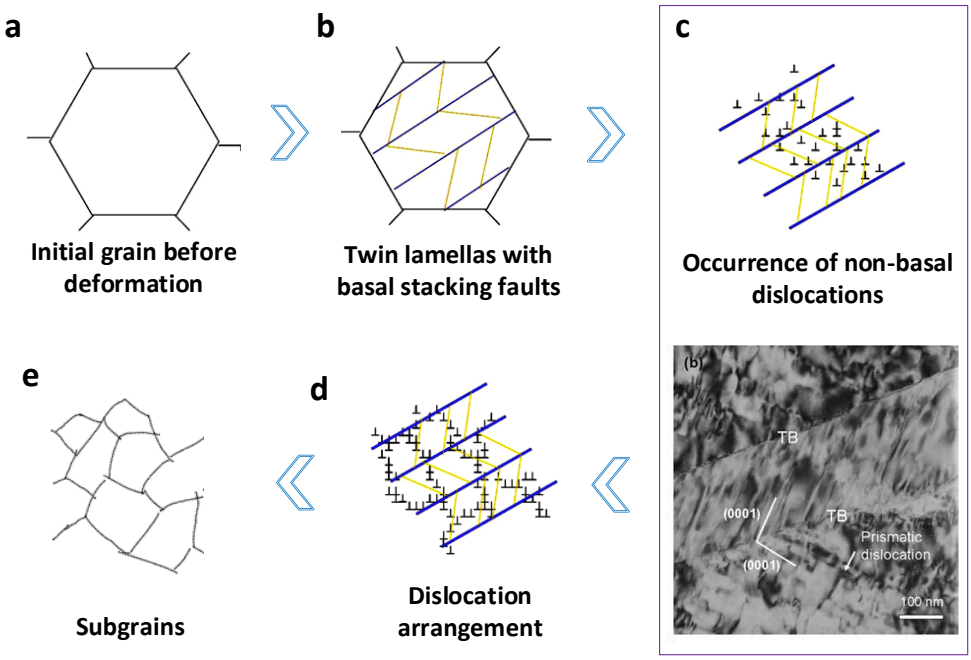

Figure 1.4 Schematic of the microstructure evolution mechanism for HCP Mg alloys subjected to both slip and twinning during an SPD process. Figure is adopted from Sun et al. [52].

In Chapter 3, a thorough literature review of experimental analysis was performed to elucidate the complex microstructure evolution mechanisms for the UFG layer formation during cryogenic machining of Mg alloys. A physics-based material model was developed for the first time to simulate the microstructure evolution during the cryogenic machining of Mg alloys by considering both slip and twinning response of the HCP Mg alloy.

1.3 Dynamic Recrystallization during SPD Processes

Dynamic recrystallization (DRX) is defined as a replacement process of deformed grain structure with newly nucleated and grown grains undergoing deformation [63]. DRX is a dominant material microstructure evolution mechanism during a warm or hot working process, during which the process temperature is elevated to above 40%~50% of the material melting point (0.4-0.5T_m) in Kelvin [64,65]. Dynamic recrystallization can occur in a slow and continuous manner for "continuous dynamic recrystallization" (cDRX), while "discontinuous dynamic recrystallization" (dDRX) occurs in a fast and discontinuous manner to metal alloys, during which nucleation of new grains occurs at the deformed grain boundaries and regions depleted of dislocations grow at the expense of regions full of dislocations. This research mainly focused on the effects of dDRX on microstructure evolution during fast SPD processes.

Metals that undergo dDRX have been extensively studied by hot working experiments under quasi-static and low strain rates conditions [63,66]. During the dDRX process, original microstructure will be eventually replaced by the recrystallized grains, and a unique flow stress behavior will be observed. As the onset of plastic deformation, dislocations are rapidly generated to accommodate the plastic strain, leading to an increase of flow stress. This stage is usually referred to the work hardening stage during plastic deformation. With the increase of plastic deformation, thermally activated dislocation annihilation process usually occurs simultaneously with the dislocation nucleation at elevated temperatures. This dislocation annihilation is usually referred to dynamic recovery, which decreases the rate of dislocation accumulation. As a result, the work hardening rate is decreased as well. When a critical dislocation density is reached,

fine equiaxed recrystallization nuclei are usually developed as dislocation-free crystallites on the boundary of the elongated dislocation cell structure. These nuclei start to grow by means of the long-range migration of boundaries, consuming the strain hardened microstructure. The driving force for the growth of such new grains is the stored energy associated with the dislocations and sub-boundaries produced during prior straining. Hence, these new grains produce softening and further decrease the work hardening rate until a clear stress peak is formed eventually. The flow stress then decreases with increasing strain until a steady-state level deformation is attained. The steady-state flow stress reflects the dynamic equilibrium between strain hardening and strain softening due to the formation of new grains and the associated grain boundary migration. Figure 1.5 depicts the aforementioned flow stress behavior and microstructure evolution mechanism subjected to discontinuous dynamic recrystallization. Based on these experimental findings, it can be concluded that dDRX is a dynamic progressive microstructure evolution process coupled with simultaneous dislocation evolution under the complex thermomechanical loadings during SPD processes.

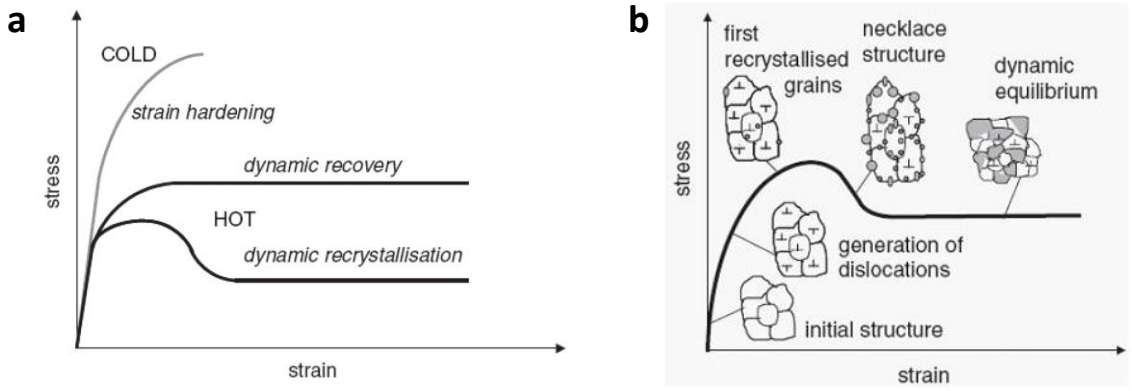

Figure 1.5 Schematic of flow stress behavior and microstructure evolution mechanism subjected to discontinuous dynamic recrystallization. Figure is adopted from Quan [67].

Recently, more numerical work starts to emerge to simulate the microstructural changes during machining processes, assuming dDRX as the dominant grain refinement mechanism [17–23]. Phenomenological material constitutive models, e.g., Johnson-Cook (JC) model, have been applied in these finite element-based cutting process simulations, during which work materials are subjected to large-strain, high-strain rate, and high-heating/cooling rate loading conditions. Empirical relationships, e.g., Zener–Hollomon equation, were employed to predict the final grain size after cutting. Critical model parameters of Zener–Hollomon equation required a large amount of calibration efforts to improve or correct the simulation results using measurement data of microstructural attributes. The other empirical process-microstructure relationship in the form of Hall–Petch equation was often employed to predict the final material microhardness. However, these empirical correlations of final grain size and microhardness presented in the previous researches [17–23] were established based on the calibrations from numerous experimental measurements. They generally did not consider the dynamic dislocation evolution during dynamic recrystallization subjected to complex thermomechanical process loading conditions.

Yanagimoto et al. [68] developed a kinetic model to simulate the progressive dDRX procedure in hot forming by considering the volume fraction of dDRX, X_{DRX}. In this kinetics model, the calculation of X_{DRX} was determined using the proces time. Multiple alternative equations were developed to improve Yanagimoto's kinetics model by calculating X_{DRX} using true plastic strain [68–74]. This kind of DRX kinetics models have been extensively applied in numerous simulation work for hot working processes

under quasi-static strain rates in the range of 10^{-4} ~10^{-1} s^{-1}. To capture the flow stress behavior for work hardening and low-temperature creep, Kocks and Mecking developed a phenomenological material constitutive model using dislocation density as a single parameter [75,76]. In the most recent year, researchers attempted to simulate the dislocation density evolution and DRX procedure during machining operations by applying the Kocks-Meching material constitutive model and improved Yanagimoto's DRX kinetics model to finite element cutting process simulation [42–44,47].

Neither Kocks-Meching model nor improved Yanagimoto's DRX kinetics model is suitable for modeling ultrasonic welding and hard machining under intermediate strain rates (10^{0}-10^{2} s^{-1}) or high strain rates (up to 10^{6} s^{-1}), respectively. To adapt the Kocks-Meching model for high strain rate metal cutting process, Liu et al. [44] introduced a dislocation drag term to increase the strain rate sensitivity under high strain rates (10^{5} ~10^{6} s^{-1}). However, considerable calibration efforts were still needed to apply this model for a different material under a different process condition. Moreover, the DRX kinetics model were still not coupled with dislocation density evolution in Liu's work. The onset of DRX in these kinetics models were associated with a phenomenological critical plastic strain, rather than a critical dislocation density.

In Chapter 2, the final bulk work material microstructures are simulated using the improved Yanagimoto's kinetic model of discontinuous dynamic recrystallization during ultrasonic welding under intermediate dynamic strain rates and high temperatures. In Chapter 5, a new dislocation density-based Cellular Automaton (CA) model was developed for the first time to simulate the microstructure evolution of bulk materials during the dDRX-dominated ultrasonic welding process. Multiple mechanisms of

microstructure evolution were coupled in the CA model including severe plastic deformation, dynamic recovery, discontinuous dynamic recrystallization, and thermally driven grain growth.

1.4 Nanocrystalline White Etching Layer Formation during SPD Processes

A surface layer subjected to undesired microstructure changes has been widely observed on the high-speed machined surface of difficult-to-machine materials, e.g. hardened steels [77–86], Ni-based superalloys [87–96], and Ti-6Al-4V alloy [97–102]. This undesirable microstructure is often termed as "white etching layer" (WEL) because it appears to be featureless and white when it is viewed under an optical microscope as shown in Figure 1.6. The formation of WEL has been a great interest in the past decades. Griffiths [103] attributes white layer formation to one or more of the following possible mechanisms: (1) rapid heating and quenching, which results in dynamic phase transformation, (2) severe plastic deformation, which produces a refined homogeneous structure, and (3) surface reaction with the environment, e.g., nitriding. Jawahir et al. [83] argued that metallurgical transformation occurs in the chip or on the workpiece machined surface due to intense, localized and rapid thermo-mechanical working during hard turning. Ramesh et al. [84] suggested that white layers produced by hard turning of bearing steel at low-to-moderate cutting speeds are largely due to the grain refinement induced by SPD, whereas white layer formation at high cutting speeds is mainly due to thermally driven phase transformation. Studies of the drilling of a commercial bearing steel (type SUJ2) in a tempered martensitic structure by Todaka et al. [85] showed that the white layers formed on the machined surfaces were composed of refined equiaxed

nanocrystalline grains. They stipulated that the ultrafine structure layer on the machined surface is produced by both thermally- and deformation-driven phase transformations together with a large strain gradient and high strain rates. Li et al. [86] showed that both cutting parameters and initial workpiece hardness play vital roles in the white layer formation. Burns et al. [77,78] have reported that for carbon steels, e.g. AISI 1045 and 1075 steels, the phase transformation drastically changed the material constitutive behaviors at high temperatures. They also indicated that the constitutive models developed without the phase change effect are usually not suitable for modeling of cutting of steel at high cutting speeds. Hence, the white layer formation in machining of steels should be considered as a coupled effect of dynamic phase transformation and grain refinement process, although there are still different understandings of the mechanism of its formation.

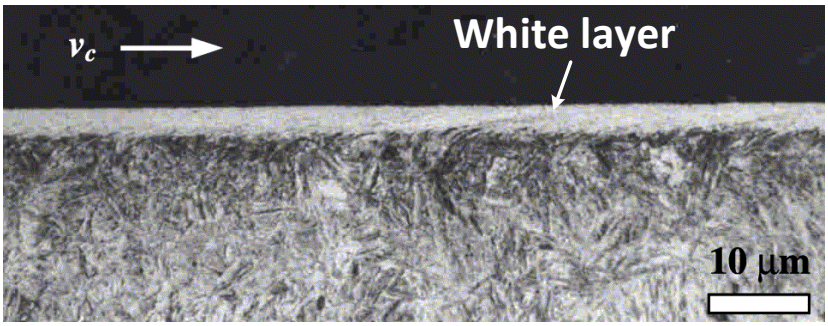

Figure 1.6 Optical micrograph of a white layer in a sectioned and etched surface of BS 817M40 steel of 52 HRC. Figure is adopted from Barry and Byrne [80].

During the last decades, researchers have become more interested in numerical modeling the development of the white layer formation during hard machining processes of steels. However, most of these researches focused on the understanding of dynamic

phase transformation effects on the white layer formation. Chou and Evans [79] used an analytical thermal modeling approach to predict white layer formation due to phase transformation in hard turning of AISI 52100 steel workpieces. Shi and Liu [104] developed a two-dimensional (2D) FE analysis to simulate orthogonal cutting of hardened AISI 52100 steel using ABAQUS, and used the predicted temperature to analyze the phase transformation in the chips. Fast re-austenitization and martensitic transformation were facilitated by the high temperatures in the secondary shear zone, whereas the other parts of the chips retain the original tempered martensitic structure. Umbrello et al. [105,106] developed a 2D FE framework to predict white/dark layer thickness due to quenching/tempering and surface hardness in orthogonal cutting of hardened AISI 52100 steel. Ramesh and Melkote [107] applied a kinetics model of phase transformation to 2D FE simulations of orthogonal cutting of hardened AISI 52100 steel using ABAQUS. Their simulations attempted to predict the white layer thickness induced by the phase transformation due to thermal, stress, and strain effects in a surface layer. However, these aforementioned models did not consider the feedback of phase change on the material thermal, elastic and constitutive viscoplastic behaviors in cutting.

Nanocrystalline structures observed in the white layer during machining of difficult-to-machine materials have emerged as a research interest in the metal cutting research community in the last a few years. Multiple finite element-based cutting process models were developed to predict the surface nanocrystallization [19,22,23,47,108–114]. These FE cutting simulations assumed dynamic recrystallization was as the driving microstructure evolution mechanism to form the nanocrystalline and UFG structures in the machined surface. Phenomenological material constitutive models combined with

empirical process-microstructure relationships, such as Zener–Hollomon and Hall-Patch equations, were often used to predict the final grain size and microhardness. The limitations of their modeling approaches are thoroughly discussed in Section 1.3. Due to these limitations, the numerical modeling approach based on empirical process-microstructure relationships are considered inappropriate to model the microstructure evolution and white layer formation during hard machining of difficult-to-machine materials.

Buchkremer and Klocke [115] developed a numerical approach based on the thermodynamic potential change to predict the nanocrystalline structure formation in the machined surface of steel AISI 4140 during orthogonal cutting. The thermodynamic potential was determined by plastic work, heat dissipation, heat conduction, grain interface energy, and entropy evolution. Based on the irreversibility during the machining process, the DRX initiation and kinetics were simulated during the cutting simulation. To author's best knowledge, this modeling work is the first attempt in literature using the thermodynamics approach to simulate surface nanocrystallization during machining operation. However, this method implemented an empirical relationship, i.e., a critical DRX initiation strain calibrated using experimental data, to model DRX kinetics. In addition, this method did not consider the dynamic evolution of dislocations under the complex thermomechanical process loading conditions.

Controversies still exist in literature about surface nanocrystallization mechanisms during machining processes. Although dynamic recrystallization was considered as the microstructure evolution mechanism in all the aforementioned work [19,22,23,47,108–115], numerous experimental data have shown that dynamic recrystallization is not a

major microstructure alteration mechanism for machining of difficult-to-machine metal alloys, e.g., Ni-based superalloys [87–96]. These experimental researches indicated that the surface nanocrystallization is governed by a combined effect of many mechanisms, including thermally driven phase transformation and mechanical refinement due to severe plastic deformation.

More contradicting experimental results have been reported for hard machining of steels. With very limited experimental data (slightly coarser structure and several larger cells in BS 817M40 steel), Barry and Byrne [80] argued for the possible occurrence of DRX, which may have happened to steels at elevated cutting process temperatures due to a decrease in the stacking fault energy. They also concluded that conventional discontinuous dynamic recrystallization is unlikely to occur in the machined surface during rapid machining operations. Li et al. [86,116–118] investigated the surface microstructure for a drilled hole in carbon steels. They concluded that the formation of nanocrystalline layer in the drilled hole surface should be attributed to a combined effect of severe plastic deformation and dynamic phase transformation with a large strain gradient and a high strain rate.

For steels, the formation of nanocrystalline white layers has been achieved in many other SPD processes, such as adiabatic shear band formation [119–123], sliding wear [124], ultrasonic or air blast shot peening [117,125], sand blasting [126], ball milling [127], laser shock peening [128–133], HPT and ECAP [134–138]. These experimental researches investigated the nanocrystalline formation over a wide range of process loading conditions: strain rate in the range of 10^{-1}-10^{7} s^{-1}, process temperature from cryogenic temperature to 80% of the melting point (in Kelvin), and process time

duration from tens of microseconds to several hours. No clear evidence of recrystallized grains was found in any of these researches to support the occurrence of dynamic recrystallization.

To advance the manufacturing science in nanocrystalline white layer formation process, an extensive review was conducted in Chapter 4 to categorize and analyze the important experimental data and substantial evidence available in literature. A metallo-thermo-mechanically coupled framework was developed in this research extending from the work of Ding and Shin [11,38] to consider the coupled effects of deformation-driven grain refinement and thermally driven dynamic phase transformation on the formation of nanocrystalline white layer during machining. Important microstructural attitudes and cutting process variables were solved simultaneously using this model.

1.5 Research Objectives

The primary objective of the research effort as presented herein is the development of a dislocation density-based numerical framework to simulate multiple microstructure evolution mechanisms during SPD manufacturing processes. Under his framework, physics-based MTM coupled process simulations are performed to model the complex coupling of thermomechanical loading and microstructure evolution under intermediate to high strain rate SPD processes. The specific research tasks conducted are summarized as follows:

- In Chapter 2, a three-dimensional metallo-thermo-mechanically coupled finite element model is developed to capture the effect of welding time duration on the

microstructure evolution during ultrasonic welding. A phenomenological kinetic model of dDRX is implemented to predict welding joint microstructure.

- In Chapter 3, a physics-based material model is developed to simulate the microstructure evolution during cryogenic machining of Mg alloys by considering both slip and twinning responses. This material model is employed to simulate the enhanced surface integrity of AZ31B Mg alloy by cryogenic machining.
- In Chapter 4, a new dislocation density-based grain refinement model is developed to capture the surface nanocrystallization and white layer formation during hard drilling of steels.
- In Chapter 5, a new dislocation density-based cellular automaton model is developed to simulate the microstructure evolution of bulk materials during the dDRX-dominated SPD processes.

CHAPTER 2.

DYNAMIC RECRYSTALLIZATION IN ULTRASONIC WELDING

Ultrasonic welding (UW) of metals is a process characterized by intermediate dynamic strain rates (10^2~10^3 s^{-1}) [139] and high temperatures (0.4-0.6T_m) [140,141]. UW presents a typical example of the microstructure evolution governed by discontinuous dynamic recrystallization and grain growth. In this chapter, a three-dimensional (3D) metallo-thermo-mechanically coupled FE model is developed for the first time to capture the effect of welding time duration on microstructure evolution in the ultrasonic spot welding of Cu batter tabs. Actual knurl patterns were modeled for the first time to simulate the large deformation occurring in the weld zone during ultrasonic spot welding. The material constitutive model considers cyclic plasticity, thermal softening, and acoustic softening. A phenomenological dynamic recrystallization kinetics model is implemented using a post-processing user-defined subroutine to model the microstructure evolution governed by dynamic recrystallization in the UW process.

2.1 Experimental Analysis of Microstructure Alterations in Ultrasonic Welding

Ultrasonic welding has been applied as a practical and efficient solution for joining of thin malleable metals such as aluminum, and copper due to the virtues of low power consumption, rapid solid-state joining and environment friendliness [142]. In this study, the microstructure alterations induced by UW were carefully examined near the joint interfaces of two C11000 Cu (99.9% pure) sheets. S.S. Lee et al. [143] conducted these ultrasonic spot welding experiments for joining the copper tab-copper bus of automotive battery cells using an AmTech Ultraweld® L-20 high power welder with a

maximum output electric power of 4 kW. The top and bottom sheets were 0.4 and 1 mm in thickness, respectively. The bottom sheet was plated by a thin Ni layer (~3 μm thick). The ultrasonic vibration was implemented in the workpiece transverse direction with an amplitude of 30 μm at 20 kHz frequency. The clamping force was applied along the vertical direction and varied from 40 to 60 psi. Multiple experiments were performed for different welding time from 0.2 to 1.0 sec. Different knurl and anvil patterns were applied in their experiments. The experimental parameters were given in Table 2.1.

Table 2.1 Experimental conditions [143].

Materials	C11000 Cu (tab) Ni-plated C11000 Cu (bus)
Coupon thickness (mm)	0.4 mm (tab) 1 mm (bus)
Load (psi)	40, 50, 60
Vibration amplitude (μm)	30
Frequency (kHz)	20
Welding time (sec)	0.2, 0.4 0.6, 0.8, 1.0

The microstructure alterations are shown in Figure 2.1, which were obtained after ultrasonic spot welding under a clamping pressure of 50 psi with varying welding time durations. The as-received sheets were rolled and annealed before the welding experiments, which had strain-free grains for both top and bottom coupons as shown in Figure 2.1a. It can be recognized that the material microstructure underwent different evolution routes as the welding time increased. For a short welding time of 0.2 sec, a great amount of elongated grains can be seen in Figure 2.1b on both side of the joint interface. As the welding time increased to 0.4 sec, the elongated grains became dissolved, and newly formed strain-free-like fine grains can be seen in Figure 2.1c.

Similar microstructure with newly-formed fine grains near the weld interface was also observed after a 0.3 sec ultrasonic spot welding of aluminum alloy 6111 under a similar ultrasonic loading condition [144]. In Figure 2.1d, fine equiaxed recrystallized grains were formed with very clear grain boundaries in most area of the specimen cross-section after 0.6 sec welding. As the welding time increased to 0.8-1.0 sec, coarse grains were mainly seen in the specimens as shown in Figure 2.1e-f. In addition, a uniform microstructure was formed under these two conditions, while the difference across the weld interface was obvious for the shorter welding durations.

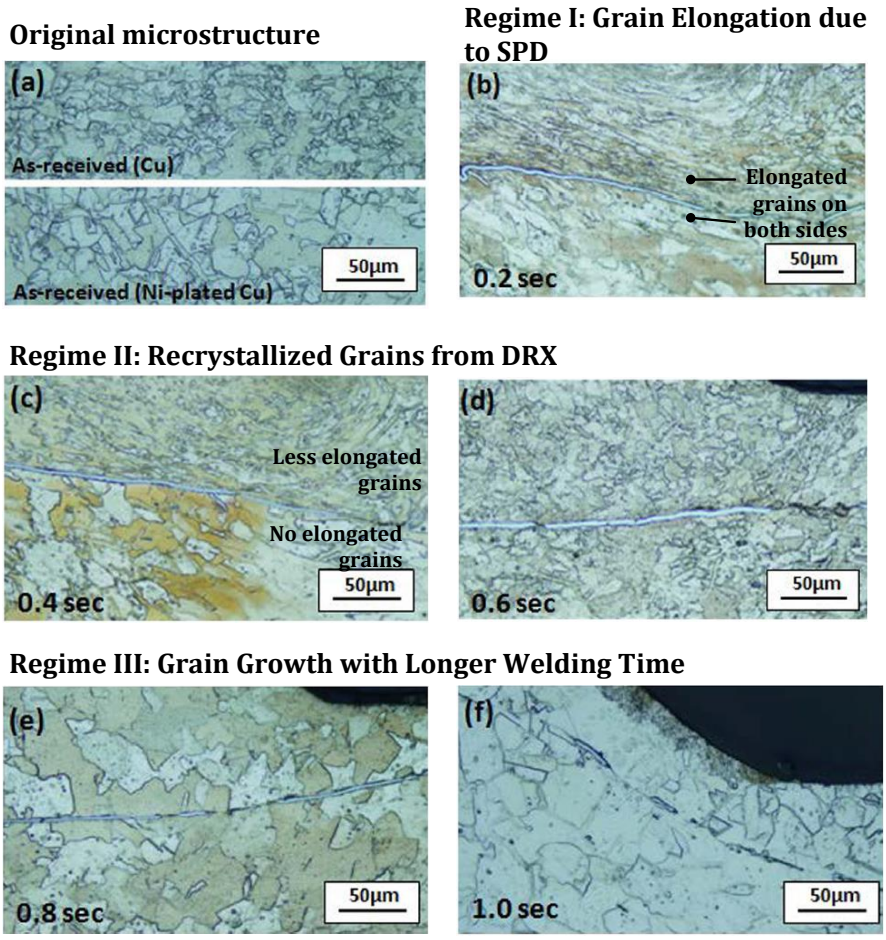

Figure 2.1 Microstructure after various welding time durations: (a) original microstructure before welding; (b) 0.2 sec; (c) 0.4 sec; (d) 0.6 sec; (e) 0.8 sec; (f) 1.0 sec. The original images were adopted from S. S. Lee et al. [143].

The grain size was measured separately for the top and bottom coupons using the optical micrographs for all the specimens. Figure 2.2 shows the measured average grain size from both sides of the weld line. The grain size of the as-received material was also measured: finer grains of 7.5 µm were observed in the thinner top coupon, while the thicker bottom coupon had a greater grain size of 12.5 µm. Significant grain refinement was observed after 0.2 sec welding. After a welding time of 0.4-0.6 sec, the grain size of about 10 µm was obtained. As the welding time increased to above 0.8 sec, significant grain growth to 30 µm occurred. After welding time of 0.4 sec, a small grain size of 7.6 µm was measured in the top coupon, while a big grain size of 11.6 µm was found in the bottom coupon. However, this difference in grain size between the top and bottom coupons started to diminish during grain growth under a longer welding time duration.

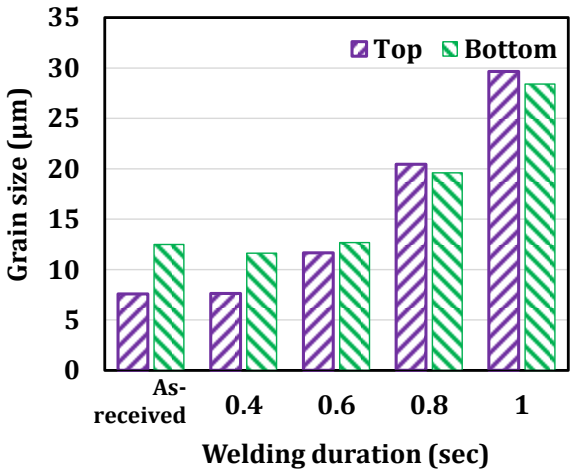

Figure 2.2 Grain size measurement.

Figure 2.3 shows microhardness at different locations on the cross-sectioned of weld joints from these experiments. The micro-indentation hardness tests were performed on the yellow spots. As labeled in Figure 2.3, valley is denoted as the more plastically deformed domain under the tip of the knurling tool, while the peak is the less deformed domain. Significant hardness increases can be observed for specimens made from a short welding time duration of 0.2 sec, especially at the valleys. As welding time duration increased from 0.2 sec to 1 sec, the microhardness at the valleys drastically decreased. It became even lower than the original value, when welding time duration increased to 1 sec. Figure 2.3 also shows the microhardness of weld joint varied at different locations due to different plastic deformation. For a short welding time duration (less than 0.4 sec), the more deformed valley has a much higher microhardness than that of the peaks. However, as the welding time increased, the difference in microhardness between the more and less deformed domains was significantly reduced or even diminished. The microhardness change was caused by the combined effect of the welding time, severe plastic deformation as well as microstructural evolution during ultrasonic welding.

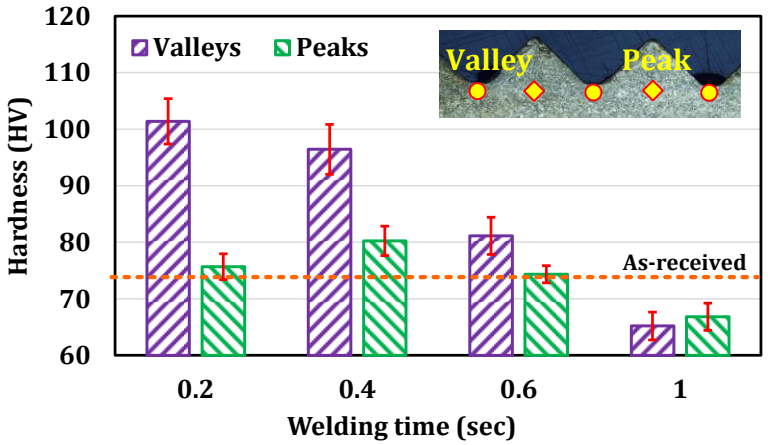

Figure 2.3 Hardness measurement of the joints at different locations with different welding durations.

2.2 Literature Review of Ultrasonic Welding Process Characterization and Modeling

Considerable research efforts have been devoted to characterizing the thermal field in the weld zone. The thermal contact conductance between thin metal sheets was determined as a function of contact pressure [145]. The real-time temperature and heat flux change have been measured and monitored near the weld zone using thin-film thermocouples [140] and thin-film micro-sensors [141]. Different weld formations were studied for various welding time durations from 0.6 sec to 1.5 sec. Based on the history of heat flux change rate, Li et al. [141] proposed a bonding mechanism for ultrasonic welding consisting of three continuous stages within one operation, which were firstly friction heating, then bonding by plastic work, and finally diffusion bonding.

Ultrasonic loading often leads to a significant softening phenomenon. The softening effect during ultrasonic spot welding is considered in two main mechanisms of thermal softening and acoustic softening. Thermal softening is attributed to the frictional heat generation from the high frequency vibration. The thermal energy is uniformly absorbed by the metal material. The acoustic softening contributes more on the flow stress reduction. The acoustic energy generated by ultrasonic sonotrode is transmitted to the metal and locally absorbed at defected crystal lattice, e.g. vacancies, dislocations and grain boundaries [146]. As a result, the activation energy of the dislocation line movement is considerably reduced [147]. The increased mobility of dislocations drastically attenuates the work-hardening, so flow stress can be extremely reduced.

Numerical modeling studies have been attempted to model the thermomechanical coupling effect during ultrasonic spot welding. Elangovan et al. [148] developed a two-dimensional finite element model for ultrasonic welding of dissimilar materials. In their

model, the effective heat generation terms were adopted from a previous study [149] for modeling heat generation due to deformation and friction under ultrasonic vibration. D. Lee et al. [150] developed a three-dimensional thermomechanical FE model and used a combined explicit/implicit multi-step numerical approach to predict ultrasonic spot welding of multi-sheet dissimilar materials (Al and Cu). However, the acoustic softening effect on material flow stress under ultrasonic loading was not considered in these previous studies.

The acoustic softening effect in the combined isotropic/kinematic hardening model under cyclic loading was considered by a material phenomenological constitutive model developed by Siddiq and Ghassemieh [151]. This model was successfully implemented in a 3D thermomechanical FE model for an ultrasonic seam welding process of Al ally 6061 using a sonotrode with smooth cylindrical surface. The temperature-dependent friction coefficient was calibrated and applied to predict the frictional heat generation under ultrasonic vibration. Siddiq and Ghassemieh [152] applied this numerical approach to model ultrasonic seam welding of Al ally 3003 and investigated the effects of various process parameters, such as applied load, ultrasonic vibration amplitude, and tool velocity, on weld material response. Siddiq and Sayed [153] further proposed a micromechanics-based crystal plasticity model by incorporating the phenomenological acoustic softening term and simulated the ultrasonic assisted deformation of both single crystalline and polycrystalline Al materials. With this model development, the work material textural change was simulated for ultrasonic consolidation at sub-micron scale [154].

Different from ultrasonic seam welding using a smooth cylindrical sonotrode, for ultrasonic spot welding of battery tabs considered in this study, a sonotrode and an anvil with diamond knurl patterns were used to significantly enhance the welding process capability. During the process, weld forms from compression and ultrasonic in-plane sliding of the diamond knurling tool, which induces severe plastic deformation in the work material. Experimental results of ultrasonic spot welding from S. S. Lee et al. [143] showed complex coupling effects among mechanical deformation, heat transfer, and microstructure change for various welding time durations. Their study revealed the material microstructure underwent different evolution routes with varying thermal and deformation histories. There is a great challenge in modeling such a metallo-thermo-mechanical coupled process under ultrasonic vibration. The available numerical approaches in literature are not capable to simulate the complex weld formation and microstructural evolution for the ultrasonic spot welding process.

2.3 Modeling of DRX and Grain Growth

A kinetic model was developed to capture the microstructural evolution during a warm/hot deformation process. The progress of DRX is characterized as the change of the volume fraction of DRX [68]. The DRX kinetic model is defined by [155]:

$$\varepsilon_c = a_2 \varepsilon_p \tag{2-1}$$

$$\varepsilon_p = a_1 d_0^{n_1} \dot{\varepsilon}^{m_1} \exp\left(\frac{Q_1}{RT}\right) \tag{2-2}$$

$$\varepsilon_{0.5} = a_5 d_o \dot{\varepsilon}^{m_5} exp\left(\frac{Q_5}{RT}\right) \tag{2-3}$$

$$X_{DRX} = 1 - \exp\left[-\beta_d \left(\frac{\varepsilon}{\varepsilon_{0.5}}\right)^{k_d}\right] \quad (2\text{-}4)$$

where ε_c is the critical strain for the onset of DRX, ε_p is the peak stress strain corresponding to the maximum flow stress, $\varepsilon_{0.5}$ denotes the strain at 50% recrystallization, d_o is the initial grain size, T is the process temperature in K, and X_{DRX} is the volume fraction of DRX. R is the ideal gas constant of 8.314 J/mol·K. β_d, and k_d are material constants. a_i, n_i, and m_i (i = 1, 2, …, 9) are material constants in each equation, and Q_i is a modified activation energy.

During the recrystallization, the averaged grain size (d) after DRX can be predicted by a mixture rule:

$$d = d_o - (d_o - d_{DRX})X_{DRX} \quad (2\text{-}5)$$

$$d_{DRX} = a_8 d_o \dot{\varepsilon}^{m_8} exp\left(\frac{Q_8}{RT}\right) \quad (2\text{-}6)$$

where d_{DRX} is the predicted grain size after DRX. The initial grain size d_o was assumed uniformly distributed in the coupons.

As recrystallization completes, grain growth would take place to reduce the grain boundary area per unit volume if the temperature is higher than the grain growth starting temperature [156]. Grain growth was considered to end as temperature dropped during the cooling step. The final grain size due to grain growth, d_g, is given by:

$$d_g = \left[{d_0}^{m_9} + a_9 t \cdot \exp\left(\frac{Q_9}{RT}\right)\right]^{1/m} \quad (2\text{-}7)$$

where t is the time duration for temperature above grain growth starting temperature, which also includes the time duration during the cooling stage. The relationship between

hardness and average grain size after welding is represented by Hall-Petch equation [157]:

$$H = H_o + kd^{-\frac{1}{2}} \quad (2\text{-}8)$$

where H is the microhardness of the material, H_o and k are material constants determined from the relationship of measured grain size and hardness. All the aforementioned material constants were calibrated based on the previously reported experimental results [143,158]. These values are listed in Table 2.2. Other necessary mechanical and physical properties of copper are given in Table 2.4.

Table 2.2 Model parameters to predict microstructure evolution and microhardness.

β_d	k_d	a_1	n_1	m_1	a_2	Q_1 (kJ/mol)	Q_5 (kJ/mol)	Q_8 (kJ/mol)
0.72	4.1	0.0003	1	0.1029	0.81	20.27	15.39	-44.33
a_5	m_5	a_8	m_8	a_9	m_9	H_o (HV)	Q_9 (kJ/mol)	k (HV$\sqrt{m}$)
0.0011	0.0781	711.45	0.15	25.29	-0.225	56.1	4.027	0.0487

Table 2.3 Mechanical and Physical Properties for Pure Cu [159].

Property	**Value**
Density (kg/m^3)	8890
Young's modulus (GPa)	115
Poisson's ratio	0.33
Melting point (°C)	1083
Thermal conductivity (W/m·°C)	391
Heat Capacity (J/Kg/°C)	385
Thermal expansion (μm/m·°C)	17

2.4 Flow Stress Modeling under Ultrasonic Loading

Ultrasonic welding involves high-frequency cyclic loading, thermal effect at the interface and ultrasonic effect due to ultrasonic vibration. Therefore, flow stress should be expressed in combined effect of all three phenomena. The basic constitutive equations for cyclic plasticity model were adopted from uniaxial loading. The total strain is the sum of elastic and plastic strain tensor:

$$\underline{\varepsilon} = \underline{\varepsilon}^{el} + \underline{\varepsilon}^{pl} \tag{2-9}$$

Flow stresses at any step of the simulation are calculated using the elastic stress strain relation:

$$\underline{\sigma} = \boldsymbol{D_{el}}\underline{\varepsilon}^{el} = \boldsymbol{D_{el}}\left(\underline{\varepsilon} - \underline{\varepsilon}^{pl}\right) \tag{2-10}$$

where $\boldsymbol{D_{el}}$ is the elasticity tensor. The yield surface is defined by modified Chaboche model, which is considered more accurate for cyclic loading condition [160].

$$\mathrm{F} = \left|\underline{\sigma} - \underline{\alpha}\right| = \sigma_0 + R \tag{2-11}$$

where σ_0 is initial yield stress, $\underline{\alpha}$ is the term related to back stress tensor due to kinematic hardening, and R is the term related to isotropic hardening. The plastic strain during deformation process is given by

$$d\underline{\varepsilon}^{pl} = d\lambda \frac{\partial F}{\partial \underline{\sigma}} \tag{2-12}$$

where $d\lambda$ is plastic multiplier which satisfies the following Kuhn-Tucker type consistency conditions.

$$F \leq 0;\ d\lambda \geq 0;\ d\lambda \cdot F \cong 0 \tag{2-13}$$

The expansion of yield surface due to isotropic hardening can be expressed as an exponential function of accumulated plastic strain [154]:

$$R = Q(1 - e^{-b\bar{\varepsilon}^{pl}}) \tag{2-14}$$

where Q and b are material constants. Q is the maximum change of yield surface due to isotropic hardening and b is the rate at which yield surface changes with accumulated equivalent plastic strain $\bar{\varepsilon}^{pl}$. For nonlinear kinematic hardening, the rate of back stress ($\dot{\underline{\alpha}}$) is given by

$$\dot{\underline{\alpha}} = C\frac{1}{\sigma_0}\left(\underline{\sigma} - \underline{\alpha}\right)\dot{\bar{\varepsilon}}^{pl} - \gamma\underline{\alpha}\dot{\bar{\varepsilon}}^{pl} \tag{2-15}$$

where C and γ are material constants from cyclic testing. C stands for the kinematic shift of yield surface and γ stands for the rate at which saturation value of kinematic hardening decreases with increasing plastic strain. $\sigma_0 = \sigma_y + R$, where σ_y is the yield stress for zero plastic strain. The back stress can be integrated from Eq. 7 for uniaxial case:

$$\alpha = \frac{C}{\gamma}\left(1 - e^{-\gamma\bar{\varepsilon}^{pl}}\right) + \alpha_1 e^{-\gamma\bar{\varepsilon}^{pl}} \tag{2-16}$$

where α_1 is obtained from stabilized cycle and is given by $\alpha_1 = \sigma_1 - \sigma_s$ with σ_1 is the stress at the start of the stabilized cycle and σ_s is the yield stress at stabilized cycle.

$$\sigma_s = \frac{\sigma_1 + \sigma_n}{2} \tag{2-17}$$

where σ_1 and σ_n are the stress at the start and end of stabilized cycle.

A phenomenological softening term $[(1 - d_u E_u)^e]$ dependent upon the ultrasonic energy density per unit time has been introduced in the relations of isotropic and kinematic hardening terms to demonstrate the ultrasonic softening effect on yield stress

[151]. The thermal softening is included in the flow stress model by embedding the temperature term of $\left[1-\left(\frac{T-T_r}{T_m-T_r}\right)^m\right]$ [161]. By including both thermal softening and acoustic softening, the modified equations of isotropic and kinematic hardening are given by [154]:

$$R_{ultrsonic} = \left[Q(1-e^{-b\bar{\varepsilon}^{pl}})\right]\left[1-\left(\frac{T-T_r}{T_m-T_r}\right)^m\right][(1-d_uE_u)^e] \quad (2\text{-}18)$$

$$\underline{\alpha}_{ultrsonic} = \left[\frac{C}{\gamma}\left(1-e^{-\gamma\bar{\varepsilon}^{pl}}\right)+\alpha_1 e^{-\gamma\bar{\varepsilon}^{pl}}\right]\left[1-\left(\frac{T-T_r}{T_m-T_r}\right)^m\right][(1-d_uE_u)^e] \quad (2\text{-}19)$$

where d_u and e are the material constants related to ultrasonic softening and E_u is the ultrasonic energy density per unit time transferred from ultrasonic vibrator to the material. The constant values of copper are given in Table 2.4. These values were calibrated from experimental work for cyclic loading on copper [162], except the value of e was adopted from the previous simulation work for ultrasonic seam welding [151]. E_u was adopted as 3.5×10^5 W/m^2 for the top coupon, while a smaller E_u of 8.1×10^4 W/m^2 was accessed for the bottom coupon subjected to less acoustic softening. The bottom coupon was relatively far away from the knurling tool, which was mounted on the ultrasonic horn. Based on the literature search and observations in [163], the amplitude of ultrasonic vibrations decreased for the bottom coupon.

Table 2.4 Material parameters in the flow stress model [151,162].

Q (MPa)	b	C (MPa)	γ	m	T_m (°C)	T_r (°C)	d_u (m^2/W)	E_u (W/m^2)	e
40	11	22300	340	1.09	1083	25	1.3e-6	3.5e5 for Top 8.1e4 for Bottom	2

2.5 3D Process Model Development

2.5.1 Model Setup

Figure 2.4a shows the 3D modeling configuration in DEFORM 11.0 for the ultrasonic spot welding experiment. The typical knurl and anvil pattern designs are shown in Figure 2.4b. For the modeled condition, both knurl and anvil had the diamond pattern with 4×4 knurling tips to treat an area of 5×5 mm^2. Both knurl and anvil were treated as rigid bodies in this model. Clamping force was applied at the back of the knurling tools along the vertical direction. The knurl can move along the vertical direction, while the anvil was fixed in all the degree of freedoms.

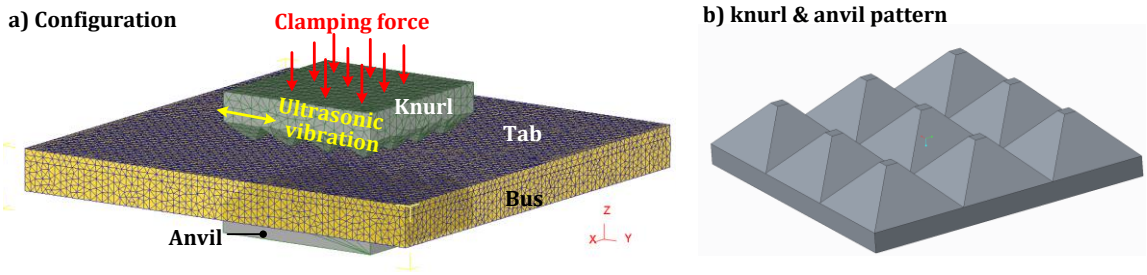

Figure 2.4 FE modeling setup for ultrasonic welding: (a) FE configuration; (b) knurl and anvil pattern.

Multiple simulations were conducted with varying welding time durations from 0.2 sec to 1.0 sec. After the welding step simulation, the tools were disengaged from the joints and coupons and a cooling step was simulated for the workpiece using a natural convection (20 W/m^2-K) condition. The modified Chaboche yield criterion was applied effectively by defining kinematic and isotropic hardening rule separately. The hardening

rule was specified as kinematic with the back stress defined within the whole coupon domain. The sum of isotropic hardening term R and initial yield stress σ_o was given as tabular data in DEFORM, which were calculated from various strains and temperatures.

Ultrasonic vibration was not directly modeled for the horn in this work to save computational cost. When ultrasonic vibration was implemented for the knurling tool, computational cost was too high to complete even a very short period of welding process. In this study, the effect of ultrasonic vibration was considered as acoustic softening on flow stress and frictional heat generation. The acoustic softening effect by ultrasonic vibration was modeled as in Section 0. The effect on frictional heat generation was considered for both friction coefficient and heat generation.

During ultrasonic welding, heat generation mainly occurs at the interface between the two sheets from both mechanical deformation and friction [148]. Thus, a constant surface heat flux was applied in this model at the interface between the top and bottom copper sheets. The applied surface heat flux was 18.15 W/mm^2 in this model, which was calibrated by comparing the simulated temperature histories at different locations to the measurement [141]. The friction coefficients between the knurling tools and workpieces were considered to be temperature-dependent. The friction coefficient was reported to increase with temperature up to a certain temperature then start to decrease [164]. The temperature dependency of friction coefficient was given by:

$$\mu = \mu_0 \left(8.485\text{x}10^{-10}T^4 - 8.842\text{x}10^{-7}T^3 + 1.969\text{x}10^{-4}T^2 - 9.762\text{x}10^{-3}T + 1.12\right) \quad (2\text{-}20)$$

where μ_o equals to 0.39, which is the kinetic friction coefficient at room temperature between copper and steel [165].

2.5.2 Subroutine of Microstructure Evolution Model

To predict the continuous grain growth after ultrasonic welding, a cooling step was simulated with a natural convection (18.15 W/m^2-K) applied after the welding step. For the experiments with longer welding time durations of 0.8 and 1.0 sec, the simulated thermal history for both welding and cooling steps was used to predict the final grain size due to grain growth. A post-processing user routine programmed in FORTRAN was implemented to predict the microstructural evolution and microhardness change as given in Section 3.2. Figure 2.5 shows the flow chart of the post-processing user routine. As aforementioned, the starting temperature of DRX and grain growth were adopted as $0.4T_m$ and $0.5T_m$, respectively, i.e., 270 and 406 °C for Cu. If the temperature was higher than 406 °C, the grain growth would continue through the cooling step after the welding step until the temperature dropped below 406 °C.

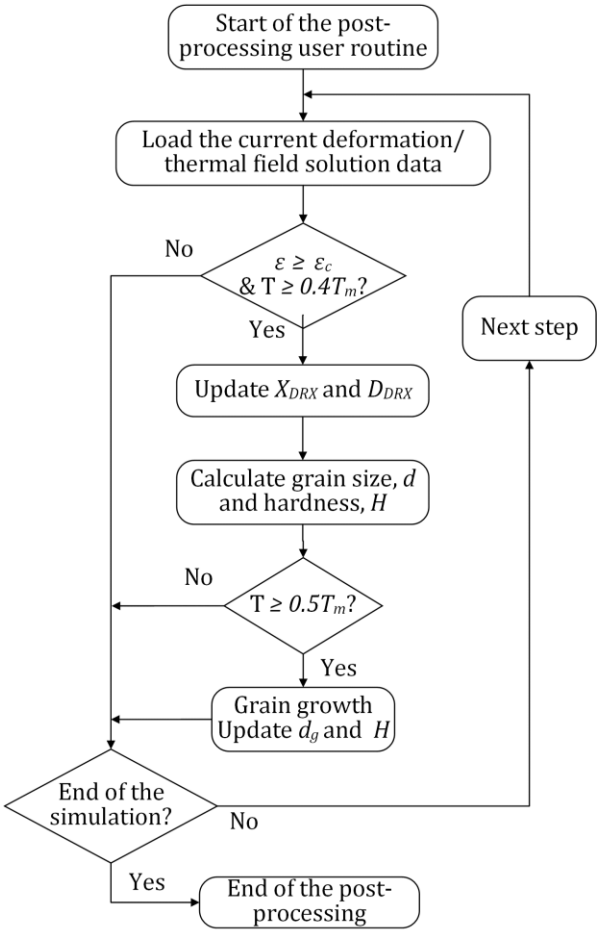

Figure 2.5 Flowchart for post-processing user routine.

2.6 Results and Discussions

2.6.1 Weld Geometry and Deformation Field

Figure 2.6 shows the simulated 3D Von Mises stress distributions on both top and bottom coupons at the welding time of 1.0 sec. A 4×4 array of indents can be seen in the weld zone on the top sheet. The stress in the top sheet was lower than that of the bottom sheet. This was resulted from different magnitudes of acoustic softening. More acoustic softening was applied in the top sheet because significantly more ultrasonic energy was absorbed in the top sheet.

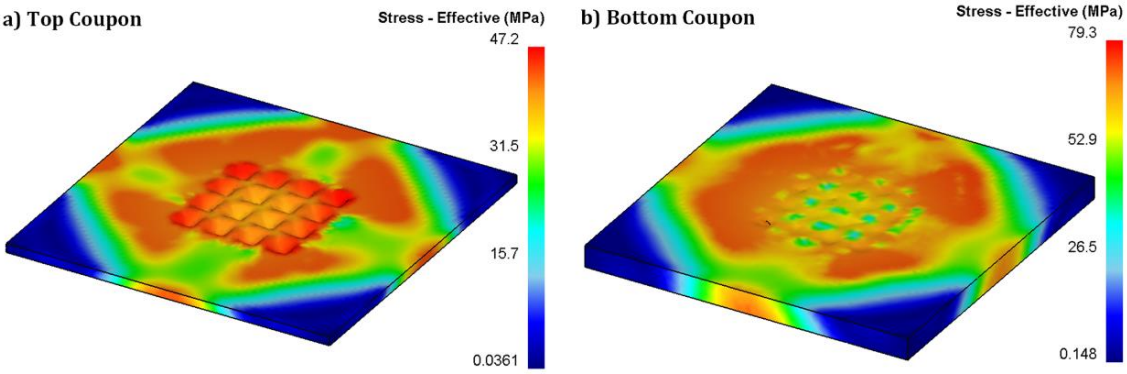

Figure 2.6 Effective stress distribution at 1.0 sec ultrasonic welding in: a) top coupon; b) bottom coupon.

Figure 2.7 shows the predicted weld joint geometry under various welding time durations. The model predictions show more compacted joint with welding time increasing. Larger knurling indents were predicted in the top sheets than the bottom sheet. These modeling results matched well with the experimental results. Figure 2.8 further examines the weld thickness from the simulations, which was defined as the thinnest distance from the top to bottom surface of the weld as shown in Figure 2.7. The model accurately predicted the weld thickness under different welding time duration, which reduced from 1.4 mm achieved at 0.2 sec welding duration to about 0.6 mm after 1.0 sec welding.

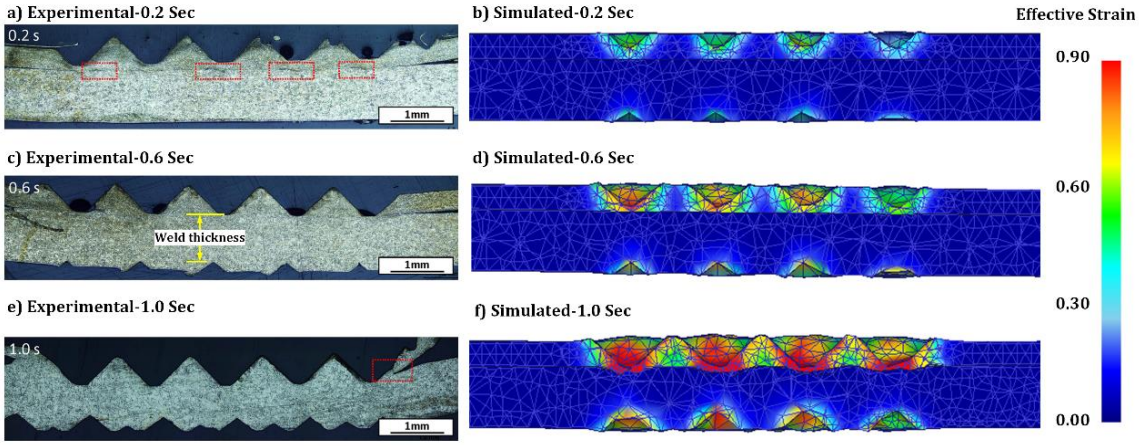

Figure 2.7 Simulated deformed geometry under different welding durations compared with the experimental results in [143].

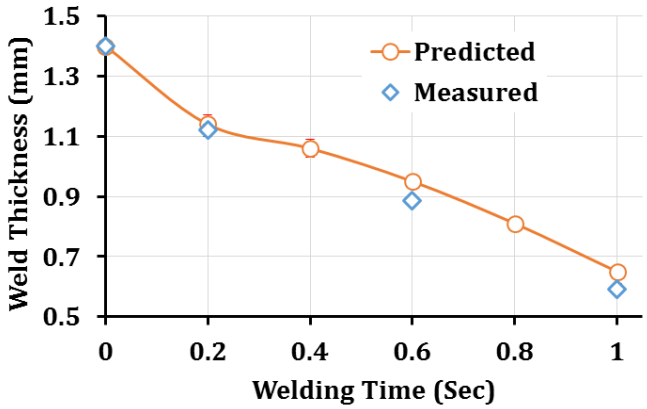

Figure 2.8 Simulated weld thickness under different welding durations compared with experimental measured weld thickness in [143].

2.6.2 Temperature Prediction

Simulated temperature distributions are shown in Figure 2.9 for both welding step (1.0 sec welding time duration) and cooling step. The weld joint area was predicted to have a relative uniform temperature distribution of about 500 °C at the end of 1.0 sec welding duration. This average temperature was determined for welding processes with

various welding time durations. Figure 2.9b shows the temperature prediction during the cooling step with the knurling tools disengaged from the coupons. Figure 2.10 compares the simulated temperatures with the experimental measurements undertaken by a welding time duration of 0.4 sec [141]. Thermocouples could not be directly applied within the weld zone but were attached to the top Cu coupon at about 1.5 mm away from the weld zone, denoted as P1 and P2 as can be seen in Figure 2.10. The temperature histories at these thermocouple locations were tracked from the simulation result. Under the friction heat flux of 18.15 W/mm^2, the simulated temperature histories agreed well with the experimental measurements for both thermocouple locations. This validated the accuracy of temperature prediction in this analysis.

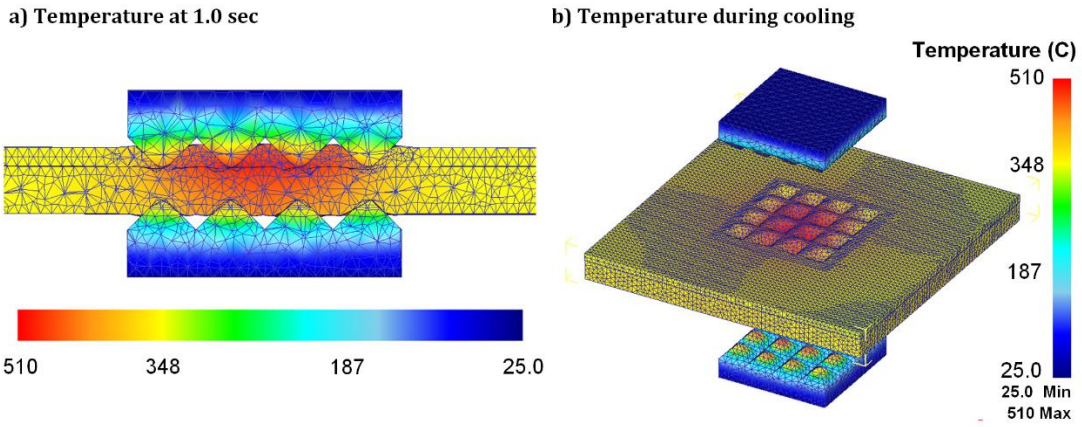

Figure 2.9 Temperature distribution of 1 sec ultrasonic welding simulation: (a) at 1.0 sec; (b) during cooling.

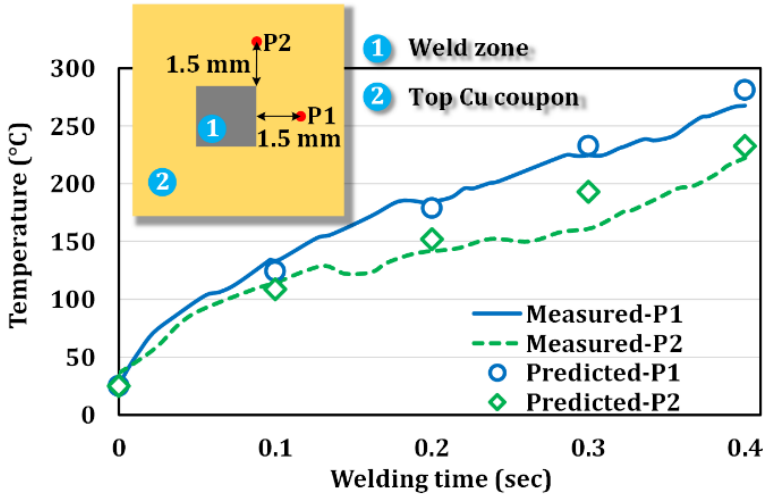

Figure 2.10 Simulated temperature histories at two locations on the Cu coupon during a 0.4 sec welding experiment. The temperature measurements were adopted from Li et al. [141].

2.6.3 Microstructure Prediction

Figure 2.11 shows the simulated microstructural variables in terms of volume fraction of DRX, grain size, and microhardness after 1 sec welding and subsequent cooling, which were calculated using the post-processing user routine. As shown in Figure 2.11a, DRX completed in most area of the top coupon within the weld zone due to the more plastic deformation, while DRX only occurred near the anvil indents in the bottom coupon due to less deformation. Grain size was determined from the temperature history, which was predicted about 34.7 μm in the weld zone and smaller in the surrounding area. Accordingly, the microhardness followed the reversed trend of the grain size. A low hardness was predicted in the welding zone because of the coarse grains and became higher in the surrounding area.

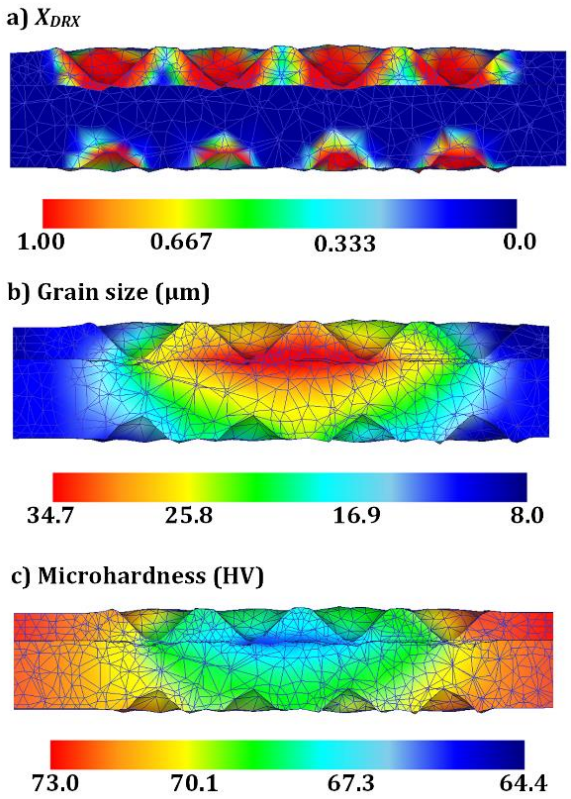

Figure 2.11 Microstructure prediction for 1.0 sec welding.

2.6.4 Microstructure Evolution Mechanisms

In ultrasonic welding, the final microstructure is determined by the coupled metallo-thermo-mechanical histories. The change of microstructure and microhardness highly depends on the process temperature, which is mainly determined by the welding time duration. Hence, the microstructural evolution during ultrasonic spot welding can be classified into three regimes:

- Regime I: under a low processing temperature ($< 0.4T_m$), the work hardening by SPD is hypothesized as the major mechanism to govern the material response and microstructural evolution.

- Regime II: under a medium processing temperature (0.4-0.5 T_m), DRX is the dominant mechanism for microstructural evolution.
- Regime III: under a high processing temperature (> 0.5T_m), DRX and subsequent grain growth are the dominant mechanisms for microstructural evolution. As the completion of recrystallization, grain growth occurred to reduce the grain boundary area, and would continue after the welding process. Eventually, the material would be softened and had a uniform coarse-grained structure across the weld interface.

The simulation results of process temperature under different welding conditions were shown in Figure 2.12. Figure 2.12a shows the predicted process temperature histories for welding time durations of 0.6 and 1.0 sec. It can be seen that the process temperature increased very fast during the welding step, and then dropped quickly within the first 10 sec of the cooling step. After the welding time duration, a workpiece cooling process took place in air, which usually takes more time with a higher process temperature. This trend can be seen in Figure 2.12a. For 1.0 sec welding time duration, the process temperature was predicted to be above 406 °C (0.5T_m for Cu) for 16 sec, during which grain growth occurred. While the temperature increase was only increased to about 400 °C under the welding time duration of 0.6 sec, grain growth did not occur under that condition. Thus, for 1.0 sec welding time duration, the material microstructure underwent the aforementioned three regimes. These stages were highlighted with different colors in the zoom-in view in Figure 2.12a

Figure 2.12b summarizes the predicted process temperatures and microstructural evolution regimes under different welding time durations. For the short welding time

duration of 0.2 sec, the process temperature did not reach the DRX starting temperature ($0.4T_m$, i.e. 270 °C for Cu), microstructural evolution was governed by SPD. For welding time of 0.4-0.6 sec, the process temperatures were in the range of the DRX ($0.4\text{-}0.5T_m$, or 270-406 °C for Cu), which dominated the microstructural evolution. For welding time of 0.8 and 1.0 sec, the process temperature exceeded the starting temperature of grain growth ($0.5T_m$, or 406 °C for Cu), and the final grain size was determined by the grain growth mechanism. These findings agreed well with the experimental observations on microstructural evolution.

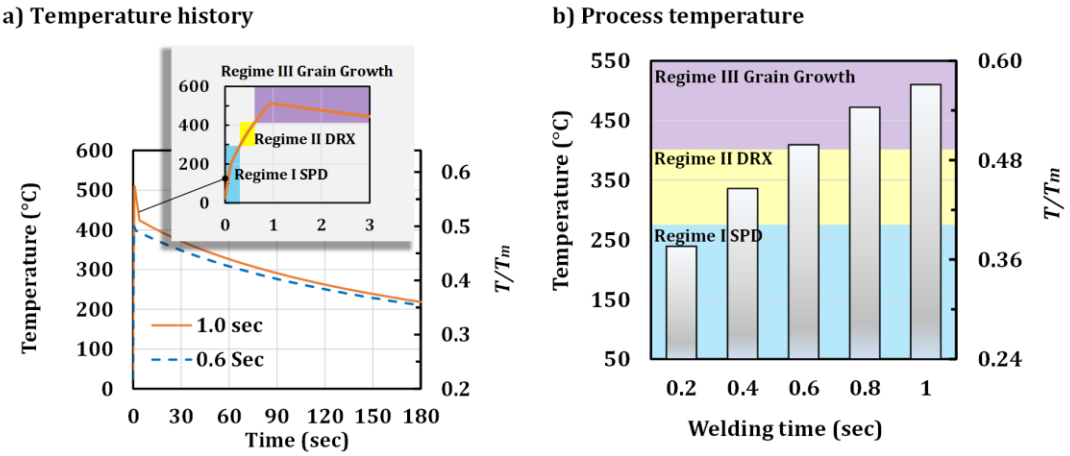

Figure 2.12 Comparison of the simulated temperature histories and peak temperatures: a) Temperature history in both welding and cooling step (welding time of 0.6 and 1.0 sec); b) welding time effect on the simulated process temperatures.

2.7 Summary

A novel metallo-thermo-mechanically coupled 3D FE model was successfully developed for ultrasonic spot welding to model both weld formation and microstructural evolution. A combined isotropic/kinematic hardening flow stress model with an acoustic

softening term was implemented to predict the material response under high-frequency ultrasonic vibration. Using a post-processing user routine, a kinetics model was implemented to predict the material microstructural evolution governed by DRX and grain growth.

The simulated weld zone geometry agreed well with the experiments. The simulations demonstrated that process temperature during ultrasonic welding was highly dependent on the welding time duration. For a welding time duration longer than 0.8 sec, the weld material experienced three different stages, namely, mechanical deformation, dynamic recrystallization, and grain growth. The final distributions of grain size and consequential microhardness were predicted based on thermomechanical solution fields and agreed well with experimental measurements.

The simulation results demonstrated that the essential characteristics of the deformation field and microstructure evolution during ultrasonic welding are well captured in the metallo-thermo-mechanically coupled model. The numerical framework developed in this study has been shown to be a powerful tool to optimize ultrasonic welding process for its mechanical properties and microstructures.

CHAPTER 3.

ULTRA-FINE GRAIN REFINEMENT DURING CRYOGENIC MACHINING

The microstructure evolution of Mg alloys has not been well-understood to date under high strain rate and low temperatures. Cryogenic machining of metals is characterized by high strain rates ($>10^5$ s^{-1}) and low temperatures due to cryogenic cooling by applying liquid nitrogen spray. In the literature, most prior research unpersuasively concludes that formation of an ultra-fine-grained layer during the cryogenic machining of Mg alloys is attributable to dynamic recrystallization. This chapter presents both a thorough literature review and the results of experimental analysis performed to clarify for the first time the complicated microstructure evolution mechanism for the formation of UFG layer during cryogenic machining of Mg alloys. A physics-based material model is then developed to simulate microstructure evolution during cryogenic machining of Mg alloys by considering both slip and twinning responses of the HCP Mg alloy for the first time. This material model is implemented in a 2D FE model to simulate the enhanced surface integrity of AZ31B Mg alloy subjected to cryogenic machining.

3.1 Experimental Analysis of Microstructure Alterations in Cryogenic Machining

The microstructure alterations induced by cryogenic machining is carefully examined for the HCP structured AZ31B Mg alloy in this study. Pu et al. [53] carried out these orthogonal cutting experiments using uncoated C-2 carbide tool inserts. The rake and clearance angle were -7° and 7°, respectively. The geometry of the tool insert is TNMG 432. The parameters of the grooves are: groove width, 1.84 mm; land length,

0.135 mm; groove radius, 1.068 mm; backwall height, 0.042 mm. Two different edge radii of tool inserts (r_e) were used in the experiments: 30 µm and 70 µm. When the cryogenic cooling was applied, an Air Products ICEFLY® system was used to inject liquid nitrogen to the machined surface from the clearance side of the cutting tool. The temperature of the AZ31B Mg alloy discs during machining was measured by an infrared (IR) camera. The effect of cryogenic cooling was investigated by performing the orthogonal cutting tests with or without the cryogenic cooling, i.e. cryogenic machining or dry machining. A constant cutting speed of 100 m/min and a feed of 0.1 mm/rev were used for all the test conditions. Table 3.1 listed all the experimental conditions.

Table 3.1 Orthogonal cutting tests for AZ31B Mg Alloy [53].

Tests	Cooling Method	Edge radius, r_e (µm)	Cutting speed, v_c (m/min)	Feed, f (mm/rev)	Max surface temperature, T_{max} (°C)	UFG layer thickness, t_{UFG} (µm)
Dry-Re30	-	30	100	0.1	125	< 3
Cryo-Re30	Cryogenic	30	100	0.1	52	10-14
Dry-Re70	-	70	100	0.1	-	12-18
Cryo-Re70	Cryogenic	70	100	0.1	71	15-23

Some of the critical experimental results were summarized in Table 3.1. For dry machining with an edge radius of 30 µm, the maximum machined surface temperature, T_{max}, was found to be 125 °C, while a significant decrease in T_{max} was obtained by cryogenic cooling. In the cryogenic condition Cryo-Re30 using the same cutting process parameters, T_{max} dropped from 125 °C to 52 °C by 60%. Using a larger tool cutting edge

radius of 70 µm, T_{max} slightly increased due to more plastic deformation, but it was still as low as 71 °C under cryogenic cooling. Thus, the cooling effect of the application of cryogenic coolant was very significant. In Table 3.1, the UFG surface layers were also observed in the machined surface due to the SPD effect under cryogenic cooling. With the edge radius of 30 µm, the thickness of UFG layer was about 10-14 µm under cryogenic cooling, while the UFG layer can be barely seen without the cryogenic coolant. Due to the enhanced SPD effect using a larger edge radius of 70 µm, the thickness of UFG layer in cryogenic machining even increased by 50-65% from that of Cryo-Re30.

Some of the critical experimental results were summarized in Table 3.1. For dry machining with an edge radius of 30 µm, the maximum machined surface temperature, T_{max}, was found to be 125 °C, while a significant decrease in T_{max} was obtained by cryogenic cooling. In the cryogenic condition Cryo-Re30 using the same cutting process parameters, T_{max} dropped from 125 °C to 52 °C by 60%. Using a larger tool cutting edge radius of 70 µm, T_{max} slightly increased due to more plastic deformation, but it was still as low as 71 °C under cryogenic cooling. Thus, the cooling effect of the application of cryogenic coolant was very significant. In Table 3.1, the UFG surface layers were also observed in the machined surface due to the SPD effect under cryogenic cooling. With the edge radius of 30 µm, the thickness of UFG layer was about 10-14 µm under cryogenic cooling, while the UFG layer can be barely seen without the cryogenic coolant. Due to the enhanced SPD effect using a larger edge radius of 70 µm, the thickness of UFG layer in cryogenic machining even increased by 50-65% from that of Cryo-Re30.

Figure 3.1 shows a typical example of microstructure below the machined surface (Figure 3.1a-c) and in the chip (Figure 3.1d) created with a cryogenic machining

condition Cryo-Re70. The effect of grain refinement near the machined surface compared with the unaffected area was well characterized by the optical microscope in Figure 3.1a. A featureless microstructure of ultra-fine grains can be seen in the topmost layer of about 20 μm in thickness below the machined surface. Below the UFG layer, grain structure was sheared to some extent but quickly recovered to the unaffected microstructure of the bulk material with clear grain boundaries. However, a large amount of twinning lamellas can be found within these coarse grains, located 20 μm below the surface corresponding to a domain not severely strained. Twinning lamellas were observed in the less strained areas for all the other experiment conditions as well. Figure 3.1b shows a scanning electron microscopy (SEM) micrograph (5,000x) of the UFG microstructure, which is a zoom-in view of the location boxed in Figure 3.1a and shows no obvious grain boundaries. Below the UFG layer, grains were strained and elongated along the cutting direction. To examine the microstructure more closely, an area about 2 μm in width within the UFG layer was studied using atomic force microscopy (AFM) as can be seen in Figure 3.1c. Ultrafine grains of 30-60 nm are revealed in this micrograph, which indicates that a machined surface of nanocrystalline grain structure was achieved by cryogenic machining. Comparison of the grain refinement data in Figure 3.1shows that cryogenic machining using a large edge radius tool induces a thicker UFG layer with nanocrystalline grains than dry machining. Grain refinement to a nanocrystalline grain structure enhances the functional performance of the components such as fatigue life and wear/corrosion resistance. The microstructural alteration inside the serrated chip was also studied as shown in Figure 3.1d. A noticeable thick UFG layer was found near the tool-chip interface, which has a UFG layer thickness comparable to that on the machined

surface. Coarse grains with clear grain boundaries remained in the interior of the chip sawtooth. These structures inside the chip correspond to the less strained area between two shear bands during the formation of serrated chip during cutting.

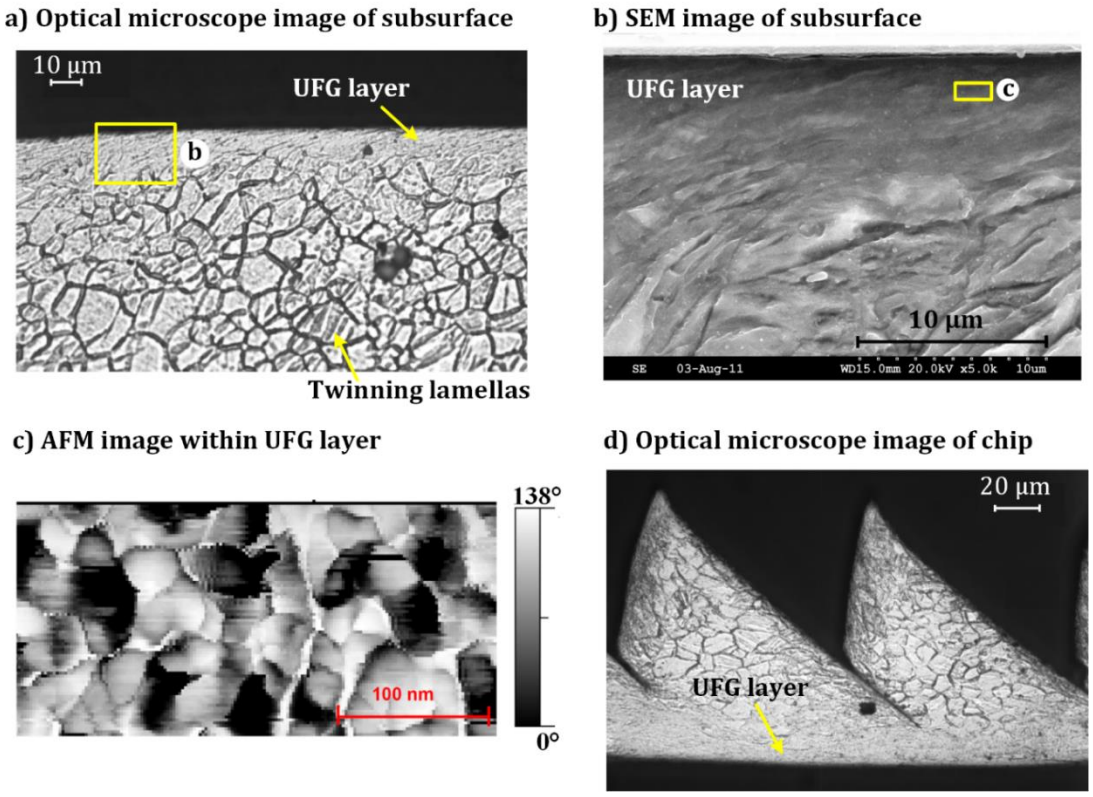

Figure 3.1 Microstructure in the machined surface and chip produced in cryogenic machining: (a) optical microscopy, (b) SEM micrograph, (c) AFM image of machined surface; and (d) optical micrograph of chip, where the raw images were adopted from Pu el al. [53].

3.2 Review of Surface Microstructure Alteration in Cryogenic Machining and Modeling

Cryogenic machining firstly has been considered as an eco-friendly and pollution-free machining technology of difficult-to-machine materials, in order to significantly

increase the tool life and reduce tool wear due to the reduction of tool-tip temperature [166,167]. With further studies of this process, the improved surface integrity has been found in the machined surface of Inconel 718, AISI 4140 and 52100 steel [168–170]. During cryogenic machining, a UFG surface layer is often formed in the machined surface with the increase of surface hardness and compressive residual stresses due to the severe plastic deformation. Recently, cryogenic machining has also been conducted on AZ31B Mg alloy to improve the machined surface integrity of mechanical components made by this material [21]. Pu et al. [53] unveiled the significant effect of cryogenic cooling on the surface integrity in the machined surface of AZ31B Mg alloy, in terms of better surface finish, the formation of UFG surface layer, increased microhardness and compressive residual stress. These attributes are critical for the performance on corrosion resistance of Mg alloys [171–174]. These past researches indicated that the optimum surface integrity for Mg alloy components can be achieved by cryogenic machining. Hence, accurate process simulations are critically needed to understand the cryogenic machining process, determine the optimum process conditions, and to achieve the most desirable surface integrity characteristics.

FE analysis have been performed for cryogenic machining of AZ31B Mg alloys to predict the residual stress in the machined surface layer [21]. Phenomenological material constitutive models, such as Johnson-Cook (JC) model, have been mostly used to model the flow stress during FE machining simulation. The Zener-Hollomon parameter-based empirical relationship was calibrated using the experimentally measured grain size. Then, it was embedded in a 2D FE analysis to simulate the change of grain size during turning of AA7075-T651 Alloy with cutting speed of 180-720 m/min [17,18],

Inconel 718 alloy [19], AZ31B Mg alloy [20], and AISI 52100 steel [22]. However, the predominant twinning response of Mg alloys was rarely accounted in numerical analysis of machining and other SPD processes. Also, the existing models are not capable to model the complicated microstructure alterations during cryogenic machining of AZ31B Mg alloy.

Due to the poor formability of Mg alloys, the conventional microstructural analysis of Mg alloys focused on the hot working processes at elevated temperatures above 200 °C and low/quasi-static strain rates [175,176]. Drastic work hardening can be usually observed firstly, while dynamic recovery was relatively slow. With the increase of true strain, sufficient strain energy was stored to enable dynamic recrystallization due to deformation. The onset of DRX, even the potential subsequent grain growth, provided a softening mechanism after a certain level of strain and resulted in a significant drop of the flow stress to a steady-state level.

However, the microstructure evolution of Mg alloys has not been well-understood under cold working conditions under high strain rate. Microstructural analyses in mechanical testing have shown different microstructure evolution routes for Mg alloys under these conditions. Ulacia et al. [55] characterized the microstructural evolution under a series of tensile tests over wide range of strain rates (10^{-3}-1.5×10^{3} s^{-1}) and temperatures (20-400 °C). For high strain rates in their experiments (5×10^{2}-1.5×10^{3} s^{-1}), the conventional DRX was not observed at any temperature. When temperature was greater than 250 °C, only a small amount of recrystallized grains can be observed [57]. These small amount of recrystallized grains were suggested to be the result of an increasing contribution of rotational recrystallization mechanism in the recrystallized

grains due to the limited time for diffusion [55,57]. Li et al. [177] also found the strain softening due to DRX did not occur in the tensile testing of AZ31B Mg alloy at 50-150 °C with strain rates lower than 0.1 s^{-1}.

Thus, significantly different stress-strain behaviors have been observed for Mg alloy under cryogenic conditions. Giraud et al. [178] conducted dynamic shear tests on 4 mm thick disks of this alloy using a Gleeble machine below 0 °C. These tests were performed at temperatures ranging from -25 °C to 400 °C and strain rates ranging from 10 s^{-1} to 5×10^{4} s^{-1}. Their results show that for strain rates less than or equal to 4×10^{3} s^{-1}, the mechanical behaviors for temperatures less than 200 °C differed from those obtained at over 200 °C. When the temperature was lower than 200 °C, the alloy deformed by slip and twinning, stress was not sensitive to strain rate, and the softening behavior due to DRX did not occur. When the temperature was higher than 200°C, the alloy exhibited a softening behavior due to dynamic recrystallization, and stress was found to be sensitive to strain rate. However, when strain rate increases to 5×10^{4} s^{-1}, the alloy does not exhibit any softening behavior through the whole temperature range from -25 °C to 400 °C. Under such high-strain rate conditions, the time duration during plastic deformation was considered to be significantly shorter than what is required for DRX to occur and develop even at elevated temperatures [55,56].

3.3 Material Constitutive Modeling

As aforementioned, the plastic deformation and microstructure evolution of Mg alloys is governed by different mechanisms at different stage of plastic deformation, i.e. twinning and slip. Moreover, process conditions, e.g. strain rate and temperature, also

significantly affect the mechanism of microstructure evolution. Hence, a comprehensive material model is required to consider all the mechanisms.

Twinning is usually observed in the early stage of the plastic deformation, and facilitated by the high strain rate and low temperature. To capture the material twinning response, Mayer et al. developed constitutive models to capture the flow stress behavior of different materials with different crystal structures, taking both twinning and slip response accounted [49,50]. For HCP material, the flow stress when twinning is dominant can be represented as [50]:

$$\sigma_T = \sigma_{T0} + k_T d^{-0.5} \tag{3-1}$$

where σ_{T0} and k_T are the athermal portion of the twinning stress and Hall-Petch (HP) slope for twinning, respectively. These material parameters were determined by Barnett et al. [179], where k_T is a constant of 9.5 MPa-mm$^{1/2}$ and σ_{T0} (MPa) can be fitted as:

$$\sigma_{T0} = -3.326\times10^{-4}T^2 - 4.026\times10^{-2}T + 41.61, \quad for\ \ 25\,°C \le T \le 200\,°C \tag{3-2}$$

In this model, twinning response is applied when the twinning stress of σ_T becomes less than or equal to the slip stress of σ_S [49,50]. Otherwise, the slip response dominates.

The slip response also plays an important role after the early stage of the plastic deformation. The slip constitutive response can be calculated with a dislocation density-based material constitutive model developed by authors. In this model, a dislocation cell structure is assumed to form during deformation, which consists of two parts, dislocation cell walls and cell interiors. The dislocation cell structure obeys a rule of mixtures. The following describes the dislocation density evolution rates in cell interiors and cell walls, respectively:

$$\dot{\rho}_c = \alpha^* \frac{1}{\sqrt{3}b}\sqrt{\rho_w}\dot{\gamma}_w - \beta^* \frac{6}{bd(1-f)^{1/3}}\dot{\gamma}_c - k_o\left(\frac{\dot{\gamma}_c}{\dot{\gamma}_o}\right)^{-1/n}\rho_c\dot{\gamma}_c \qquad (3\text{-}3)$$

$$\dot{\rho}_w = \beta^* \frac{\sqrt{3}(1-f)}{fb}\sqrt{\rho_w}\dot{\gamma}_c + \beta^* \frac{6(1-f)^{\frac{2}{3}}}{bdf}\dot{\gamma}_c - k_o\left(\frac{\dot{\gamma}_w}{\dot{\gamma}_o}\right)^{-1/n}\rho_w\dot{\gamma}_w \qquad (3\text{-}4)$$

where the cell interior dislocation density is defined as ρ_c, and the dislocation density on the cell walls is defined as ρ_w, which is a sum of statistical dislocations and geometrically necessary dislocations. The first terms on the right side correspond to the generation of dislocations due to the activation of Frank–Read sources. The second terms denote the transfer of cell interior dislocations to cell walls where they are woven in. The last terms in each of the evolution equations represent the annihilation of dislocations leading to dynamic recovery in the course of straining. The dynamic coefficients of dislocation generation (α*), interaction between the cell walls and interiors (β*), and dislocation annihilation (k_o) are dislocation evolution rate control parameters for the material. *n* is a temperature sensitivity parameter, f is the volume fraction of the dislocation cell wall, *b* is the magnitude of the Burgers vector of the material, *d* is the dislocation cell size, $\dot{\gamma}_w$ and $\dot{\gamma}_c$ are the resolved shear strain rates for the cell walls and interiors, respectively, and $\dot{\gamma}_o$ is the reference resolved shear strain rate. It is assumed that the resolved shear strain rate across the cell walls and cell interiors are equal, i.e. $\dot{\gamma}_w = \dot{\gamma}_c = \dot{\gamma}$, which satisfies the strain compatibility along the interface between interiors and boundaries. The resolved shear strain rate $\dot{\gamma}$ *c*an be calculated by the von Mises strain rate $\dot{\varepsilon}$ by using $\dot{\gamma} = M\dot{\varepsilon}$, where *M* is the Taylor factor.

$$\tau_c^r = \alpha G b\sqrt{\rho_c}\left(\frac{\dot{\gamma}_c}{\dot{\gamma}_o}\right)^{1/m} \qquad (3\text{-}5)$$

$$\tau_w^r = \alpha G b \sqrt{\rho_w} \left(\frac{\dot{\gamma}_w}{\dot{\gamma}_o} \right)^{1/m} \tag{3-6}$$

$$\tau^r = f \tau_w^r + (1-f) \tau_c^r \tag{3-7}$$

where G is the shear modulus and m is the strain rate sensitivity of the material. Volume fraction f of the dislocation cell wall, total dislocation density ρ_{tot} are given as follows:

$$f = f_\infty + (f_o - f_\infty) e^{\left(-\frac{\gamma^r}{\gamma_0}\right)} \tag{3-8}$$

$$\rho_{tot} = f \rho_w + (1-f) \rho_c \tag{3-9}$$

where f_0 and f_∞ are the initial and saturation volume fractions of cell walls, respectively.

As aforementioned, the prismatic slip is the predominant deformation mechanism after the early stage of the plastic deformation at high strain rate and low temperature. In addition, from the microstructure characterization analysis based on Fig. 1, the significant grain refinement occurred within the largely strained top layer. Thus, the grain refinement in this domain can be modeled based on the dislocation density-based grain refinement mechanism. The dislocation cell size, d, is given as:

$$d = \frac{K}{\sqrt{\rho_{tot}}} \tag{3-10}$$

where K is a material constant and adopted to be 40 in this study based on the experimental measurement of grain structure generated by the cryogenic machining of AZ31B Mg alloy [53].

The strengthening of material is characterized by the microhardness change (Δh, in GPa), which can be predicted based on the dislocation density evolution due to SPD [40,180]. It is given as

$$\Delta h = k_h M_t \alpha_o G b \sqrt{\rho_{tot}} \tag{3-11}$$

where k_h is a constant slope of 1.5 [179], α_o is a constant of 0.25 [34], and G is the shear modulus.

To determine the other material model parameters, which are unknown in literature for this material, the dislocation density-based material plasticity model was programmed in MATLAB to solve Eqs. 3.3-11 and the stress-strain curves were simulated at different temperatures and strain rates. The dislocation density evolution rate control parameters, α^*, β^*, and k_o were determined by calibrating the model using the material flow stress experimental data in literature [178,181]. With adapting tunable parameters (α^*, β^*, and k_o) starting from certain initial values, a global minimum in the parameter space was achieved by comparing experimental and calculated data. The optimized material parameters of the dislocation density-based material plasticity model should be able to replicate the stress-strain curves obtained by the material mechanical tests. Flow stress data for Mg alloy AZ31B under the shear tests [178], tensile tests [181], and tensile split Hopkinson bar tests [181] were obtained over a large range of strain rates, from $0.003 s^{-1}$ to $1{,}500\ s^{-1}$, and the temperature range from room temperature to 300 °C, which covers the ranges of temperatures in this cryogenic machining study. The temperature sensitivity coefficients, m and n, were determined to be temperature-dependent as follows [182]:

$$m = \frac{A}{T} \tag{3-12}$$

$$n = \frac{B}{T} \tag{3-13}$$

The dislocation density model parameters are given in Table 3.2. The dislocation density-based material plasticity model predicts the stress-strain relationships at different

temperatures and strain rates and the simulation results are compared with the experimental data as shown in Figure 3.2. The high strain rate experimental data was collected using a tensile split Hopkinson bar (TSHB) apparatus. Elevated temperature experiments (up to 300°C) were performed at high strain rates using a radiative furnace mounted on the TSHB apparatus [181]. As can be seen in Figure 3.3, the identified model parameters have been proved accurate enough to replicate the stress-strain relationships obtained under the material mechanical tests at different temperatures and strain rates, which validates the dislocation density-based material plasticity model for Mg alloy AZ31B. Although Mg alloy sheets prepared by the rolling process show strong anisotropic behaviors, the isotropic constitutive model was considered in this study because the anisotropy diminished when the strain rate is greater than 1,000 s^{-1} [57]. The material mechanical and thermal properties of Mg alloy AZ31B used in the models are given in Table 3.3.

Table 3.2 Dislocation density-model constants for Magnesium AZ31B.

Dislocation rate control			Temperature sensitivity control		Process constants						Initial values			
α^*	β^*	k_o	A (K^{-1})	B (K^{-1})	$\dot{\gamma}_o$	f_o	f_∞	K	M	$\tilde{\gamma}^r$	ρ_w (m^{-2})	ρ_c (m^{-2})	b (nm)	α
0.05	0.035	7-11	5E4	1.5E4	1.5E4	0.25	0.07	4	3.06	3.2	1E12	1E11	0.3196	0.25

Table 3.3 Material physical properties of AZ31B [51,183].

E (GPa)	G (GPa)	v	b (nm)	ρ (kg/m^3)	T_m (°C)	α (10^{-6}/°C)	k_c (W/m·°C)	c_p (J/kg·°C)
45	17	0.35	0.3196	1780	618	24.8	103.21+0.096×T	1181.8+0.666×T

Note: all the temperatures in this study are in Celsius.

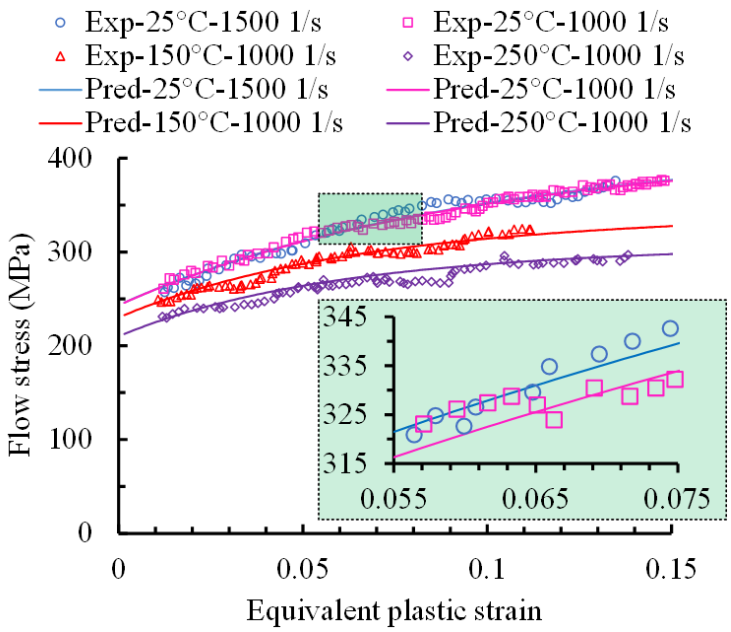

Figure 3.2 Dislocation density-based plasticity model predictions for Mg Alloy AZ31B compared with flow stress measurement under various conditions from Ref. [181].

3.4 Process Modeling

3.4.1 Model Setup

The FE simulations of the cryogenic machining process were performed with a commercial machining simulation software package AdvantEdge™ 6.4. The material constitutive model considering the microstructural evolution was implemented using the user-defined subroutines. Figure 3.3 illustrates the modeling configuration developed in AdvantEdge™ 6.4. A 4-mm cut was simulated to ensure that chip morphology and all solution fields reach a steady state.

Advanced features of residual stress and multi-pass analysis in AdvantEdge™ were implemented in this model. This residual stress technique implements post-cut analysis, i.e. the relaxation step, after a single pass or multi-pass cutting simulation is

done. During the relaxation step, the heat is dissipated, the stress fluctuations die out, and then a final state of stress in the workpiece is computed [38]. To predict the residual stresses and microstructural attributes on machined surface accurately, a very fine mesh was generated below the machined surface and in the shear zone, which uses a fully-automatic adaptive remeshing algorithm during the cutting simulation. A depth of mesh refinement (d_{fm}) was specified in the simulation setting to determine the thickness of fine mesh domain below the machined surface. Due to the computation cost, d_{fm} was specified as 0.3 mm which is sufficient for a depth of cut 0.1 mm in the cutting experiments, with a minimum element size constrained as 5 µm. After cutting pass finished, the chip will be automatically removed, followed by thermo-mechanical relaxation of the workpiece. The maximum number of cutting passes was limited to two for a multi-pass residual stress analysis. Two-pass cutting simulation was considered necessary to predict the final surface integrity accurately, because the final machined surface was produced after multiple cuts experiments. All the solution fields including residual stress, hardness and microstructural attributes were simulated simultaneously in the machined surface with the fine mesh after multiple cuts.

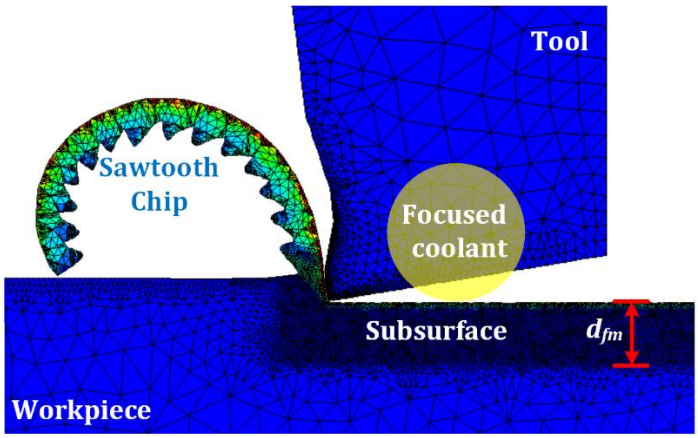

Figure 3.3 The configuration of cryogenic machining simulation in AdvantEdge™.

The chip formation was simulated in AdvantEdge™ without using any artificial chip separation criterion. Since the chips of AZ31B Mg alloy under all the tested conditions were serrated, it was necessary to simulate the chip serration process in the FE model in order to accurately predict the cutting force, stress, and process temperature. A modified material flow stress model reported by Calamaz et al. [184] was adopted to simulate serrated chips by incorporating flow stress softening effects. The critical strain was adopted as 0.5 reported by Calamaz et al. [184], and the flow stress drop was calibrated as 70% by comparing the simulated sawtooth chip to those from experiments.

The cutting tool inserts were modeled by importing the script with dimensions to the custom tool editor in AdvantEdge™. The thermo-mechanical properties of tool material were adopted from the default properties of provided in the tool material library of AdvantEdge™. The frictional coefficient at the tool-chip interface was 0.7, which was adopted from a previous study of frictional behavior [20,185]. The initial residual stress distribution induced by the sample preparation process of milling was implemented in a text script file by AdvantEdge™ solver. The values were adopted from Pu et al. [53] for all conditions.

A focused coolant was defined within an area covering the right boundary of tool and the clearance between tool relief face and the machined surface as shown in Figure 3.3. Since the coolant was focused sprayed into the clearance, the heat transfer within this domain was considered as an internal turbulent flow. The convective coefficient was firstly evaluated with Dittus-Boelter equation based on the material properties of liquid

nitrogen and related process parameters listed in Table 3.4 [186]. Then, it was finally adjusted to $5x10^5$ W/m^2·°C using multiple simulations.

Table 3.4 Coolant parameters and physical properties of liquid Nitrogen [187].

Property	Value
Density (kg/m^3)	808
Dynamic viscosity (mPa-s)	15.8
Thermal conductivity (W/m·°C)	1.38
Specific heat (J/kg·°C)	2042
Spray rate (kg/min)	0.6
Nozzle diameter (mm)	3
Spray velocity (m/min)	105.05

3.4.2 Material Subroutines

A User-Defined Yield Surface (UDYS) material plasticity model was developed for AZ31B Mg alloy with FORTRAN in AdvantEdge™. The constitutive model consisted of subroutines of the dislocation density-based slip response in companion with the twinning response, as well as the grain refinement mechanism.

Figure 3.4 shows the algorithm flowchart of the UDYS subroutine used in the simulation. In the beginning of the simulation, the model parameters and initial values of internal state variables were initialized with an input script. During the simulation, the material subroutines were called at each nodule within the workpiece and chip domain to update all internal state variables and solution fields. The constitutive plasticity model defined before in Section 3.3 was implemented to determine the twinning-slip transition by comparing the calculated slip stress with twinning stress. The chip formation and

solution fields would be simulated with the updated material flow stress and thermal properties.

Based on the previous analysis on the plastic deformation mechanism, the material can be classified into three states: slip predominant, twinning predominant, and resolved twinning. The resolved twinning, as previously discussed, is considered as the material with twinning predominant at the early stage of plastic deformation, but finally governed by significant prismatic slip. Thus, a deformation mechanism index M_{index} (0, 1, or 2) was defined to identify the current material state with different deformation mechanisms at each nodule in each time step. The indexes of 0, 1, and 2 are defined as slip, twinning, and resolved twinning, respectively. When slip response was firstly determined to be predominant and equivalent plastic strain was further increased to above a critical strain, the deformation mechanism index would be set to 2. The critical strain ε_r of 0.15 was assumed in this model [178]. The nodules carrying the index of 1 by the end of the simulation would represent the domain with a large amount of twinning structures remained below the machined surface after the whole cutting process was done.

The dislocation-based grain refinement model is solved over the whole workpiece and chip domain, in the sequence of deformation solution dependent model parameters, dislocation density evolution rate, dislocation density, microhardness change, and grain size. However, the grain size was only to be calculated and updated at the domain with the M_{index} as 2 (predominant slip response by prismatic slip, greater strain with twinning structure resolved). After the current time step, values of dislocation density, grain size and other internal state variables would be saved for next time step.

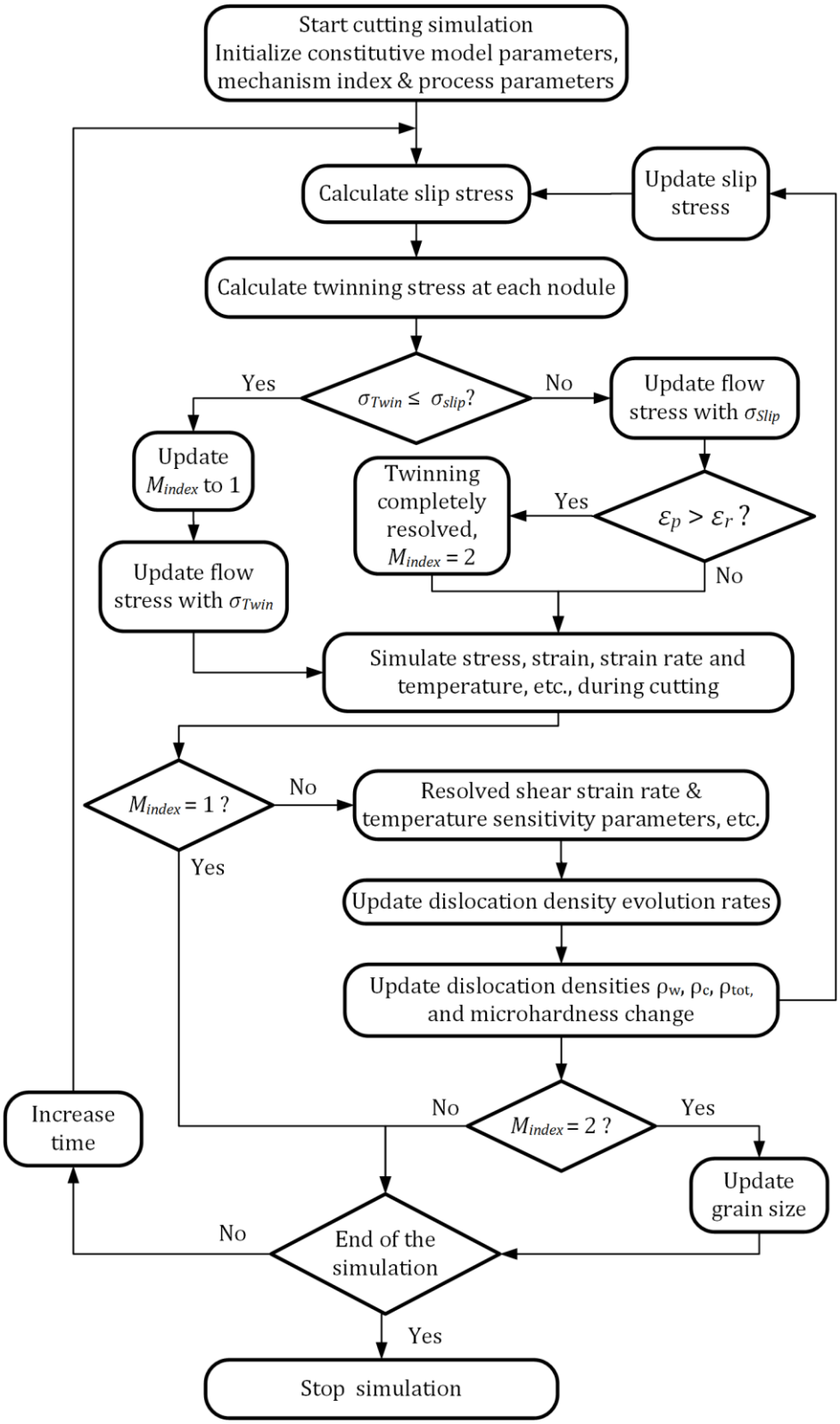

Figure 3.4 Flowchart of the material subroutines in AdvantEdge™.

3.4.3 Two-Pass Simulations

Figure 3.5 shows the schematic of a multi-pass (2-pass) residual stress analysis with AdvantEdge™. When the simulation started, the workpiece was initially meshed with coarse elements as can be seen in Figure 3.5a. As the tool started to contact the workpiece during the 1st cutting pass simulation, a fine mesh was generated by the adaptive remeshing algorithm from the initial coarse mesh within the depth of mesh refinement d_{fm}. The fine mesh layer kept growing as the tool advanced. As the 1st pass simulation completed, such a fine mesh was generated along the whole cutting distance, and the chip would be removed for the relaxation step. The simulation results would be then carried over to the 2nd cutting pass simulation. During the 2nd cutting pass simulation, the fine mesh from the previous cut was maintained through the whole cutting distance, with one additional depth-of-cut (0.1 mm) layer of dynamic remeshing moving as the tool advanced as shown in Figure 3.5b. The final machined surface with chip removed after the relaxation steps was also illustrate in Figure 3.5b. Figure 3.5c shows the adaptive remeshing and solution mapping in the chip formation. The mesh was fine inside the shear zone during the chip formation. However, as the sawtooth chip fully formed, the mesh inside the chip became coarser to reduce the computation cost. A solution mapping algorithm was used to map the solution of the state variable fields from a fine mesh to coarse mesh. As demonstrated in Figure 3.5c, result of solution mapping to a coarse mesh lost its high fidelity achieved at a fine mesh to some extent. Hence extra care should be taken when considering the deformation or microstructural attribute distribution inside the chip.

To investigate the effect of multiple passes on the simulation results on surface integrity, steady-state profiles of shear strain, total dislocation density, grain size, and hardness change were extracted from five paths along the depth from machined surface as shown in Figure 3.5b. Since the simulations reached steady state after about 15% of the total cutting length, five extraction paths were defined at 90%, 75%, 60%, 45%, and 30% of the total cutting length, respectively. The average of these profiles is discussed for one-pass and two-pass simulations. Figure 3.6 shows the comparison of profiles of equivalent plastic strain, total dislocation density, grain size, and hardness change, which were obtained from a single pass and a two-pass simulation after stress relaxation for the cutting condition Dry-Re70. All the simulation results after two-pass simulation are very close to those from one-pass simulation. The peak values of these state variables are almost the same and the variation in these profiles are very small. These comparisons proved that the simulation results on the machined surface have converged after the simulation of two cutting passes, and more cutting passes was not necessary to simulate the final surface integrity.

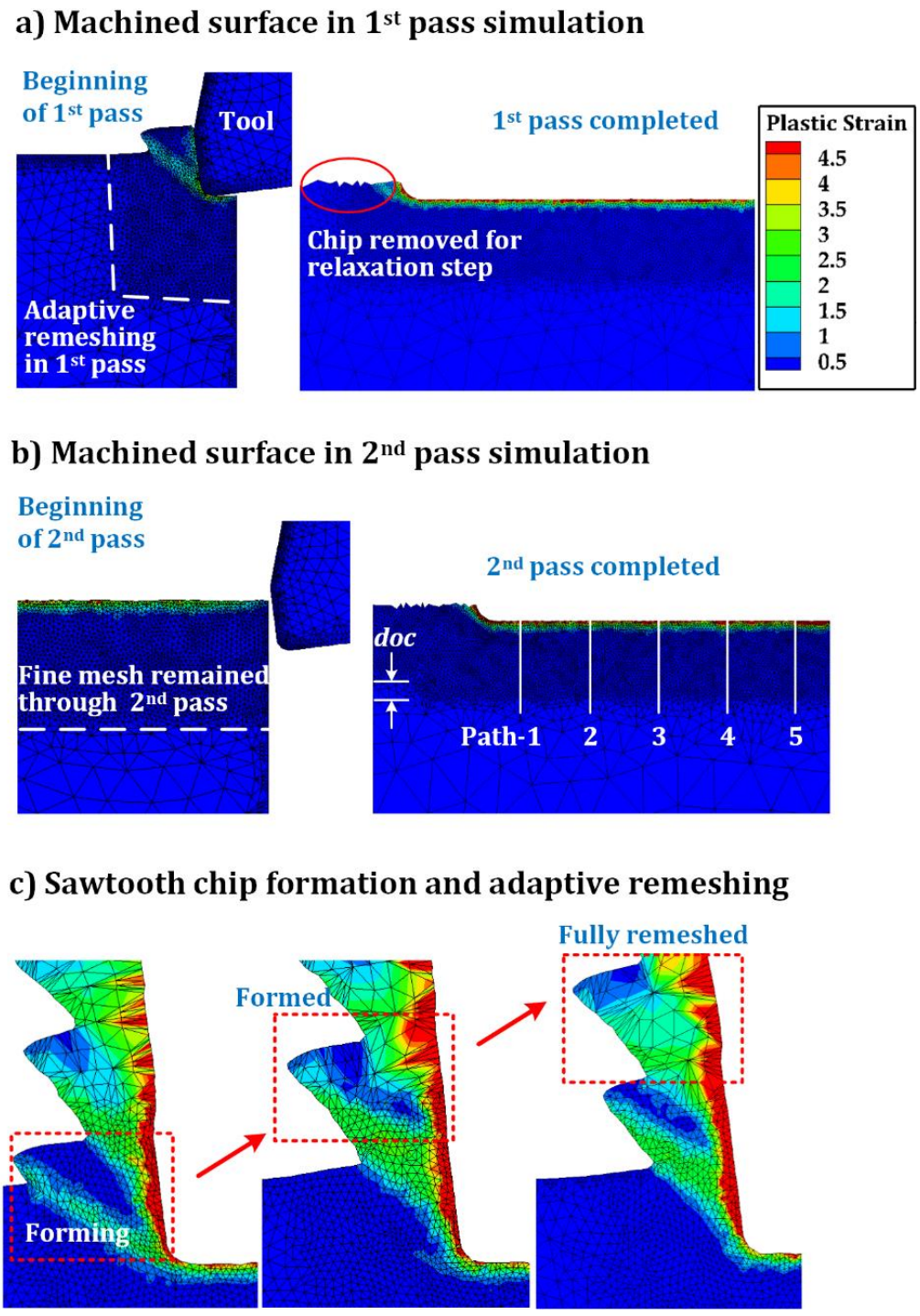

Figure 3.5 Surface and chip meshing in a two-pass simulation (condition Cryo-Re30): machined surface in (a) the 1st pass and (b) the 2nd pass; (c) Serrated chip formation and adaptive remeshing in the chips (color contours in plastic equivalent strain).

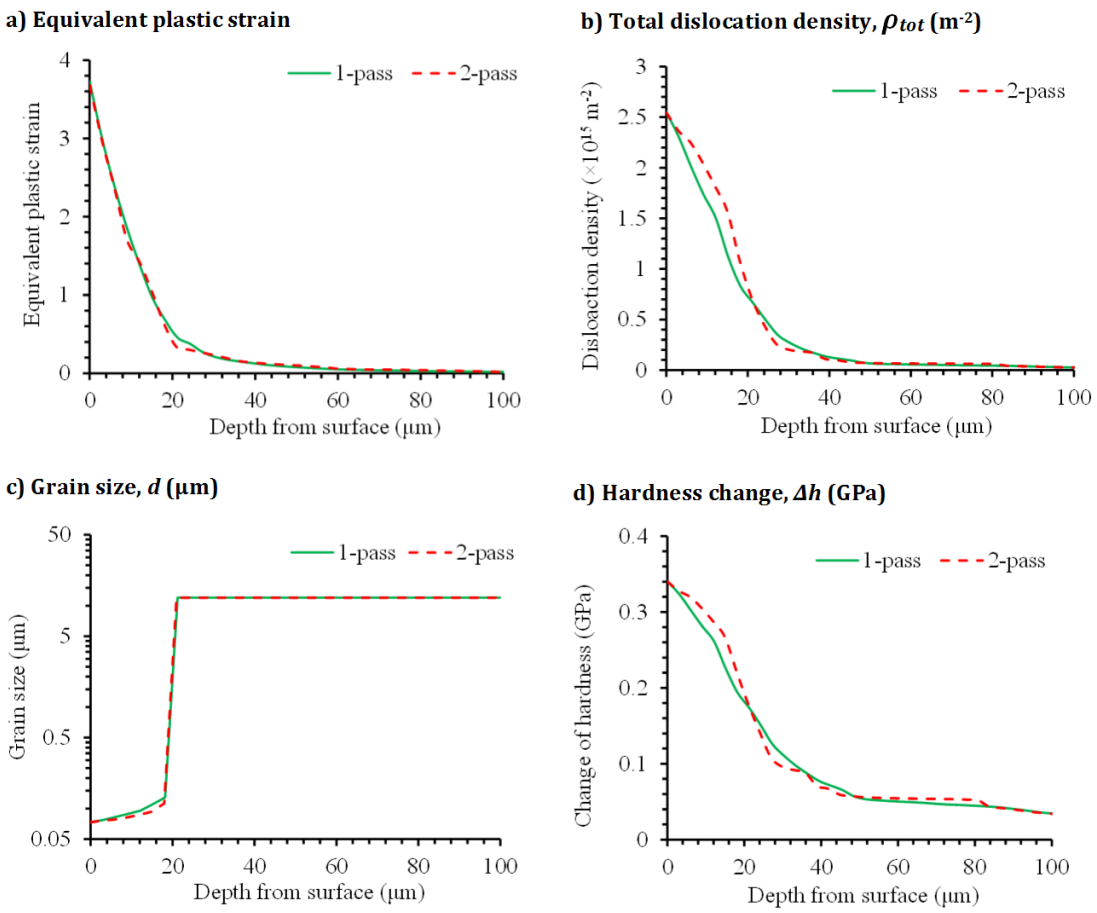

Figure 3.6 Comparison of simulated results from 1-pass and 2-pass cut for condition Dry-Re70: a) equivalent plastic strain; b) total dislocation density; c) grain size; d) change of hardness.

3.5 Results and Discussions

3.5.1 Cutting Force and Temperature Predictions

Figure 3.7a shows the simulated temperature contour of cryogenic machining condition Cryo-Re30, in which the IR measured peak surface temperature is labeled. The simulated maximum surface temperature of 59 °C matches well with the IR measurement of 52 °C peak temperature. For the dry machining condition with the same tool edge

radius (Dry-Re30), the simulated maximum surface temperature was 131 °C which also agrees well with the measured 125 °C by IR camera. It can be seen in Figure 3.7a that cryogenic cooling has a limited effect on the chip, which was quite uniform and much higher than the machined surface temperature. This is because the liquid nitrogen coolant was just applied within the cavity between the tool back relief face and machined surface. Figure 3.7b shows the comparison of simulated cutting force and thrust force history compared to the measured average forces for both components. A cyclic cutting force was predicted due to the formation of serrated chips with varying chip thickness. The experimental measured average cutting force was just slightly higher than the medium level of the predicted cyclic force, and the experimental measured average thrust force was almost the same level of the prediction. The simulation results in the process temperature and cutting forces validated the numerical solution developed for the cryogenic machining process.

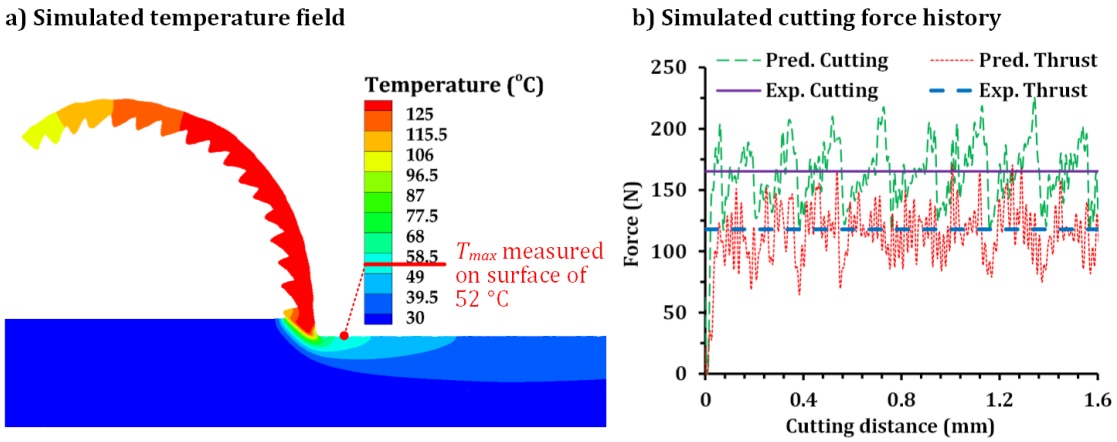

Figure 3.7 Simulated temperature field and cutting force histories compared with the experimental measurement for condition Cryo-Re30 (experimental data adopted Pu et al. [53]).

3.5.2 Grain Refinement

During the cryogenic machining process, the process temperatures were less than 70 °C and 105 °C on the machined surface and in the chip, respectively; under the dry machining condition, the process temperatures increase to 125 °C and 140 °C on the machined surface and in the chip, respectively. These process temperatures are much lower than the typical DRX starting temperatures of 203-298 °C (0.5-0.6 T_m, melting point) [64,65]. The strain rates during the machining tests with cutting speed of 100 m/min (1.67 m/s) are typically on the order of 10^5-10^6 s^{-1}, which are much higher than the strain rates for DRX not to occur found by Giraud et al. [178] and Ulacia et al. [55]. Therefore, it was considered that DRX did not occur during the cutting tests studied in this work.

Figure 3.8 shows the predicted deformation and dislocation fields of the 2D cutting simulation of the experiment of condition Cryo-Re30, in terms of (a) equivalent plastic strain, (b) total dislocation density, and (c) grain size. In Figure 3.8a, high strain gradients can be observed near the machined surface. The strain inside the chip is not uniform. The strain along the tool-chip interface is as high as 4. The peak strain along the shear plane where the serrated chip initiated was 2.5, which is much higher than those between the adjacent sawtooth chips. Dislocations accumulate more as strain increases, as can be seen in Figure 3.8b, which shows a similar pattern to the strain not only along the machined surface, but also in the chip. Beneath the machined surface, the grain size largely reverses the pattern of the dislocation density distribution, with finer grain sizes near the machined surface and coarser grains in the unaffected bulk material. In the chip, the grain size along chip-tool interface was also refined to submicron, while it was close

to the initial grain size in the chip tooth material. This predicted grain size distribution agrees with the grain size change as shown in Figure 3.9d. A similar trend of grain refinement and strain distribution was simulated along the machined surface and chip-tool interface for all the four experimental conditions in this study.

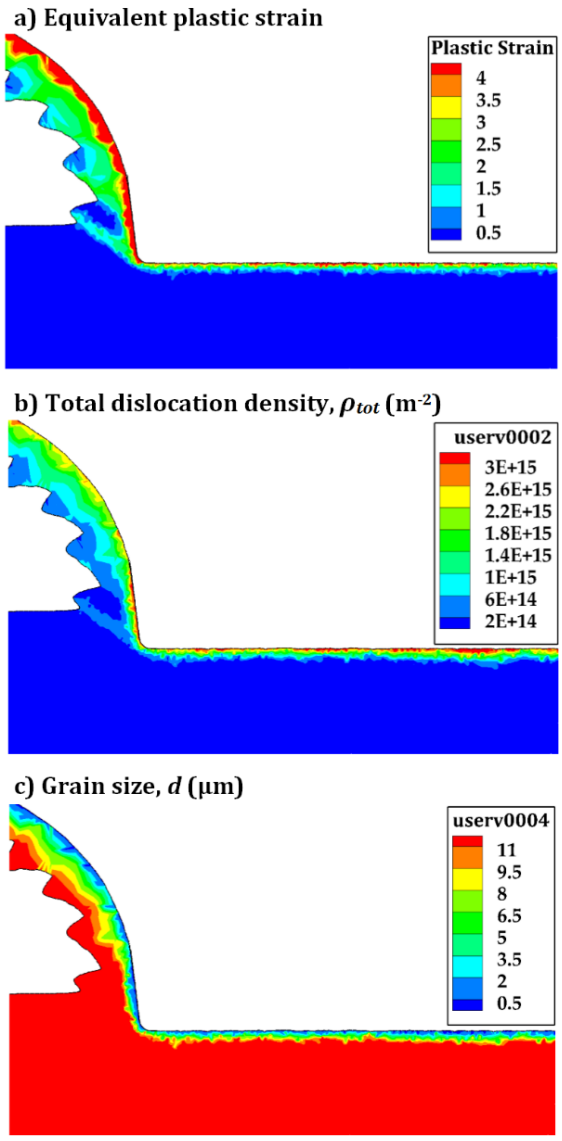

Figure 3.8 Simulated fields under condition Cryo-Re30: (a) equivalent plastic strain; (b) total dislocation density; (c) grain size.

A quantitative assessment of the simulation results was performed for the profiles of equivalent plastic strain, total dislocation density, and grain size along the depth from machined surface. Figure 3.9 shows the simulated averaged profiles with the cross-sectional microstructure of the machined surface. For cryogenic machining conditions of Cryo-Re70 and Cryo-Re30, the simulation results show high equivalent plastic strains of about 4.2 and 4, high dislocation densities of 4.15 and 3.8×10^{15} m^{-2}, and refined grain sizes of 62 and 64 nm, respectively. The simulated UFG layer thickness is 18 and 14 μm, respectively, which agree well with the measured UFG layer thickness from the experiments. The refined grain size was measured to be 30-60 nm by AFM in the UFG layer on the machined surface for Cryo-Re70. In comparison, the model simulated a grain size was refined to a minimum of 62 nm on the machined surface, which matches well with the experimental measurement. For materials below the UFG layer, the simulated equivalent plastic strain and dislocation density diminished quickly and grain size maintained unchanged as the initial size of 12 μm. These findings are very similar to those observed microstructures in Figure 3.9d, which clearly shows the UFG layer above the unaffected bulk material.

The effects of cryogenic cooling and tool cutting edge on the machined surface integrity are also examined through the comparison of the simulation results and experimental measurements. For the case of Dry-Re30, a slim UFG layer of 2 μm was predicted for a tool edge radius of 30 μm; for the case of Cryo-Re30 with the aid of cryogenic cooling, the UFG layer thickness was predicted to increase drastically to 14 μm. Similarly, for the tool edge radius of 70 μm, cryogenic cooling helps increase the UFG layer thickness from 11 to 18 μm. In addition, by the comparison of equivalent

plastic strain and dislocation density, it can be easily found while the greater edge radius introduces more plastic deformation for a thicker affected layer, the cryogenic cooling was the dominant factor of the grain refinement in this machining configuration by introducing more severe plastic deformation and dislocations.

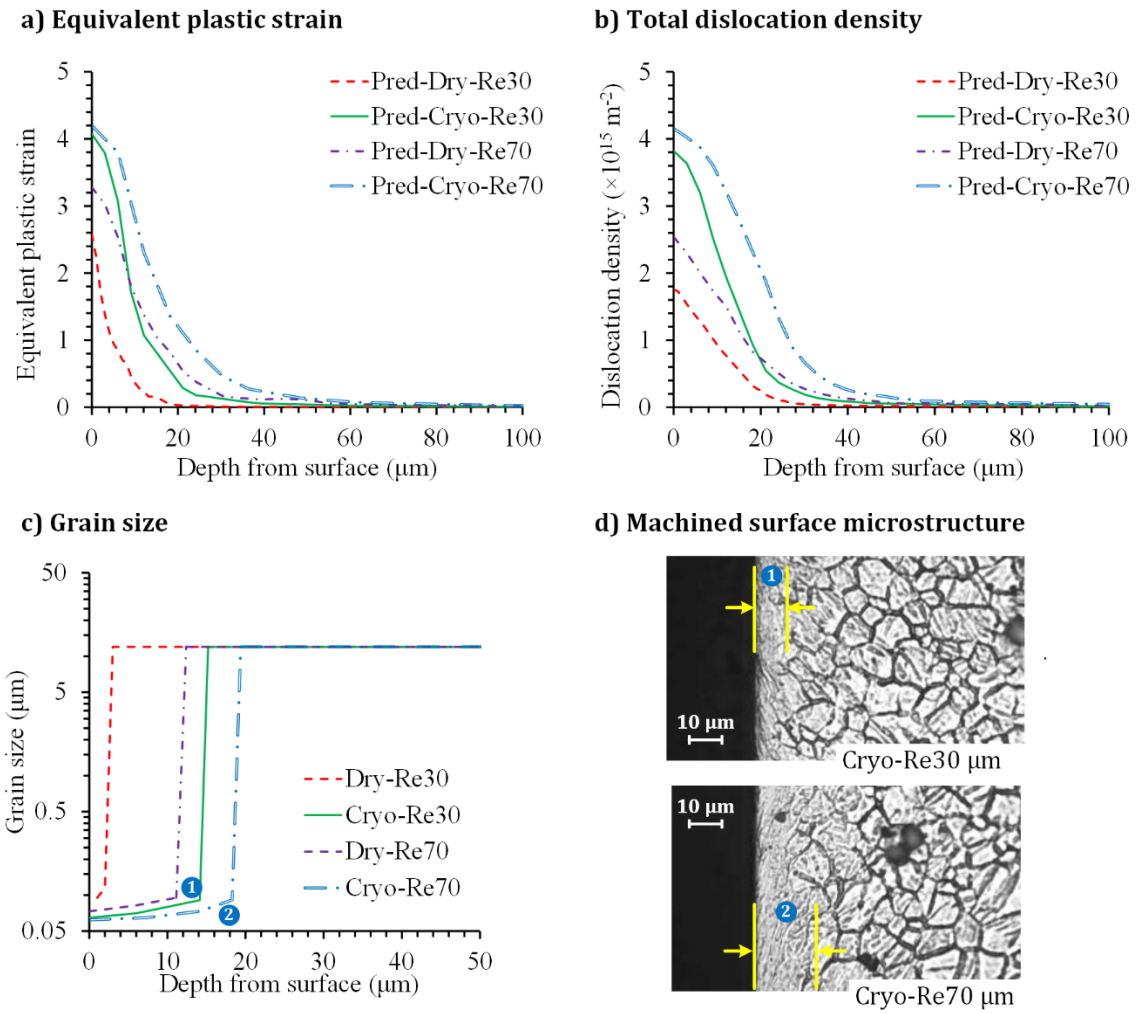

Figure 3.9 Simulated profiles of: (a) equivalent plastic strain; (b) total dislocation density; (c) grain size; (d) machined subsurface micrographs from Pu et al. [53].

3.5.3 Microhardness

Figure 3.10 shows the simulated microhardness distribution beneath the machined surface and in the chip for the cryogenic machining condition of Cryo-Re30. Hardness increases greatly on the machined surface and along the tool-chip interface, which has a distribution similar to those for strains and dislocation densities, as can be seen in Figure 3.8a-b. The initial microhardness of the bulk matrix material was 0.513 ± 0.039 GPa. The predicted microhardness within the top 10 μm were increased to the level of 0.9 GPa (an increase by 75%) on both machined surface and tool-chip interface.

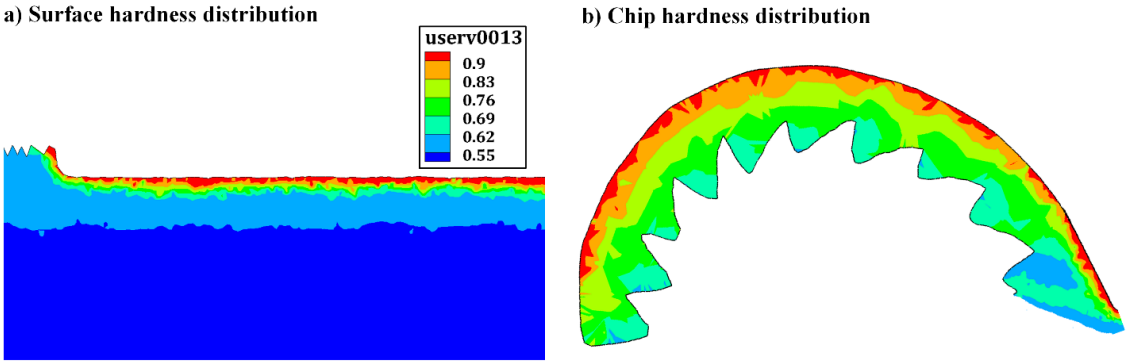

Figure 3.10 Simulated microhardness distribution for condition Cryo-Re30 in (a) machined surface and (b) chip.

Figure 3.11 shows the variation of microhardness change along the depth below the machined surface for the four difference experimental conditions. The simulated UFG layers under different conditions were highlighted by the rectangular shade in blue or red, corresponding to cryogenic cutting and dry cutting, respectively. Under all conditions, the surface hardness was significantly increased within the UFG layer, while it gradually

diminished at a depth of 100 µm. The largest surface hardness of 0.947 ± 0.055 GPa was measured under the condition of Cryo-Re70. The experimental measurements also showed surface hardness could be increased by applying cryogenic cooling or a larger edge radius. Obviously, the cryogenic cooling had a more significant effect on the increase of surface hardness. Compared with the experimental data, all the simulation results successfully captured the trend of microhardness depth profile from the machined surface, as well as the greater effect of cryogenic cooling on the increase of surface hardness.

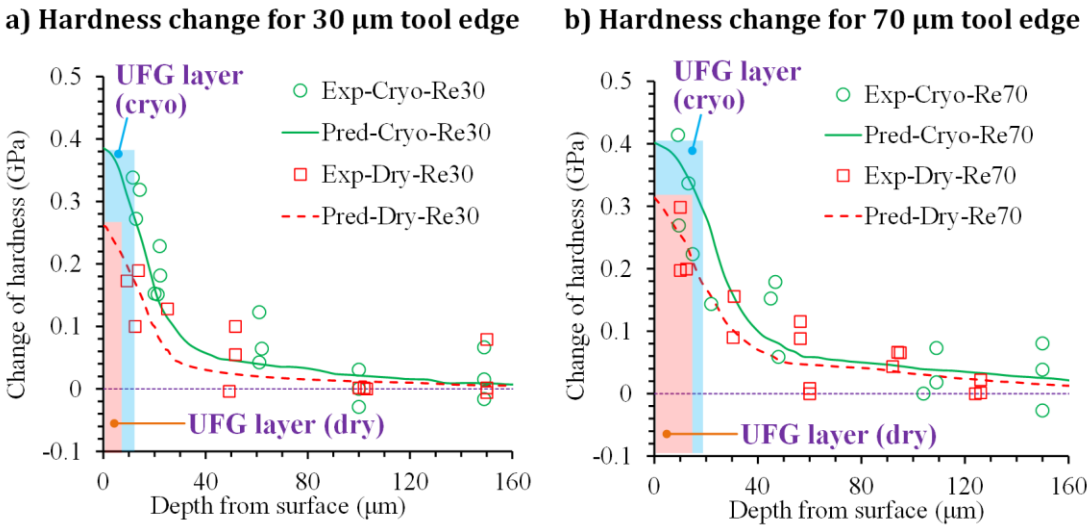

Figure 3.11 Simulated microhardness profiles compared with the experimental measurements in [53].

3.5.4 Residual Stresses

Figure 3.12 shows the simulated circumferential residual stress distribution over the whole cutting length of Cryo-Re70. It was found that the residual stress was

compressive on the machined surface. The magnitude of the residual stress continuously decreased along the depth. The darker blue domains at both left and right ends correspond to the stress concentration at the edge corners of the workpiece during relaxation. Quantitative assessments were carried out with profiles extracted within the boxed domain as shown in Figure 3.12.

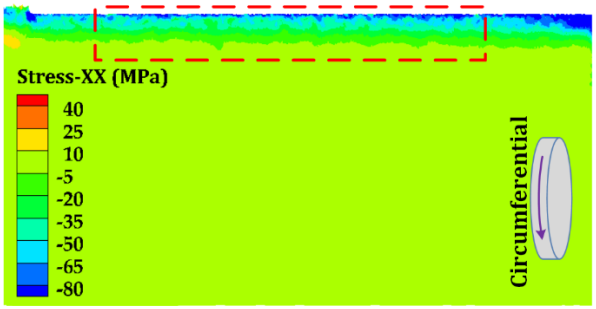

Figure 3.12 Simulated circumferential residual stress fields for conditions Cryo-Re70.

Figure 3.13 shows the measured and simulated residual stresses in the circumferential and axial directions after both dry and cryogenic machining. Due to a large penetration depth (about 25 μm) of X-ray in Mg alloy, the residual stresses measured on the surfaces were corrected by shifting 12.5 μm below the machined surface. For a 30 μm edge radius tool, compressive circumferential residual stresses were induced as deep as 150 μm below the machined surface under both dry and cryogenic conditions. The peak compressive stress in dry machining was about 40 MPa at a depth of 30 μm below the surface, which was increased to about 50-70 MPa within the same depth by cryogenic machining. For axial residual stress, tensile residual stress was predicted for the dry machining condition of Dry-Re30, which agreed well with the measurement. Tensile residual stress of 37 MPa was generated at 12.5 μm deep in the

axial direction. By implementing cryogenic machining, the residual stress turned to compressive with a magnitude of 39 MPa. When the edge radius was increased to 70 µm, the circumferential residual stress was also compressive for both dry and cryogenic machining, but penetrated 120 µm deeper than those using smaller tool edge radius. For the axial direction, cryogenic cooling made the residual stress more compressive by 50 MPa. Comparing the cryogenic machining results in axial stresses, a much thicker penetration of compressive residual stress was obtained using a larger edge radius. The results revealed a great opportunity to use cryogenic cooling combined with large edge radius tools to induce large and deep compressive residual stresses on the machined surface.

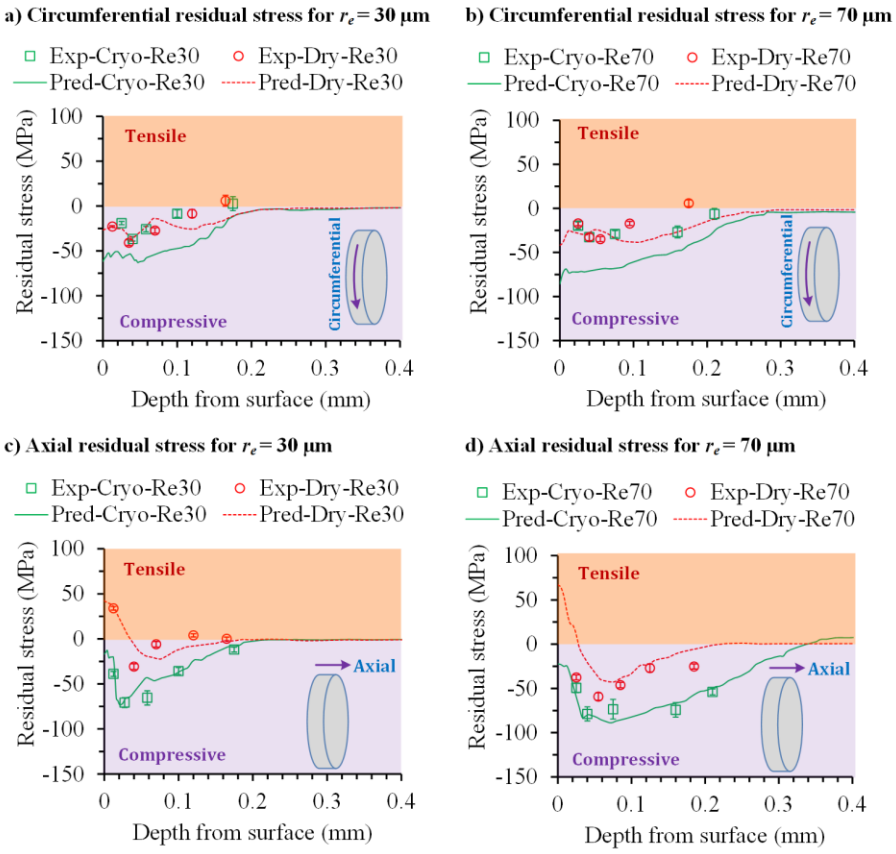

Figure 3.13 Simulated residual stress depth profiles compared with measurements in [53].

3.5.5 Discussions on Slip/Twinning Transition

The transition between slip and twinning during cryogenic machining was investigated with the model. The effect of twinning response can be demonstrated by comparing the subsurface microstructure and texture before and after the cryogenic machining experiments. Figure 3.14a shows the initial microstructure of the specimen before cryogenic machining. Twinning lamellas were found in a surface layer above the dashed line, while no twinning can be seen for the area below. These twinning lamellas were induced by the sample preparation process of milling. Figure 3.14b shows the microstructure produced by cryogenic machining test of Cryo-Re30. A featureless UFG layer existed 10-14 μm just below the machined surface, and no signs of twinning can be found for the topmost 15 μm. However, a large amount of twinning lamellas can be seen from 15 to 80 μm below the machined surface. Comparing the micrographs, cryogenic machining induced a topmost UFG layer accompanied by resolving the twinning lamellas, and introduced twinning lamellas in the region from 15 to 80 μm below the surface.

Figure 3.14c further examined the evolution of the crystallographic orientations on the disc surface before (initial) and after machining (Dry-Re30 & Cryo-Re30). The highest peak for all the conditions corresponds to the plane of $(10\bar{1}1)$, one of the two major twinning systems of Mg alloys [52]. Both of the plane of (0002) and $(10\bar{1}0)$ two slip systems of Mg alloys [52]. After the cryogenic machining, the intensity of plane of (0002) was drastically increased, while the intensity decreased in $(10\bar{1}1)$ plane from the initial specimen to the cryogenic cut surface indicated the twinning lamellas were reduced by cryogenic machining in the surface layer. The intensity increased in the plane

of (0002) plane and $(10\bar{1}0)$ indicated that more slip systems were activated due to high strain rate SPD in cryogenic machining. Also, as the large penetration depth of the X-ray in Mg, the great amount of twinning system signal was picked from the lower less strained domain, making the constant high intensity peak for the plane of $(10\bar{1}1)$ for the condition of cryogenic machining.

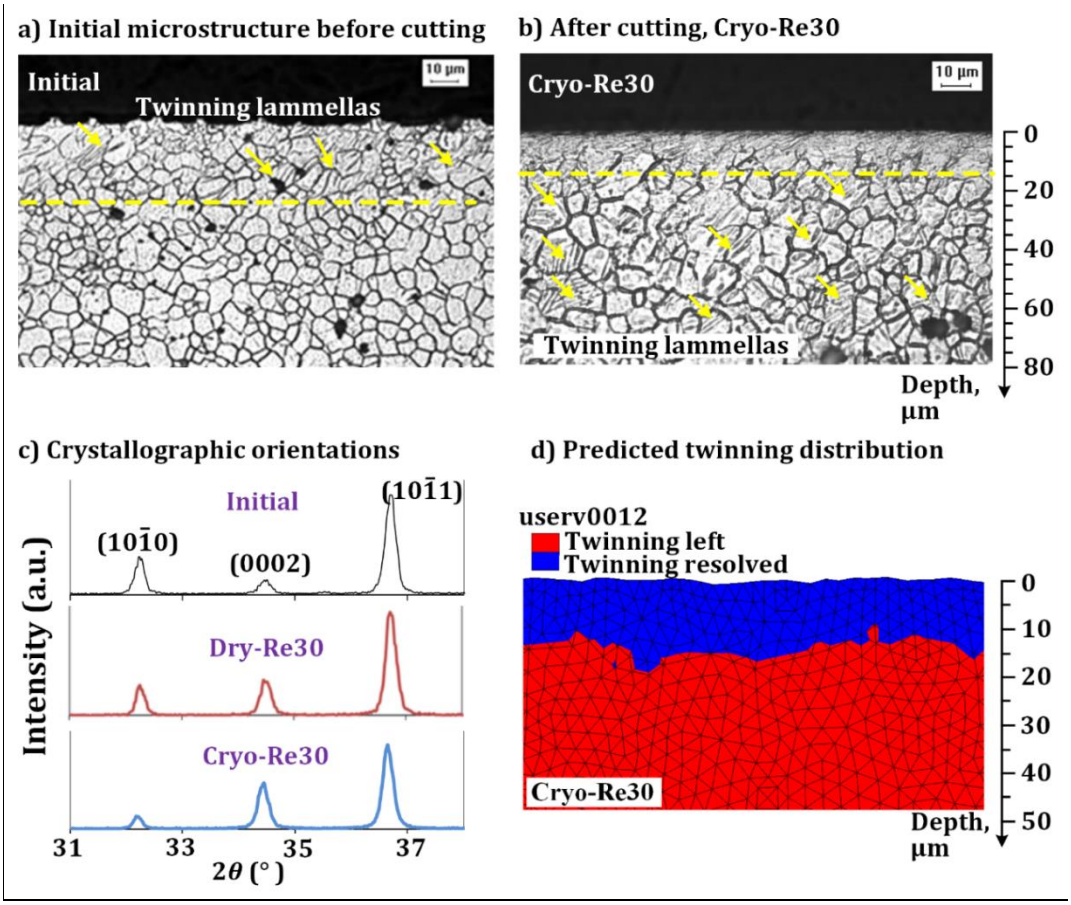

Figure 3.14 Comparison of the predicted twinning distribution with the microstructure beneath the machined surface of Cryo-Re30 (raw images adopted from Pu et al. [53]).

Figure 3.14d shows the simulated twinning distribution by the aforementioned deformation mechanism index within an 80 μm thick subsurface domain. Model predicted a 20 μm thick layer with twinning lamellas resolved, while twinning lamellas

remained from 20 to 80 μm from the machined surface. The simulated transition level of 20 μm deep was very close to the transition level shown in Figure 3.14b. Therefore, this model can capture the twinning generation and twinning/slip transition very well in the plastic deformation of AZ31B Mg alloy.

3.6 Summary

A 2D FE model is developed in AdvantEdge™ to simulate the enhanced surface integrity of AZ31B Mg alloy by cryogenic machining in two cutting passes, in terms of nanocrystalline grain refinement, increased surface hardness, and compressive residual stress. Based on both slip and twinning mechanisms, a novel physics-based constitutive model was developed and implemented as a user-defined subroutine to capture material response and grain refinement of AZ31B Mg alloy under cryogenic conditions.

Compared with micrographs and experimental measurement from Pu et al. [53], quantitative assessments were carried out with simulated in-depth profiles for all solution fields, i.e., temperature, plastic strain, dislocation density, grain size, UFG layer thickness, microhardness change, and residual stress distribution. Comparing microstructure and texture below the machined surface before and after cryogenic machining, the FE model also accurately predicted the slip/twinning transition and twinning lamellas resolving in the topmost surface layer of about 20 μm in thickness.

This FE analysis has successfully simulated the complex microstructure evolution of an HCP material in an SPD process under dynamic strain rates. The simulated surface integrity attributes agree with the experimental measurements and observations very well.

CHAPTER 4.
SURFACE NANOCRYSTALLIZATION AND WHITE ETCHING LAYER FORMATION DURING HARD DRILLING

In this chapter, a thorough review of microstructural analyses is firstly presented for the white etching layer formed during SPD processes, and the formation mechanism for the nanocrystalline structure observed in WEL are determined for the machining processes of hardened steels. A new dislocation density-based grain refinement model is then developed to model the nanocrystalline formation mechanisms during a hard drilling process, characterized by high temperatures, severe plastic strains and high strain rates. Finally, the dislocation density-based grain refinement model is implemented in a metallo-thermo-mechanically coupled FE cutting model to simulate microstructure evolution near the machined surface during drilling of hardened AISI 1060 steel with a typical hardness of 64 HRC.

4.1 Review of WEL Formation and Grain Refinement Mechanisms of Steels

4.1.1 WEL formation and grain refinement during machining processes

White etching layer has been widely observed on the final surface of hardened steels by machining [77–86]. Li et al. [86] systematically investigated the hole surface microstructures produced by hard drilling of various carbon steels under different machining process parameters. Sintered carbide drills (5 mm in diameter) were used in the drilling experiments with oil mist as coolant. The effects of drilling process parameters and work material microstructures on WEL formation and final surface microstructures were characterized by an extensive micrograph analysis using scanning

electron microscopy (SEM), transmission electron microscopy (TEM), and X-ray diffraction (XRD). The work materials they tested in this study included Fe-0.56% C, Fe-0.80% C, and commercial SUJ2 bearing steel alloys. To determine the effects of initial microstructure on final machined surface microstructure, the work materials were prepared under different heat treatment processes prior to cutting experiments to obtain different microstructures including ferrite, pearlite, martensite, and tempered martensite. The microhardness of these work materials varied from 2.9 GPa to 8.1 GPa corresponding to different microstructures. To determine the effects of cutting process parameters, drilling experiments were performed on quenched Fe-0.56% C steel alloy with a martensitic structure using cutting speeds of 20-100 m/min and feed rates of 0.01-0.1 mm/rev. Their experiments found that WEL formation can be enhanced by increasing the feed rate or cutting speed. Overall, a gradient WEL microstructure is usually observed near the machined surface. Typically, the topmost layer of WEL is featureless under optical microscope, but can be characterized as nanocrystalline using advanced SEM or TEM. Beneath the nanocrystalline layer is a layer with a mixed structure of nanoscale to submicron-sized grains. Retained austenite can be formed from solid phase transformation due to the intensive thermomechanical loadings during the hard drilling process. Their results reported that a greater initial microstructure hardness can enhance the formation of both topmost nanocrystalline layer and overall WEL microstructure.

Effects of the cutting process parameters have been systematically evaluated on the WEL formation and microstructure evolution during hard drilling. Figure 4.1 shows the longitudinal section view (the section parallel to the hole axis) SEM micrographs of typical surface microstructures achieved under different feed rates for drilling of

quenched Fe-0.56% C steel alloy with an initial martensitic structure and microhardness of 7.8 GPa. WELs were observed on the hole surface for all the applied feed rates, which had a clear boundary distinguishable from the unaffected bulk material. The thickness of WEL increased from 7.5 µm to 13 µm as the feed rate increased from 0.01 mm/rev to 0.1 mm/rev. Figure 4.2 discusses the effects of cutting speed and shows the longitudinal section view SEM micrographs of surface microstructures of the same martensitic material. For a low cutting speed of 20 m/min (Figure 4.2a), a deformed structure layer can be observed near the drilled hole surface, while no WEL was formed. For cutting at moderate to high cutting speeds, WELs formed at the hole surfaces, and their thickness increased from 8 µm to 15 µm as the cutting speed increased from 60 to 100 m/min. A similar relationship between WEL and cutting process parameters has also been determined for SUJ2 steel.

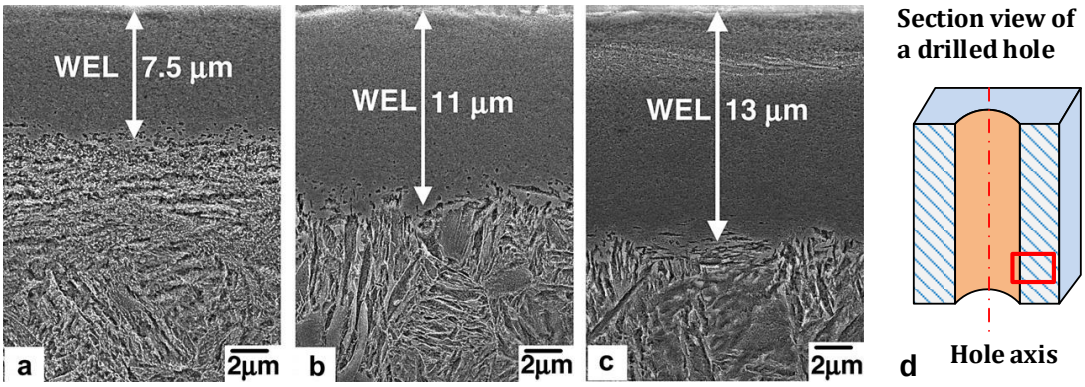

Figure 4.1 SEM micrographs near the hole surface after drilling at different feed rates under the same cutting speed of 80 m/min: (a) 0.01 mm/rev, (b) 0.05 mm/rev and (c) 0.1 mm/rev (micrographs adopted from Li et al. [86]); (d) schematic of the location of the section.

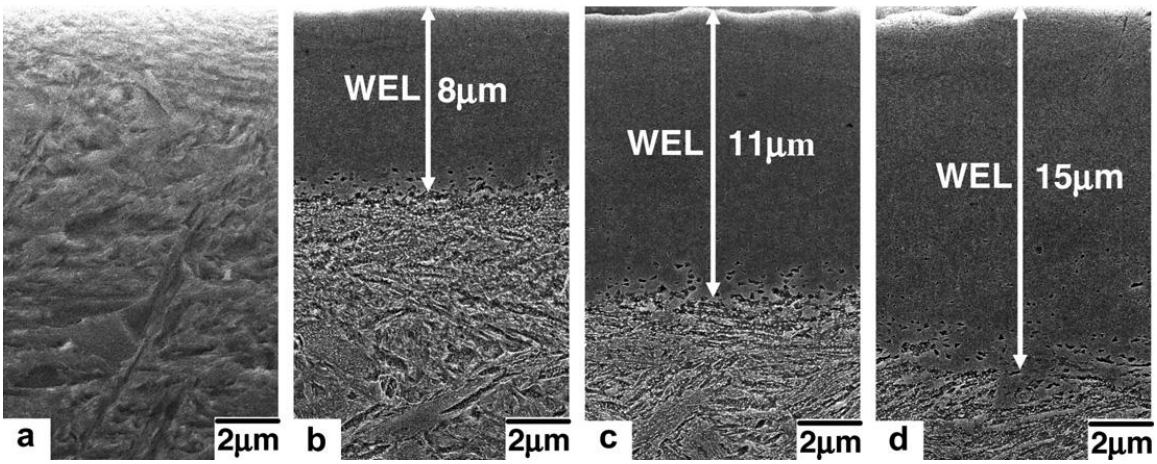

Figure 4.2 SEM micrographs near the hole surface after drilling at different cutting speeds under the same feed rate of 0.05 mm/rev: (a) 20 m/min, (b) 60 m/min, (c) 80 m/min and (d) 100 m/min (micrographs adopted from Li et al. [86]).

Effects of the initial work material microstructure have been systematically evaluated on WEL formation and grain refinement during hard drilling. WELs with similar microstructural characteristics were obtained for all of the work materials except for Fe–0.56% C steel alloy with a pearlite structure and a lowest hardness of 2.9 GPa. Figure 4.3a shows a high-resolution SEM micrograph of the machined surface microstructure in the section perpendicular to the hole axis for pearlite Fe-0.56% C steel alloy. It can be observed that cementite plates became thinner, and the spacing between cementite plates decreased gradually when it was close to the drilled surface. The topmost layer was significantly sheared along the cutting direction. This indicates that severe plastic deformation occurred near the drilled hole surface. As shown in TEM analysis (Figure 4.3b), a high dislocation density can be observed on the topmost hole surface layer. The selected area diffraction (SAD) pattern in the TEM micrograph indicates that the microstructure was composed of body-centered cubic (BCC) ferrite and

cementite, i.e., no phase transformation occurred. Irregularly shaped grains with a grain size of several hundred nanometers can be seen in the dark-field TEM image as shown in Figure 4.3c. This also indicates that strong deformation occurred near the surface of the hole.

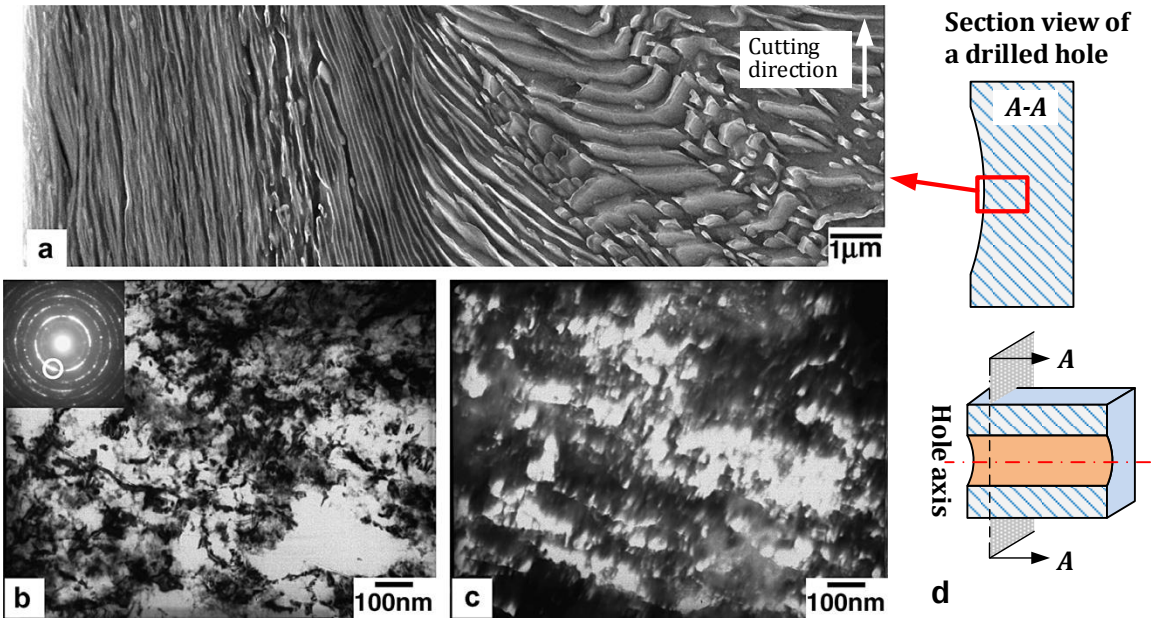

Figure 4.3 Micrograph near the surface of a hole in Fe–0.56% C steel with a pearlite structure (initial matrix hardness of 2.9 GPa) after drilling (80 m/min, 0.05 mm/rev): (a) SEM image; (b) TEM bright-field image and corresponding SAD pattern; (c) TEM dark-field image (micrographs adopted from Li et al. [86]); (d) schematic of the location of the section.

Work material with the highest initial microhardness, i.e., as-quenched martensitic Fe–0.56% C steel alloy with a microhardness of 7.8-8.1 GPa, led to the thickest WELs by hard drilling. Figure 4.4a shows high-resolution SEM micrographs near the sectioned surface of a hole in the as-quenched martensitic Fe–0.56% C steel. A

sharp boundary can be observed between the WEL and the microstructure beneath it. Within the WEL, the microstructure gradually changed as the depth increased. A featureless microstructure layer can be observed on the topmost layer. Beneath this featureless layer, sporadic etched areas can be observed, which are surrounded by smooth contrast areas. Very tiny etched areas can be observed in the topmost layer, which is less 100 nm in size. With the increase of the depth, the size of these etched areas gradually increased to about 0.3-0.5 μm in size near the bottom of the WEL.

More details in microstructural changes in WEL were characterized using TEM. The TEM micrograph in Figure 4.4b shows that the topmost featureless layer consisted of equiaxed grains about 20-50 nm in size. The continuous rings of the SAD pattern indicate the material was polycrystalline with random grain orientations. Strong diffraction rings were found for the BCC ferrite structure from matrix material, and austenite can also be interpreted from several diffraction rings. Beneath the nanocrystalline structure, both nano-sized grains and larger grains about 100–200 nm in size can be observed in Figure 4.4c. The SAD pattern shows that the microstructure can be indexed as austenite, twined martensite, and ferrite. Since the initial microstructure consisted of lath martensite, it is considered that twinned martensites were formed during the cooling phase after drilling phase. Notably, these TEM bright-field images showed that dislocation density drastically decreased in WEL when comparing them with those in Figure 4.3b-c.

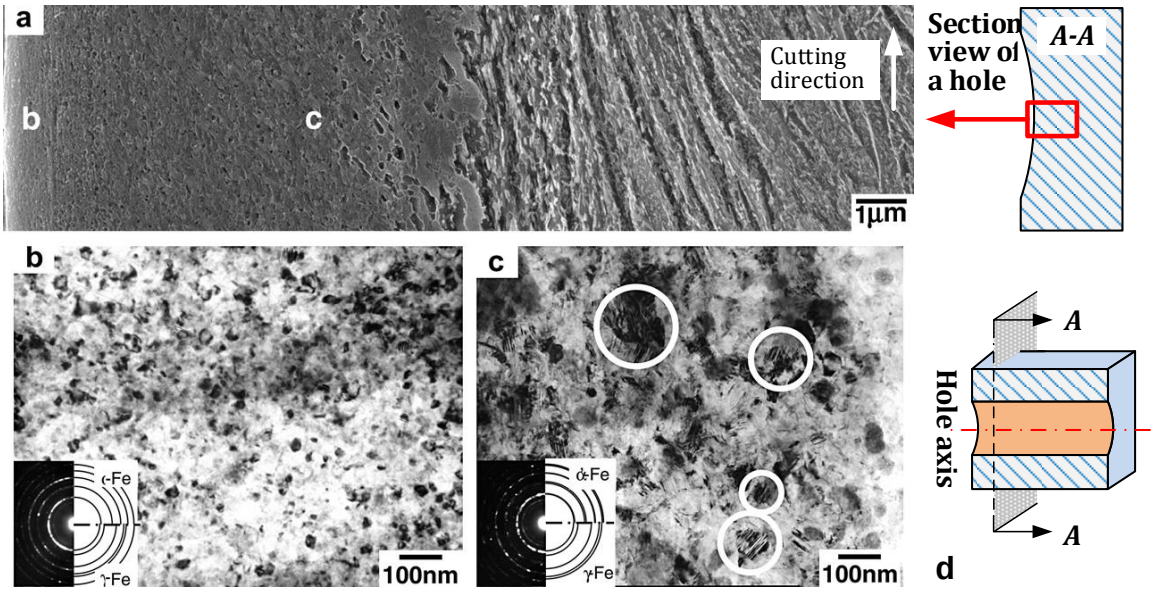

Figure 4.4 Micrograph near surface of a hole in quenched Fe–0.56% C steel with a martensite structure (initial matrix hardness of 7.8 GPa) after drilling (80 m/min, 0.05 mm/rev): (a) SEM image; (b) TEM bright-field images and corresponding SAD patterns in the nanocrystalline layer; (c) TEM bright-field images and corresponding SAD patterns near the bottom of WEL (micrographs adopted from Li et al. [86]); (d) schematic of the location of the section.

Phase composition of drilled hole surface was further investigated using XRD. Figure 4.5 shows the XRD spectra taken from the surface of as-quenched martensitic Fe–0.56% C steel specimens before and after drilling experiments. For the XRD data of surface before drilling, high-intensity and low-intensity peaks can be observed for α'-phase martensite and retained austenite, respectively. The volume fraction of retained austenite was determined to be less than 1% through a quantitative analysis of the XRD data. After drilling, the volume fraction of austenite of machined surface substantially increased to about 15% by the drilling operation using a cutting speed of 80 m/min and

feed of 0.05 mm/rev. It was found that the higher volume fraction of austenite corresponded well to the thicker WEL. Therefore, the austenite present on the surface of a drilled hole resulted from phase transformation from as-quenched martensite to austenite during drilling. Considering DPT as the dominant mechanism of WEL formation, numerical models have been developed in literature to determine the thickness of WEL based on thermal modeling of the hardened steels machining process [79,104–107]. However, deformation-driven grain refinement has not been considered in these prior researches due to a lack of systematic microstructural analyses on this critical phenomenon.

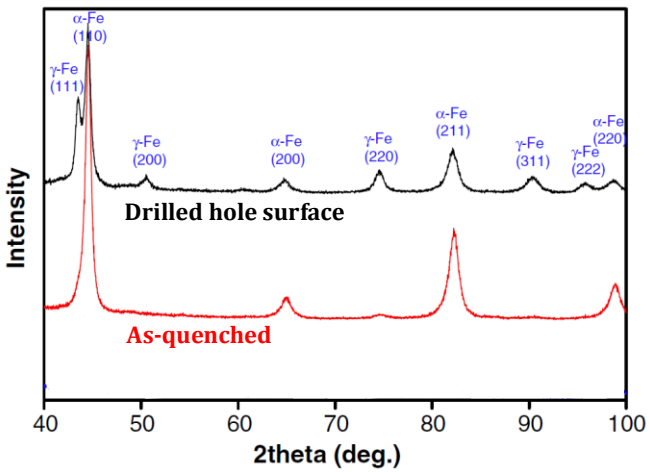

Figure 4.5 XRD spectra on the surface of as-quenched Fe–0.56% C steel before and after drilling experiments (80 m/min, 0.05 mm/rev, data adopted from Li et al. [86]).

Base on the systematical microstructural analysis of hard drilling WEL formation, Li et al. [86] concluded that the formation of nanocrystalline and UFG structures in WEL are attributed to a combined effect of severe plastic deformation and dynamic phase transformation with a large strain gradient and a high strain rate. Geometrically necessary

dislocations were developed to ensure the compatibility of deformation and accommodate large strain gradients in the drilled surface. The high-density dislocations can evolve into cell or grain boundaries under the large strain deformation by dynamic recovery, thereby refining the structure. Moreover, the high density of grain boundaries and dislocations provided a very large number of nucleation sites during DPT, which may be expected to lead to further refinement of the microstructure.

Similar WEL attributes with nanocrystalline structure and transformed retained austenite were also characterized by Barry and Byrne [80] for hard turning processes of two different steels, namely, carbon steel alloy of Fe-0.80%C and medium-carbon low-alloy BS 817M40 steel (equivalent to AISI 4340 steel). A shallow WEL (< 2-3 μm) appeared on the machined surface for both steels when machined with worn cutting tools, but no WEL can be found on the surfaces machined using new cutting tools. Retained austenite was observed in all TEM SAD patterns of the WEL microstructure for both steels, and its volume fraction increased with an increasing tool wear area. Their research indicated that retained austenite in the machined surface resulted from a reverse martensitic transformation during the machining process. The diffuse continuous rings of cementite reflections indicated a significant refinement of cementite. For materials undergoing plastic deformation, the rate of dissolution of carbides is likely to be greater due to mechanisms such as a shearing of the austenitic envelope surrounding carbide particles and generation of numerous dislocations and vacancies, which can act as high-diffusivity paths. Analyzed using TEM, the machined surface microstructures in WEL of both steels were characterized as very fine and misoriented cells. For Fe-0.8%C steel alloy, the average cell size was several tens of nanometers, and in particular, cells under

10 nm were also visible. For BS 817M40 steel, the average grain size was coarser than that in the machined surface of Fe-0.8%C steel; several larger cells of 200 nm in size were observed.

Based on the micrographic observation of slightly coarser structure and several larger cells for BS 817M40 steel, Barry and Byrne argued for the possible occurrence of dynamic recrystallization during cutting, which may have happened to steels at elevated temperatures due to a decrease in their stacking fault energy. However, without any direct experimental evidence, their hypothesis was mainly inferred from literature data for other manufacturing processes. Barry and Byrne reviewed the experimental data of nanocrystalline microstructure formation in adiabatic shear bands formed during high-speed deformation of AISI 4340 [121] steel and HY-100 steel [123]. Severe plastic deformation accompanied with a strong dynamic recovery (DRV) effect was considered as the primary mechanism to form the nanostructures during these processes, while occurrence of DRX was not evident from the resultant microstructures. However, Barry and Byrne argued that DRX may still occur for a steel alloy with a decrease in stacking fault energy induced by the reverse martensitic transformation, which is driven by intensive heat generation during hard turning. The SFE of retained austenite (FCC iron) at 1000 °C was much lower than that of martensite [188], under which condition they argued that dynamic crystallization could be possible as suggested by McQueen [189]. Nonetheless, Barry and Byrne noted that the kinetics of conventional discontinuous dynamic recrystallization (dDRX) by thermal diffusion were too slow to form the nanocrystalline or UFG structures during rapid cutting processes.

Previous microstructure analysis using TEM and XRD has shown that nanocrystalline structure and retained austenite from reverse martensitic transformation were evident for WEL formation on the machined surface of hardened steels. Therefore, both deformation-driven grain refinement and thermally driven dynamic phase transformation should be considered for modeling microstructure evolution during machining of hardened steels. However, controversies still exist in literature about the mechanisms and effects of grain refinement. In order to consider the coupled effects of deformation-driven grain refinement and thermally driven dynamic phase transformation, it is necessary to review, categorize and analyze other important experimental data and substantial evidences available in literature. In next section, a thorough review is therefore conducted for the process mechanisms of nanocrystallization of hardened steels during other SPD processes.

4.1.2 WEL and Nanocrystallization during Other SPD Processes

Severe plastic deformation has been widely acknowledged as an effective method to produce UFG and nanocrystalline materials [137]. High pressure torsion (HPT) and equal-channel angular pressing (ECAP) are two typical SPD processes to produce UFG and nanocrystalline microstructures [134–138]. However, their processing temperature is usually lower than 40~50% of the material melting point (0.4~0.5T_m), and a low strain rate is usually applied during these two processes. In addition, WEL is usually not formed from these processes. Hence, the review in this section focuses on a review of processes those generate nanocrystalline WEL including adiabatic shear band formation, sliding wear, ball drop test, ball milling, ultrasonic or air blast shot peening, and laser shot

peening (LSP). During these processes, high strain rates of about 10^3~10^7 s^{-1} can be achieved, which are comparable to the strain rate typical for the drilling process.

Nanocrystalline WEL structures of adiabatic shear bands have been extensively studied for various SPD processes, such as split Hopkinson compression bar and explosion deformation, for AISI 4340 steel [119–122] and HY-100 [123]. High strain rates were usually achieved ranging from 10^3 s^{-1} to 8×10^5 s^{-1}, and a short mechanical loading duration of about 50 μs was applied in these processes. WEL with similar grain refinement structures have been observed in these adiabatic shear bands, which has been observed for many decades since a study conducted by Zener and Hollomon in 1944 [190]. Their results showed significant effects of mechanical deformation on WEL formation, such as ultrafine grain structures with a typical grain size of 0.2-0.5 μm achieved from rolling-sliding friction [123]; structures with elongated subgrains (35-90 nm wide and 500-800 nm long) achieved using torsional Kolsky bar [121]; nanocrystalline structures or dispersed structures without clear grain boundary using split Hopkinson compression bar or explosion deformation [119,120,122]. No signs of recrystallized grains can be found in these adiabatic shear bands, and hence no clear evidence existed to support the occurrence of dynamic recrystallization in all of these studies. In addition, they did not find any direct evidence for reverse martensitic transformation from the parent phase to untampered martensite within the adiabatic shear bands, even though experimental measurements often showed a high process temperature on the level of 600 °C. The carbides in the original work materials were found to be dissolved in the dislocation sites within the shear bands. The mechanically refined nanocrystalline structure without carbides prevented preferential etching during sample

preparation for microstructure imaging, which made the WEL appears featureless and white under an optical microscope [119,120]. Based on these experimental evidence, they concluded that severe plastic deformation accompanied with a significant dynamic recovery effect was considered as the primary metallurgical process to form these refined WEL microstructures [119–123].

Nanocrystalline WEL structures has been obtained by various SPD surface treatment processes. Umemoto and his co-workers systematically investigated the formation of nanocrystalline structure in steels during multiple surface treatment processes, such as sliding wear, ball drop test, ultrasonic or air blast shot peening, and ball milling [116–118,125]. Equiaxed nanograined regions appeared near the specimen surface, and a dislocated cell structured region appeared interior of specimens. Annealed at 874 K for one hour, the nanocrystalline layers showed slow grain growth without recrystallization, whereas the deformed structures below the nanocrystalline layer were completely recrystallized. They concluded that the deformation-induced nanograined regions in steels have the following common specific characteristics: (1) grains smaller than 100 nm and low dislocation density interior of grains, (2) extremely high hardness, (3) dissolution of cementite when it exists, and (4) no recrystallization and slow grain growth by annealing. These phenomena were also observed in the ball milling study of pearlite steel (Fe-0.85% C) [127], sandblast of 304 stainless steel [126], and rolling-sliding of pearlite steel (Fe-0.6~0.8% C) [124]. Notably, occurrence of DRX was not observed in all these studies.

Surface nanocrystallization has also been reported for austenite stainless steels subjected to extremely high-strain rate, about 10^7 s^{-1}, laser shock peening process [128–

133]. The mechanism of surface nanocrystallization induced by LSP can be summarized as follows. High-density dislocations were rapidly generated at the wave front by the multidirectional shockwave loads from reflection and refraction. When the material stress caused by dislocation pile-up increased to a certain level, mechanical twins (MTs) were generated. The boundaries of these MTs were almost parallel, and divided the original coarse grains into thin twin matrix lamellae at the top surface. As the shockwave pressure further increased, intercrossed MTs were formed by excessive accumulated distortions. Formation of intercrossed MTs were also coupled with deformation-induced martensitic (DIM) transformation. Due to the strong coupling interactions of MT and DIM induced by multiple LSP impacts, a nanocrystalline surface layer with a size of 50-300 nm was formed on the surface of AISI 304SS.

Nanocrystalline structures have also been achieved for carbon steels processed using low-strain rate SPD processes such as HPT and ECAP [134–138]. The grains in the nanostructured domain were separated by dense dislocation walls, which exhibited continuous rings in TEM SAD patterns. Strain-induced cementite dissolution was also observed, which was determined as the mechanism of nanostructure formation.

4.1.3 Discussions

Formation of nanocrystalline WEL structures, especially for surface nanocrystalline structures, has been discussed in the previous section for various SPD processes with a wide range of strain rates between 0.5 s^{-1} and 10^7 s^{-1}, process duration ranging from 50 μs to hours, and temperature ranging from cryogenic condition to hot forming condition of $0.8T_m$. These data in literature provides a good basis for analysis of

hard machining of steels. During machining processes of hardened steels and other difficult-to-machine alloys, the machine tool often induces large plastic strains (e.g., shear strain of ~5-10) not only inside the chip but also along the machined surface. The chip forms at a high strain rate, typically on the order of 10^5 s^{-1}, for typical cutting speeds of 100-300 m/min. A high temperature gradient also exists in the cutting zone, characterized by a rapid heating rate of 10^5-10^6 °C/s and a fast cooling rate of 10^3-10^4 °C/s. By comparison of the process loading conditions, machining process of harden steels can be considered as a specific SPD process. Therefore, the microstructure evolution mechanisms of steels during hard machining must be consisted with those major mechanisms during SPD processes.

Based on the extensive review in Sections 4.1.1 and 4.1.2, it is concluded that the surface nanocrystallization and WEL formation of steels during the machining process are governed by both SPD-induced grain refinement accompanied with a strong DRV effect and thermally driven DPT. Under low cutting temperature conditions, mechanical deformation plays the dominant role on microstructure evolution, while the effect of DPT diminishes. Under high cutting temperature conditions due to the intensive heat generation, both mechanical deformation and thermally driven DPT contribute the final machined surface microstructures. The accumulated high dislocation density and newly formed grain boundaries due to mechanical deformation help provide nucleation sites for solid-state phase transformation. Twining may also play an important role under certain process conditions, such as laser shock peening of austenite stainless steels and cryogenic cutting of Mg alloys discussed in Chapter 3. Cementite may be dissolved in the topmost nanocrystalline layer, providing a good thermal stability even at elevated temperatures.

The extensive microstructure analysis data reviewed in previous sections shows that dynamic recrystallization does not contribute to machined surface nanocrystallization or WEL formation. No signs of recrystallized grains can be found in these surface structures, particularly in WEL, and hence no experimental evidence exists in literature to support the occurrence of DRX in any of these machining or SPD studies. Therefore, in this study, it is concluded that DRX, especially by the form of dDRX induced by thermal diffusion, is not the mechanism of machined surface nanocrystallization or grain refinement. Most of the previous modeling efforts in metal cutting [19,22,23,47,108–114] incorrectly assumed DRX as the primary mechanism to form the nanocrystalline and UFG structure in the machined surface without any support of direct experimental evidence. In addition, their modeling approaches often applied the kinetics of dDRX by thermal diffusion, which is too slow to form the nanocrystalline or UFG structures during rapid cutting processes.

In this study, a new grain refinement kinetics model based on the evolution of dislocation density will be developed to simulate both SPD-induced grain refinement associated with a strong DRV effect and thermally driven DPT simultaneously during hard machining of steels. This new model will consider the decrease in dislocation density in the topmost layer of WEL, which has been experimentally characterized. To the author's best knowledge, no existing model efforts have been undertaken in literature to capture this comprehensive mechanically, thermally, and metallurgically coupled phenomenon. In this work, a metallo-thermo-mechanically coupled grain refinement model will be developed to simulate the microstructure evolution of hardened steels during machining.

4.2 Metallo-Thermo-Mechanically Coupled Grain Refinement Model

A metallo-thermo-mechanically coupled grain refinement model is developed to simulate the WEL formation and surface nanocrystalline during the drilling process of hardened AISI 1060 steel. To model the formation of the WEL, the phase transformation kinetics is solved simultaneously during the thermomechanical process. To model both SPD-induced grain refinement associated with a strong DRV effect and thermally driven DPT effects in the WEL, the previously developed SPD-induced dislocation density-based grain refinement model was extended with effect of DPT on dislocation density evolution. The DPT is modeled by the thermally driven DPT kinetics in this study. The microhardness prediction is subjected to the effects of SPD, tempering, and surface nanocrystallization.

4.2.1 Evolution of Dislocation Density

During the metal cutting-induced deformation process, formation of a dislocation cell structure is evaluated by a set of dislocation dynamics rules including dislocation generation due to plastic deformation, dislocation annihilation by dynamic recovery, and interaction between the dislocation cell interiors and cell walls. The dislocation density evolution rate on the dislocation cell walls and cell interior are given as [36]:

$$\dot{\rho}_c = \alpha^* \frac{1}{\sqrt{3}b}\sqrt{\rho_w}\cdot\dot{\gamma}_w - \beta^* \frac{6}{bd\left(1-f\right)^{1/3}}\dot{\gamma}_c - k_o\left(\dot{\gamma}_c/\dot{\gamma}_o\right)^{-1/n}\rho_c\cdot\dot{\gamma}_c \qquad (4\text{-}1)$$

$$\dot{\rho}_w = \beta^* \frac{\sqrt{3}\left(1-f\right)}{fb}\sqrt{\rho_w}\cdot\dot{\gamma}_c + \beta^* \frac{6\left(1-f\right)^{\frac{2}{3}}}{bdf}\dot{\gamma}_c - k_o\left(\dot{\gamma}_w/\dot{\gamma}_o\right)^{-1/n}\rho_w\cdot\dot{\gamma}_w \qquad (4\text{-}2)$$

where $\dot{\rho}_c$ and $\dot{\rho}_w$ are the dislocation density evolution rate in cell interior and cell walls, respectively. Dislocation evolution rate control parameters are denoted as α^*, $\beta^*$and k_o. b is the magnitude of Burgers vector, d is the dislocation cell size. $\dot{\gamma}_w^r$ and $\dot{\gamma}_c^r$ are the resolved shear strain rates for the cell walls and interiors, respectively. It is assumed that these resolved shear strain rates are equal across the cell walls and cell interiors, i.e., $\dot{\gamma}_w^r = \dot{\gamma}_c^r = \dot{\gamma}^r$. The resolved shear strain rate $\dot{\gamma}^r$ can be calculated by the von Mises strain rate$\dot{\varepsilon}$ $\dot{\varepsilon}$ using $\dot{\gamma}^r = M_T \dot{\varepsilon}$, where M_T is the Taylor factor. $\dot{\gamma}_o$ is the reference resolved shear strain rate. The volume fraction of the dislocation cell wall are denoted as f, which is given as:

$$f = f_\infty + (f_o - f_\infty)\exp(-\gamma^r / \gamma_f) \tag{4-3}$$

where f_o and f_∞ are the initial and saturation volume fractions of cell walls, respectively. $\gamma_f$is a parameter describing the rate of variation of f with resolved shear strain $\gamma^r$and adopted to be 3.2 [33]. The total dislocation density, ρ_{tot}, is calculated from a mixture rule:

$$\rho_{tot} = f\rho_w + (1-f)\rho_c \tag{4-4}$$

and then the dislocation cell size, d_{cell}, is given as:

$$d_{cell} = K_d / \sqrt{\rho_{tot}} \tag{4-5}$$

where K_d is a material constant and adopted to be 10 in this study for steel [35].

Under the effect of severe plastic deformation, the change in microhardness is contributed by the accumulation of dislocations. This strengthening of material can be

characterized by the microhardness change (Δh_{SPD}, in GPa), which can be predicted based on the dislocation density evolution due to SPD. It is given as [40,180]:

$$\Delta h_{SPD} = k_{SPD} M_t \alpha_o G b \sqrt{\rho_{tot}} \tag{4-6}$$

where k_{SPD} is a constant slope of 1.0 [179], α_o is a constant of 0.25 [34], and G is the shear modulus. The model parameters for the unified grain refinement model are listed in Table 4.1.

Table 4.1 Unified grain refinement model parameters of hardened AISI 1060 steel.

α^*	β^*	k_o	$\dot{\gamma}_o$	f_o	f_∞	M_T	$\tilde{\gamma}^r$	G (GPa)	b (nm)	ρ_{wo} (m^{-2})	ρ_{co} (m^{-2})
0.22	0.09	14.6	1e5	0.29	0.16	3.06	2.5	80	0.248	1e12	1e11

A new kinetics of dislocation density evolution is developed to expand the above dislocation density evolution kinetics as in Eq. (4-1) to Eq. (4-6), which models the primary mechanism of SPD-induced grain refinement associated with strong DRV and DPT effects. The following sections describes the derivations of this new model based on the irreversible thermodynamic state changes in the work materials during hard drilling.

The drilling process is irreversible due to the plastic deformation and microstructure change in the work material. During a machining process, the work material is usually severely plastic deformed under high strains, strain rates, and temperatures. The plastic deformation process is subjected to rapid heating and cooling due to plastic energy dissipation, frictional work dissipation, and thermal conduction from/to adjacent material domain. In addition, the total amount of grain boundary energy

is generally drastically increased due to the large amounts of newly formed interfacial area in the thermally stable and highly misoriented UFG or nanocrystalline structure after the machining process. Hence, the thermodynamic state changes in the workpiece are non-isothermal and irreversible, i.e., entropy is produced.

The grain refinement kinetics is described by the release of stored dislocation energy to the interfacial energy change when thermally driven solid-state phase transformation occurs. The irreversible thermodynamic state changes are calculated based on the thermodynamic potential in the system, and this approach is inspired by modeling work recently published by Buchkremer and Klocke [115]. Since the plastically deformed work material is distributed below the newly generated machined surface in the workpiece or chip surface after the process, the thermodynamic system is considered as a closed system at a constant volume. Hence, Helmholtz free energy, *F*, is used to represent the irreversible thermodynamic state changes during machining. The sign of the total differential of the Helmholtz energy, d*F*, indicates whether a thermodynamic state change occurs spontaneously (d$F < 0$) or not spontaneously (d$F > 0$). The Helmholtz energy *F* is defined as:

$$F = U - TS \tag{4-7}$$

where *U* is internal energy, *T* is absolute temperature and *S* is entropy. For the following derivation of d*F* for the closed system during drilling, all extensive state variables are referred to the unit volume and are denoted with small letters. Then, the volume-specific differential of Helmholtz free energy, d*f*, is given as:

$$\mathrm{d}f = \mathrm{d}u - \mathrm{d}(s \cdot T) = \mathrm{d}u - s\mathrm{d}T - T\mathrm{d}s \tag{4-8}$$

The volume-specific differential of Helmholtz free energy should be extended for drilling to consider the grain refinement kinetics based on thermodynamic potentials. In this model, the irreversible state changes in the work material are described by an analytical formulation considering the plastic work, dissipation, thermal conduction and grain boundary energy, as well as the associated productions and flows of entropy. Then, the volume-specific change of internal energy, du, and entropy, ds, are given as:

$$\mathrm{d}u = \mathrm{d}e_{me} + \mathrm{d}e_{cond} + \mathrm{d}e_a \tag{4-9}$$

$$\mathrm{d}s = \mathrm{d}s_{diss} + \mathrm{d}s_{cond} \tag{4-10}$$

where de_{me} is the derivative of mechanical energy, de_{cond} is the derivative of thermal energy by thermal conduction, and de_a is the derivative of interface energy associated with grain size evolution, while ds_{diss} and ds_{cond} are the change of the entropy by energy dissipation and thermal conduction.

The formulation of these energy and entropy terms were derived based on the state changes from time frame t_i to t_{i+1}, which are associated with changes of equivalent plastic strain (ε_t to ε_{t+1}), equivalent strain rate ($\dot{\varepsilon}_t$ to $\dot{\varepsilon}_{t+1}$), temperature (T_t to T_{t+1}), grain size (d_t to d_{t+1}). Then, Eqs. (4-9, 10) is rewritten as:

$$\Delta u = \Delta e_{me} + \Delta e_{cond} + \Delta e_a \tag{4-11}$$

$$\Delta s = \Delta s_{diss} + \Delta s_{cond} \tag{4-12}$$

where Δe_{me} is the change of mechanical energy, Δe_{cond} is the change of thermal energy by thermal conduction, and Δe_a is the change of interface energy associated with grain size

evolution, while Δs_{diss} and Δs_{cond} are the change of the entropy by energy dissipation and thermal conduction.

Firstly, the terms in Eq. (4-11) for change of internal energy are derived. The absolute change in the volume-specific mechanical energy Δe_{me} in Eq. (4-11) is equal to the plastic work, i.e. the integral of the flow stress σ over the equivalent strain ε. Thus, Δe_{me} is associated with a change of plastic strain from ε_t to ε_{t+1}:

$$\Delta e_{me} = \int_{\varepsilon_t}^{\varepsilon_{t+1}} \sigma(\varepsilon, \dot{\varepsilon}, T) \mathrm{d}\varepsilon \tag{4-13}$$

where σ is the flow stress, which is usually formulated as a function of equivalent plastic strain (ε), equivalent strain rate ($\dot{\varepsilon}$) and temperature (T), to account for the strain hardening, strain rate hardening, and thermal softening under metal cutting conditions.

The main phase constituent of the AISI 1060 steel studied in this work was as-quenched martensite. Its flow stress during drilling is defined by Johnson-Cook (JC) model:

$$\sigma = \left(A_{JC} + B_{JC}\varepsilon^{n_{JC}}\right)\left(1 + C_{JC}\ln\left(\frac{\dot{\varepsilon}}{\dot{\varepsilon}_o}\right)\right)\left(1 - \left(\frac{T - T_{ref}}{T_m - T_{ref}}\right)^{m_{JC}}\right) \tag{4-14}$$

where A_{JC}, B_{JC}, C_{JC}, n_{JC}, and m_{JC} are model parameters, which were adapted from an oil-quenched AISI 1050 steel with a hardness of 57.8 HRC [191] listed in Table 4.2. T_m is the melting point, and T_{ref} is the reference temperature, which is room temperature of 20 °C in this work. Since the time increment is infinitesimal during the FE computation (usually 10^{-9}-10^{-8} s), it is assumed that the plastic deformation occurs at a constant temperature and strain rate from time frame t_i to t_{i+1}. Then, Eq. (4-13) is rewritten as:

$$\Delta e_{me} = \left(1 + C_{JC}\, ln\left(\frac{\bar{\dot{\varepsilon}}}{\dot{\varepsilon}_o}\right)\right)\left(1 - \left(\frac{T - T_{ref}}{T_m - T_{ref}}\right)^{m_{JC}}\right)$$

$$\cdot\left(A_{JC}(\varepsilon_{t+1} - \varepsilon_t) + \frac{B_{JC}}{n_{JC}}\left(\varepsilon_{t+1}^{n_{JC}+1} - \varepsilon_t^{n_{JC}+1}\right)\right) \qquad (4\text{-}15)$$

where $\bar{\dot{\varepsilon}}$ and $\bar{T}$ are the average values for the temperature and strain rate along the state change from time frame t_i to t_{i+1}, which are denoted as $\bar{T} = 0.5 \cdot (T_t + T_{t+1})$ and $\bar{\dot{\varepsilon}} = 0.5 \cdot (\bar{\dot{\varepsilon}}_t + \bar{\dot{\varepsilon}}_{t+1})$, respectively.

Table 4.2 Johnson-Cook model parameters of AISI 1060 steel [191].

A_{JC} (MPa)	B_{JC} (MPa)	n_{JC}	C_{JC}	m_{JC}	$\dot{\varepsilon}_o$ (1/s)	T_m (K)
2626.4	1799.3	0.245	0.0216	0.433	1	1793

It has been widely accepted that most of the mechanical energy is dissipated as heat during plastic deformation, and the fraction of the rate of plastic work dissipated as heat, β, is often assumed to be a constant parameter of 0.9 for most metals [192]. Accordingly, during each infinitesimal state change, an energy increment of $\beta\Delta e_{me}$ is added to the internal energy. Hence, in Eq. (4-11), the thermal energy increment only due to thermal conduction is equal to the total thermal energy change, Δe_{th}, minus the dissipated mechanical energy, Δe_{diss}, as:

$$\Delta e_{cond} = \Delta e_{th} - \Delta e_{diss} = c_p \rho (T_{t+1} - T_t) - \beta \Delta e_{me} \qquad (4\text{-}16)$$

where c_p is the specific heat capacity, and ρ is the density.

The change of the specific interface energy Δe_a in Eq. (4-11) is proportional to the change in volume-specific internal surface Δa as follows:

$$\Delta e_a = \Gamma_{gb} \Delta a \tag{4-17}$$

where Γ_{gb} is the grain boundary energy. Assuming cubic grains with edge length of d, i.e., grain size, Δa associated with a grain size modification from d_t to d_{t+1} is given as:

$$\Delta a = a_{t+1} - a_t = 3\left(\frac{1}{d_{t+1}} - \frac{1}{d_t}\right) \tag{4-18}$$

It was assumed that the grain boundary energy linearly decreased with temperature [193], which is given as:

$$\Gamma_{gb} = \alpha_\gamma \cdot T + \beta_\gamma \tag{4-19}$$

where α_γ and β_γ are model parameters, and the values are -4.9×10^{-10} J/mm^2/°C [193] and 4.2×10^{-10} J/mm^2 [115].

In the following, the terms involving the entropy, s, are derived. For the integral of the entropy over temperature, $s\Delta T$, the expression of $s(T)$ is determined based on the Clausius theorem as follows:

$$s(T) = \int_0^{e_{th}} \frac{\mathrm{d}e_{th}}{T} = \int_0^T \frac{c_p \rho \mathrm{d}T}{T}$$

$$= c_p \rho [T_{t+1} \ln(T_{t+1}) - T_{t+1} - T_t \ln(T_t) + T_t] \tag{4-20}$$

To determine the entropy increments Δs_{diss} and Δs_{cond} are determined, an analytical analysis is conducted to determine the change of temperature due to heat dissipation of plastic work, ΔT_{diss}, and thermal conduction only, ΔT_{cond}, from time frame t_i to t_{i+1}.

Like the total thermal energy change, the temperature change is mainly determined by the heat dissipation of plastic work and thermal conduction. Hence, the temperature increment, dT, can be equivalently divided into the temperature increment due to heat dissipation of plastic work, dT_{diss}, and thermal conduction only, dT_{cond}, as:

$$\mathrm{d}T = \mathrm{d}T_{diss} + \mathrm{d}T_{cond} \tag{4-21}$$

where $\mathrm{d}T_{diss} = \frac{\mathrm{d}\varepsilon_{diss}}{c_p \rho}$. Hence, from time frame t_i to t_{i+1}, the change of temperature can be rewritten in:

$$\Delta T = T_{t+1} - T_t = \Delta T_{diss} + \Delta T_{cond} \tag{4-22}$$

where $\Delta T_{diss} = \frac{\Delta \varepsilon_{diss}}{c_p \rho} = \frac{\beta \Delta \varepsilon_{me}}{c_p \rho}$. Then, ΔT_{diss} is equal to:

$$\Delta T_{cond} = \Delta T - \Delta T_{diss} = T_{t+1} - T_t - \frac{\beta \Delta \varepsilon_{me}}{c_p \rho} \tag{4-23}$$

Based on Clausius theorem, ds_{diss} is associated with the dissipated mechanical energy, de_{diss}, and is given as:

$$\mathrm{d}s_{diss} = \frac{\mathrm{d}e_{diss}}{T} \tag{4-24}$$

where $\mathrm{d}e_{diss} = c_p \rho \mathrm{d}T_{diss}$. Then, Δs_{diss} is given as:

$$\Delta s_{diss} = \int_{e_{diss_t}}^{e_{diss_{t+1}}} \frac{\mathrm{d}e_{diss}}{T} = \int_{T_t}^{T_{diss_{t+1}}} \frac{c_p \rho}{T} \mathrm{d}T$$

$$= c_p \rho \ln\left(\frac{T_{diss_{t+1}}}{T_t}\right) = c_p \rho \ln\left(\frac{T_t + \Delta T_{diss}}{T_t}\right) \tag{4-25}$$

Likewise, Δs_{cond} is given as:

$$\Delta s_{cond} = \int_{e_{cond_t}}^{e_{cond_{t+1}}} \frac{\mathrm{d}e_{cond}}{T} = \int_{T_t}^{T_{cond_{t+1}}} \frac{c_p \rho}{T} \mathrm{d}T$$

$$= c_p \rho \ln\left(\frac{T_{cond_{t+1}}}{T_t}\right) = c_p \rho \ln\left(\frac{T_t + \Delta T_{cond}}{T_t}\right) \quad (4\text{-}26)$$

Hereinabove, the volume-specific differential of Helmholtz free energy, d*f*, has been formulated from time frame t_i to t_{i+1} to capture the irreversible thermodynamic state changes during the drilling process. The considered thermodynamic state changes are calculated by the spatially resolved evolution of strain, strain rate, temperature, flow stress obtained from FE simulation.

When d*f* is negative and the work material temperature exceeds austenite temperature (AC3), the stored dislocation energy is transformed to the interface energy during the grain refinement in the WEL. The change of the interface energy is given as:

$$\Delta e_a = \varphi E_{st} \quad (4\text{-}27)$$

$$E_{st} = \int (1 - \beta)\, \mathrm{d}e_{me} \quad (4\text{-}28)$$

$$E_{res} = (1 - \varphi) E_{st} \quad (4\text{-}29)$$

where E_{st} is the stored dislocation energy, E_{res} is the residual stored dislocation energy, and φ is the fraction of the released dislocation energy. It was assumed that this fraction is mainly associated with temperature: φ is the maximum of 1 when the temperature is equal to the melting point; φ is the minimum of 0 when the temperature is the austenite temperature AC_3. The austenite temperature was determined as 790 °C for AISI 1060

steel from the classic Fe-C binary phase diagram [194]. To simplify the model, φ is assumed to be proportional to the temperature and given as:

$$\varphi = 2.457\frac{T}{T_m} - 1.457 \qquad \text{for } AC_3 < T < T_m \tag{4-30}$$

where all the temperatures were in Kelvin.

From time frame t_i to t_{i+1}, the refined grain size in WEL, d_{t+1}, can be determined by the transformation of the stored dislocation energy. Hence, d_{t+1} is given as:

$$d_{t+1} = \frac{3\Gamma_{gb}}{\frac{3\Gamma_{gb}}{d_t} + \Delta e_a} = \frac{3\Gamma_{gb}}{\frac{3\Gamma_{gb}}{d_t} + \varphi\int(1-\beta)\mathrm{d}e_{me}} \tag{4-31}$$

Due to the reduction in the stored dislocation energy, the equivalent plastic strain and dislocation density should be decreased accordingly. At time frame t_{i+1}, the stored dislocation energy E_{st} is associated with the equivalent plastic strain ε_{i+1} before the transformation, whereas residual dislocation energy E_{res} is associated with the adjusted equivalent plastic strain ε_{adj} after the transformation. From Eqs. (4-17, 27, 28, 29, 30), ε_{adj} is given as:

$$\varepsilon_{adj} = -\frac{p_1}{2} + \sqrt{\left(\frac{p_1}{2}\right)^2 - p_2} \tag{4-32}$$

$$p_1 = \frac{A_{JC}(n_{JC}+1)}{B_{JC}}, \qquad p_2 = -\frac{(n_{JC}+1)(1-\varphi)E_{st}}{\left[1+C_{JC}\ln\left(\frac{\bar{\dot{\varepsilon}}}{\bar{\dot{\varepsilon}}_o}\right)\right]\left[1-\left(\frac{T-T_{ref}}{T_m-T_{ref}}\right)^m\right]B_{JC}}$$

Then, the dislocation density is adjusted regarding to the change of the plastic strain. In this work, the adjusted total dislocation density, ρ_{adj}, is assumed to be proportional to change of the plastic strain, which is given as:

$$\rho_{adj} = \left(1 - \frac{\varepsilon_{t+1} - \varepsilon_{adj}}{\varepsilon_{t+1}}\right)\rho_{tot} \quad (4\text{-}33)$$

The final hardness in the WEL can be predicted by Hall-Petch equation [157]:

$$H = H_o + k_{HP} d^{-\frac{1}{2}} \quad (4\text{-}34)$$

where H is the microhardness of the material, H_o is the original microhardness of the matrix material (as-quenched martensite, 7.88 GPa), d is the grain size in μm, and k_{HP} is a material constant of 0.588 fitted from the drilling experimental results reported by Todaka et al. [85].

4.2.2 Dynamic Phase Transformation

To account for the evolution of phase composition of the work material, phase transformation kinetics is solved simultaneously in this work with the energy equation at each time step during simulations. The initial work material was defined as a homogeneous as-quenched martensitic (*M*) structure. The heating rates were estimated as high as ~10^6 K/s in the top surface layer during the hard machining process [77], which prevent martensite from decomposing within the short period of heating cycle illustrated by Ding and Shin [38]. Diffusionless reverse martensitic transformation was assumed to occur in the top surface layer if the local workpiece temperature during cutting rises above the austenite temperature, and the initial as-quenched martensite transforms to austenite. The austenite temperature was determined as 790 °C for AISI 1060 steel from the classic Fe-C binary phase diagram [194]. During the heating cycle in hard drilling, no carbide dissolution needs to be modeled since the initial as-quenched martensite structure is quite homogeneous with a high carbon concentration.

As the material temperature begins to drop in the top surface layer, austenite transforms to martensite if the cooling rate is fast enough or to bainite if the cooling rate is slower. To determine if bainite formation will occur, the current cooling time of a material undergoing non-isothermal transformation is compared with the amount of time required to begin bainite formation in an isothermal process. Sheil's Additivity Rule was used to discretize the process over a number of time steps, allowing for non-isothermal calculations [10]. If the integral in Eq. (4-35) reaches a value of 1 before the temperature drops below the martensite formation temperature (M_s), bainite will begin to form given in [195].

$$\int_0^t \frac{dt}{t_a(T)} \geq 1 \tag{4-35}$$

where dt is the length of a time-step, $t_a(T)$, is the incubation time required for bainite to form isothermally at temperature T, and t is the current cooling time of an austenite cell in the model. Under the drilling parameters in this study, bainite is not formed because the cooling rate is sufficiently fast, thereby avoiding formation of bainite. Once the temperature has dropped below M_s, the following equation is used to calculate the volume fraction of martensite in the cooling process given in [196]:

$$f_m = f_\gamma^* \left(1 - e^{-0.011(M_s - T)}\right) \tag{4-36}$$

Here f_γ^* is the volume fraction of austenite at the time when temperature reaches M_S. If the cooling rate is sufficiently fast, i.e., no bainite is formed, all austenite that does not change into martensite will be considered as retained austenite. M_S was estimated to be 270 °C in this study obtained in [194]. The change of microhardness due to the dynamic

phase transformation (Δh_{DPT} in GPa) can be calculated according to the phase fractions of that element given in [10]:

$$\Delta h_{DPT} = \sum_{i=1}^{v} f_i h_i - h_o \tag{4-37}$$

where f_i is the fraction of phase i in the element, h_o is the initial bulk microhardness, h_i is the hardness of phase i, and v represents the number of present phases in the element.

The material below the top surface layer is subjected to tempering for the peak temperature between 250 °C and the lower critical temperature of 727 °C given in [195]. In this region, martensite can further decompose to ferrite and cementite during the tempering process. The higher the workpiece temperature (still below 727 °C), the more of original martensitic structure will revert to a ferrite-cementite mixture and consequently strength and hardness will fall progressively, while the toughness and ductility increase. The change of hardness due to tempering (Δh_{Temper} in GPa) depends on the heating history and can be estimated by

$$\Delta h_{Temper} = -3.097 \times 10^{-6} T_P^{\,2} - 2.248 \times 10^{-3} T_P + 0.17 \tag{4-38}$$

where Tp is the peak temperature in the tempered layer. Microhardness of the martensite and retained austenite were adopted as 64 HRC (≈7.946 GPa) and 17 HRC (≈2.256 GPa) [106], respectively.

During the phase transformation in the drilling process, an additional strain is induced by the microstructure evolution along with mechanical and thermal strains. The phase transformation also produces transformation-induced plasticity. This can be

represented analytically by adding a separate strain component to the total strain function. Hence, the total strain increment ($\Delta\varepsilon$) for a steel undergoing the solid-state phase transformation can be written as the sum of individual components of the strain as follows given in [196].

$$\Delta\varepsilon = \Delta\varepsilon^{E} + \Delta\varepsilon^{P} + \Delta\varepsilon^{T} + \Delta\varepsilon^{\Delta V} + \Delta\varepsilon^{TrP} \tag{4-39}$$

where $\Delta\varepsilon^{E}$, $\Delta\varepsilon^{P}$, $\Delta\varepsilon^{T}$, $\Delta\varepsilon^{\Delta V}$, and $\Delta\varepsilon^{TrP}$ represent the strain increments due to elastic, plastic, thermal, volumetric dilatation and transformation-induced plasticity, respectively. The elastic strain increment $\Delta\varepsilon^{E}$ is calculated using the isotropic Hook's law. The rate-independent constitutive models given in the following are used for the plastic strain increment of $\Delta\varepsilon^{P}$. The thermal strain increment $\Delta\varepsilon^{T}$ is computed using the coefficient of thermal expansion. When a given volume in a workpiece undergoes the transformation from one phase to another, the microstructural pattern transforms. For example, the austenite changing to martensite will transform from a face-centered cubic structure to a body-centered tetragonal structure, thereby dilating the volume. The strain increment due to this volumetric dilatation is given in [197]

$$\Delta\varepsilon^{\Delta V} = \frac{1}{3}\frac{\Delta V}{V}\Delta f \tag{4-40}$$

where the percent volume change $\Delta V/V$ due to phase transformation from one phase to another and Δf is the change in phase fraction during the time increment. The percent volume change from the austenite to martensite ($\Delta V/V_{\gamma\text{-}M}$,) was determined to be 1.026% [10]. The formation of martensite induces the transformation plasticity, which is also produced when dilatational strains interact with the already-existing stress field [196]. It

has been reported that transformation plasticity produces a mechanical effect on the stresses and strains equivalent to that induced when the yield stress of the steel is reduced by a certain extent over the phase transformation temperature range given in [198]. A reduction of 30 MPa in flow stress can represent the mechanical effect of transformation plasticity via the formation of martensite [196]. This simplified approach was employed in this work to incorporate the transformation plasticity into the FE model.

4.3 Multi-step Finite Element Modeling of Drilling Process

The metallo-thermo-mechanically coupled material model was implemented in an FE simulation to simulate the formation of a WEL and nanocrystallization during hard drilling. The microstructural analysis conducted in this work was based on a previously published experimental study by Li et al. [86]. The drilling experiment used the hardened AISI 1060 steel (Fe-0.56wt.%C) as the work material, during which cutting speed of 60-100 m/min and feed of 0.01-0.10 mm/rev were applied. The process conditions are listed in Table 4.3.

Table 4.3 Experimental conditions for drilling of AISI 1060 steel [86].

Test	1	2	3	4	5
V (m/min)	80	60	100	80	80
f (mm/rev)	0.05	0.05	0.05	0.01	0.1

It is well-known that the drilling process is too difficult and expensive to be directly simulated with the current numerical solutions. Numerous efforts have been

carried on to explore different schemes to predict the thermal and mechanical response during the drilling process [199–201]. In these schemes, the heat source was modeled by integrating the heat flux on a series of small partitions along the cutting lip of the drill bit. Nowadays, it has been widely accepted the cutting action along the cutting lips of a drill bit can be interpreted as occurring within a series of oblique sections, in which the rake and inclination angles vary radially along each lip [202]. However, these aforementioned models are not fully thermomechanically coupled, and did not consider the mechanism of grain refinement in the formation of white layer, although ultrafine grain structures have been widely observed in the near-machined surface layers.

With the development of numerical modeling, a 3D thermomechanically coupled FE model for drilling processes is available with some commercial FE simulation software packages, e.g., AdvantEdge^{TM}. However, due to issues of computational cost and some unavailable required features for a 3D drilling simulation, a multi-step FE modeling approach is developed in this work to simulate the surface and subsurface microstructural change during the hard drilling process using commercial FE simulation software of AdvantEdge^{TM} 6.4 and ABAQUS 6.12.

In the 3D drilling FE simulation, the steady-state solutions in the workpiece domain were simulated; these included torque, thrust force, stress, strain, and temperatures in the tool or chip. Then, the temperature and stress fields were extracted from the uncut workpiece domain ahead of the cutting edge and were imported to the subsequent 2D FE analysis using ABAQUS. In this step, the thermally driven phase transformation and grain refinement were not modeled due to the coarse mesh on the drilled surface. These phenomena were simulated in the subsequent 2D FE orthogonal

cutting simulation using ABAQUS with a very fine mesh in the deformation zone and on the machined surface.

In the 3D drilling simulation using AdvantEdge™, the microstructure of the work materials was assumed to be as-quenched martensite. The JC model of as-quenched martensite was converted to three equations of strain hardening, rate sensitivity, and thermal softening with the power law in order to simulate the material flow stress. The carbide tool material was selected from the tool material library of AdvantEdge™. To obtain the steady-state solutions effectively, the 3D drilling simulations were started with an initial axial depth of 4 mm and continued for 1000° of tool rotation, i.e., 2.78 revolutions. A typical procedure to export the steady-state solution from AdvantEdge™ is shown in Figure 4.6. After the 1000° of tool rotation, the stable chip temperature distribution, as shown in Figure 4.6a, and the stable histories of torque and thrust force, as shown in Figure 4.6b, indicated that the steady state of the drilling process had been reached. Then, at the final frame of the 3D drilling simulation, the simulation domain was cross-sectioned at the end of cutting lip on a horizontal plane A-A, as shown in Figure 4.6c. A typical steady-state temperature distribution on the section plane A-A is shown in Figure 4.6d, and the temperature distribution near the deformation zone is shown in Figure 4.6e. The temperature and stress fields were extracted in the uncut workpiece domain ahead of the cutting edge, as labeled in Figure 4.6e, and the uncut chip thickness was estimated as 0.1 mm for the reduced 2D orthogonal cutting simulation.

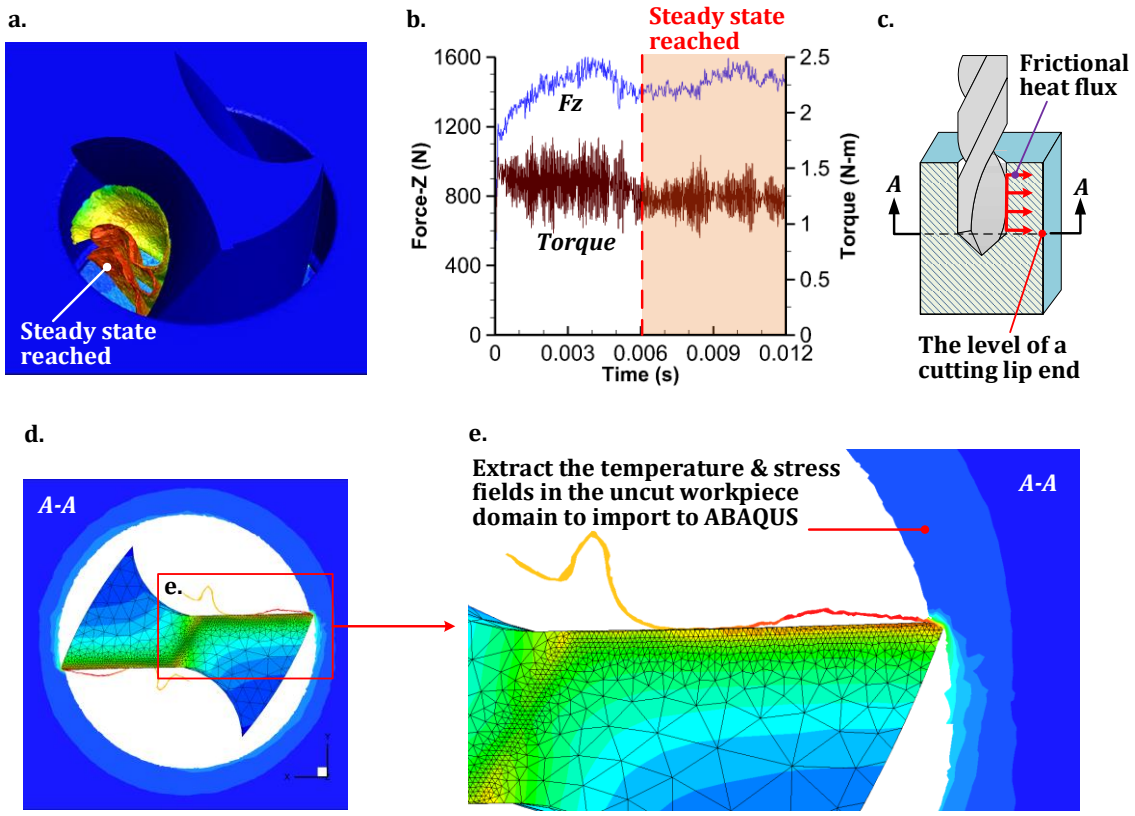

Figure 4.6 3D FE drilling simulation with AdvantEdge™: (a) 3D steady state temperature distribution; (b) histories of torque and thrust force; (c) the level of the cross section of 3D simulation domain; (d) a typical steady-state temperature distribution on the section plane A-A; e) a zoom-in temperature distribution near the deformation zone.

In ABAQUS, the coupled Eulerian-Langrangian (CEL) model was set up as shown in Figure 4.7. The arbitrary-Lagrangian–Eulerian (ALE) technique was used in the whole workpiece domain. During simulation, material flows into the workpiece mesh from the left inlet surface, passes the region around the tool tip, and exits the simulation domain from the right outlet surface and the very top surface of the workpiece domain representing the chip. The ALE adaptive mesh velocity constraints were applied to confine the spatial motion of the mesh. The steady-state temperature and stress fields

were imported from the previous 3D simulation and were defined as Eulerian boundary conditions in the material flow inlet. A uniform distributed frictional heat flux was applied on the machined surface to simulate the accumulated heat effect of rubbing between drill bit flutes and the machined surface. The element size near the machined surface was set to 2 μm along the Y-direction. The applied frictional coefficient at the tool-chip interface was 0.4. A long length of 5 mm cut was simulated to ensure that the steady states were reached for the chip morphology, mechanical, thermal, and metallurgical field solutions. Other physical properties of AISI 1060 steel used in the simulations are listed in Table 4.4.

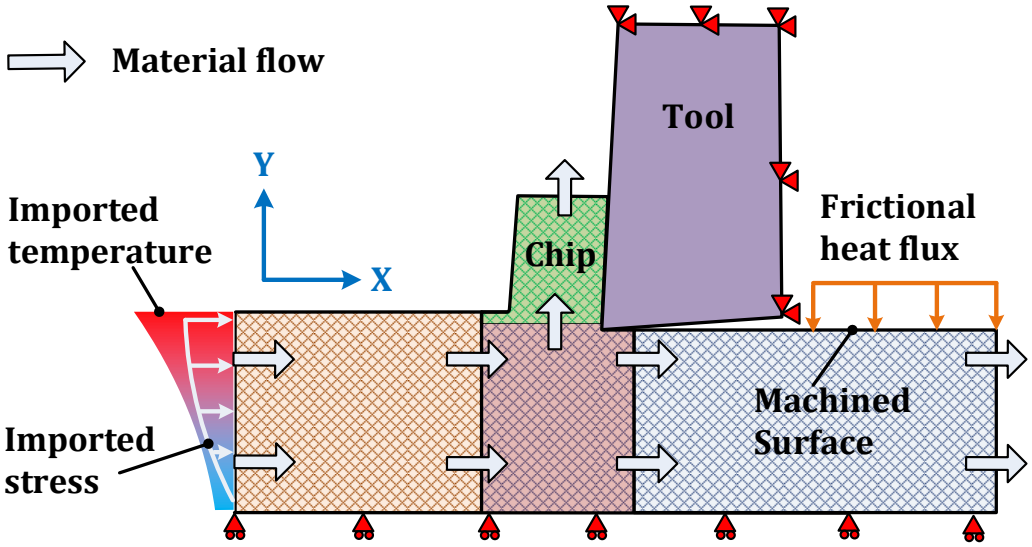

Figure 4.7 ABAQUS model configuration for the 2D CEL orthogonal cutting simulation.

Table 4.4 Physical properties of AISI 1060 steel [203].

Property	***Data***
Elastic modulus, E (GPa)	200
Density, ρ (kg/m^3)	7870
Magnitude of Burger's Vector (nm)	0.248
Poisson ratio, ν	0.29
Thermal expansion, α (μm/m·°C)	11
Thermal conductivity, k (W/m·K)	51.9
Specific heat, C_p (J/kg·K)	472

A user-defined material subroutine of VUHARD was developed for AISI 1060 steel in FORTRAN as required by ABAQUS. During the simulation, material subroutines were called at each node within the workpiece domain to update the state variables and user-defined metallurgical variables. The MTM coupled grain refinement model was implemented to simulate the formation of the WEL and the grain refinement in the WEL based on the evolution of dislocation density, phase constituents, and the irreversible thermodynamic state changes.

4.4 Simulation Results and Discussions

Simulation results of Test-1 are presented in this section to show the model's capability and the validation of the second-step 2D CEL orthogonal cutting simulation using ABAQUS. Figure 4.8 shows the simulated steady-state distribution of temperature, equivalent plastic strain, dislocation density, and grain size. As shown in Figure 4.8a, the peak temperature was predicted to be about 921 °C at the tool-chip interface. The peak

temperature on the machined surface is near the deformation zone, which was about 868 °C and higher than AC3. As shown in Figure 4.8b, large plastic strains were mainly distributed in the chip and surface layers of the machined surface. From the zoom-in view, very large strain gradients can be observed near the machined surface. As shown in Figure 4.8c, dislocations accumulated with the plastic deformation through the primary deformation zone into the chip or machined surface. However, the distribution of dislocation density did not follow the same trend as the distribution of plastic strain, which usually can be observed for an SPD process under cold working conditions. In the chip, the peak dislocation density did not occur in the secondary deformation zone along the chip-tool interface or the machined surface, where the material usually undergoes much more SPD. Instead, peak dislocation density was obtained in the domain near the free surface of the chip, which is a less deformed domain than the secondary deformation zone or the machined surface. The dislocation density distribution in the machined surface can be seen in the zoom-in view shown in Figure 4.8c. A higher dislocation layer was obtained below the topmost surface layer in the machined surface, which was also a different distribution from the gradient of plastic strain, as shown in Figure 4.8b. Even with a lower dislocation density, the simulated minimum grain size was about 10 nm in the secondary deformation zone along the chip-tool interface, as shown in Figure 4.8d. As shown in the zoom-in view, the simulated minimum grain size was about 39 nm in the topmost surface layer with a relatively lower dislocation density.

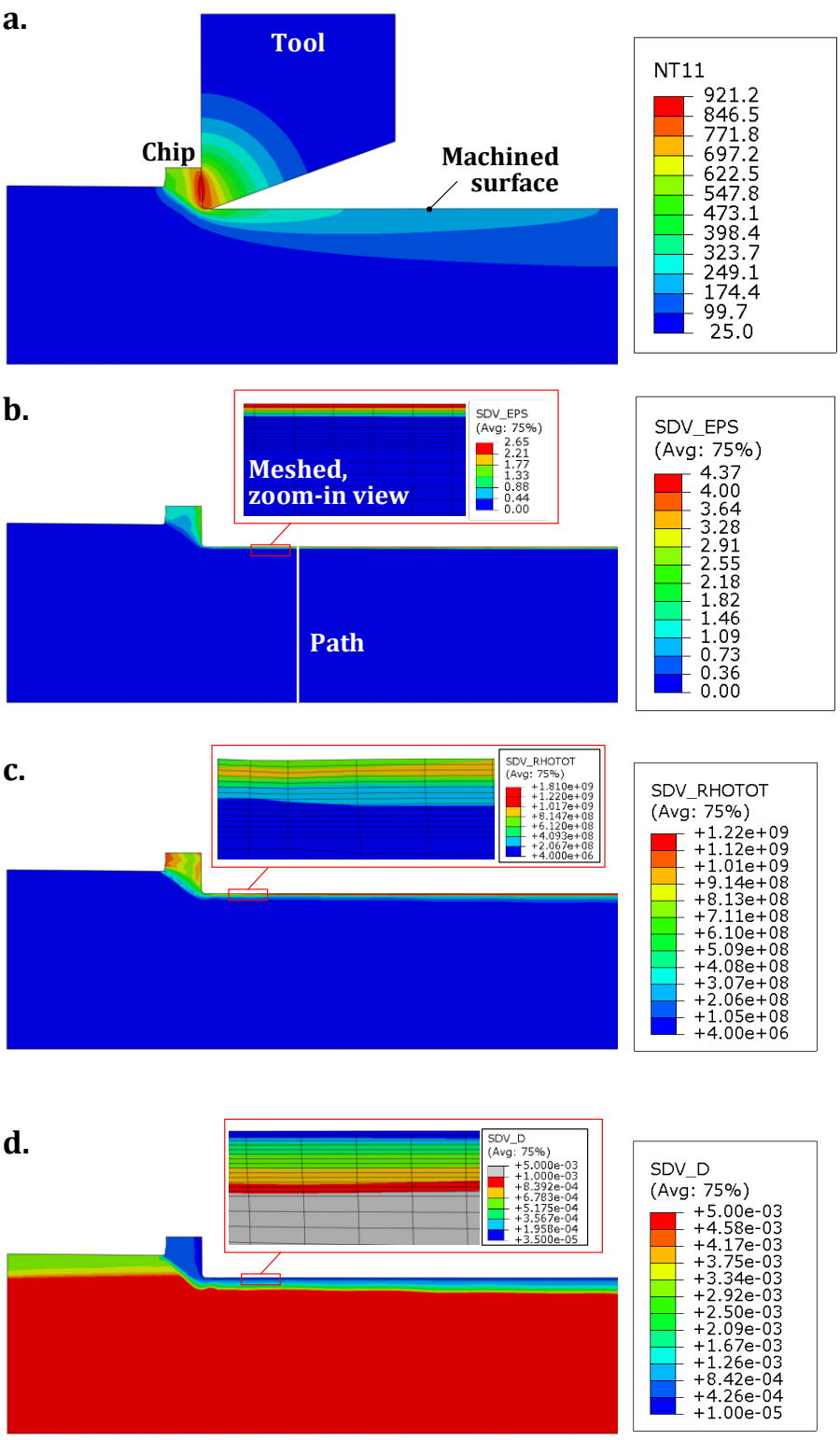

Figure 4.8 Test-1 simulation results: (a) temperature, (b) equivalent plastic strain, (c) dislocation density, and (d) grain size.

A quantitative assessment of the simulation results was performed on the plastic strain, total dislocation density, and grain size along a vertical path defined in ABAQUS, as shown in Figure 4.8b. Figure 4.9a shows the simulated depth profiles of shear strain, total dislocation density, and grain size. The FE simulation results showed high shear strains of 7.86-0.9 within the topmost layer of 10 μm in the machined surface, whereas the shear strain gradually decreased to 0.18 at the depth around 20 μm. With the increase of shear strain from the depth around 20 μm to the machined surface, the simulated dislocation density increased from 2.13×10^{14} m^{-2} to its peak value of 9.1×10^{14} m^{-2} at the depth around 5 μm, then gradually decreased to 6.6×10^{14} m^{-2} on the machined surface. The inflection point occurred at the depth around 5 μm was the result of the significant annihilation of dislocations due to dynamic recovery and DPT within this domain. The nanocrystalline grain size of 39 nm was predicted on the machined surface. The grain size increased to 240 nm at the depth around 5 μm, where the inflection point of the dislocation density was predicted. Then, the grain size gradually increased to the level of 1 μm at the depth around 33 μm.

The FE simulation results were validated by comparing the depth profiles shown in Figure 4.9a with the hole surface microstructure shown in the SEM and TEM micrographs in Figure 4.9b-c, which were obtained from a cross section perpendicular to the hole axis. As shown in Figure 4.9b, a sharp boundary between the WEL and the microstructure beneath it was found at the depth around 10 μm, corresponding to the start of the drastic increase of shear strain as shown in Figure 4.9a. Figure 4.9c shows the TEM micrographs at two locations in the WEL. These two locations corresponded to the nanocrystalline layer and the UFG layer in the WEL, which were labeled by “A” and

"B," respectively, in Figure 4.9b. As shown in the TEM micrographs, the dislocation density in Location A was obviously lower than that in Location B. This FE simulation consistently captured the inflection point occurring at the depth around 5 μm, as shown in Figure 4.9a, even though the shear strain in Location A was much higher than that in Location B. The predicted grain sizes at the depths similar to Locations A and B were close to the TEM observations, as shown in Figure 4.9c. Also, the predicted nanocrystalline layer thickness was about 2.5 μm, which was very close to the nanocrystalline layer thickness of 2.77 μm reported by Li et al. [86]. Hence, this newly developed MTM coupled grain refinement model successfully captured the formation of nanocrystalline and UFG structures in the WEL during drilling of hardened steels due to the combined effects of dynamic recovery in SPD and DPT.

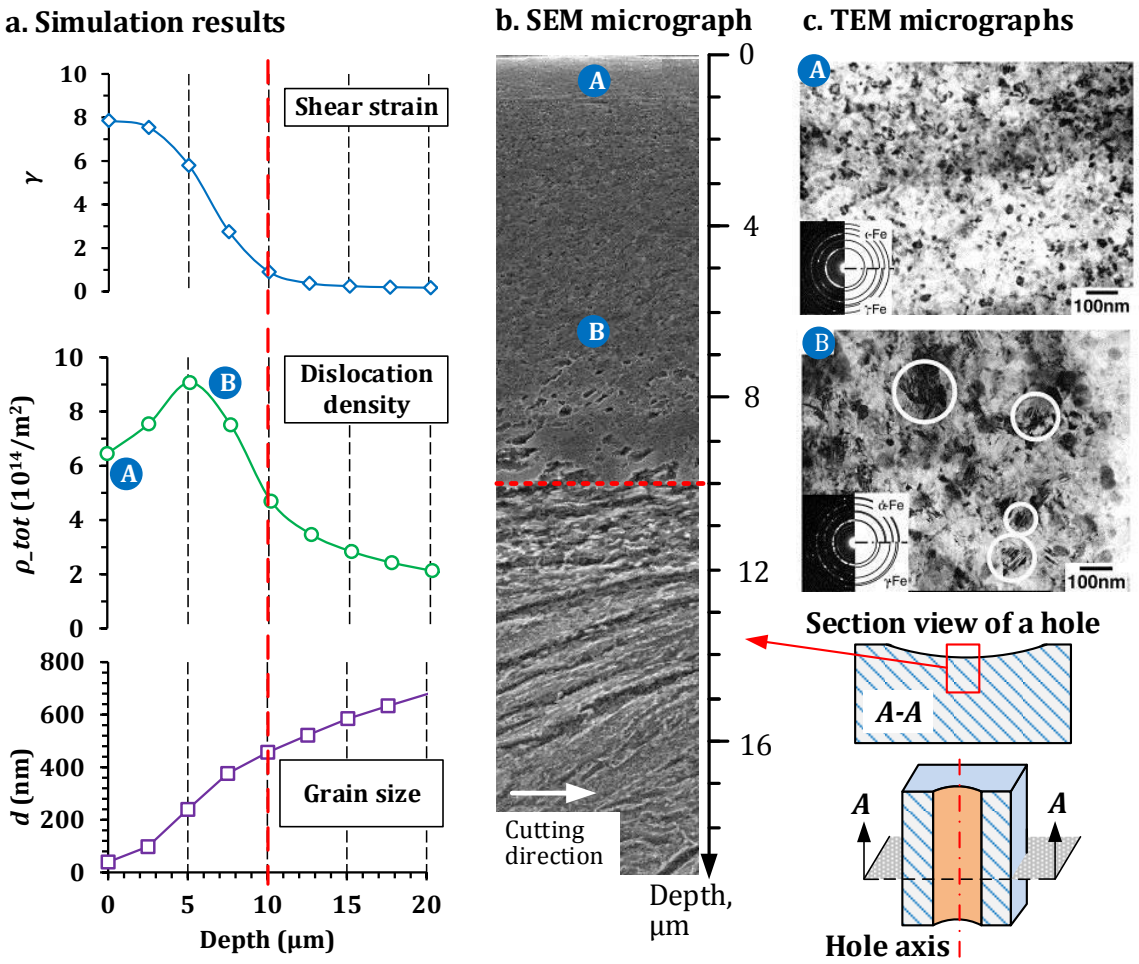

Figure 4.9 The comparison of (a) simulated profiles of shear strain, total dislocation density, grain size along the penetration with the (b) SEM and (c) TEM micrograph near surface of a hole in Test-1 (original micrographs adapted from Li et al. [86]).

The microhardness below the drilled hole surface was also predicted using the MTM coupled grain refinement model. Figure 4.10a shows the microhardness measurement below the drilled hole surface. A peak microhardness value of 10.8 GPa was simulated on the hole surface, then it gradually decreased to 8.9 GPa at the depth around 10 μm. This peak microhardness layer corresponded to the WEL, as shown in Figure 4.10b. Below the WEL, the microhardness drastically decreased to about 5.4 GPa

at the depth around 15 μm, and it gradually increased to the original hardness of the matrix material of as-quenched martensite at the depth around 64 μm. This softened layer with 15-64 μm corresponded to the tempered martensite layer as shown in Figure 4.10b. The simulated depth profile of microhardness agreed very well with the microhardness measurement reported by Todaka et al. [85]. As shown in Figure 4.10c, the microhardness increased to as high as 11.3 GPa in the WEL. Then, it dropped to 5-6 GPa within the 15-25 μm below the surface, which was even lower than that of the as-quenched martensitic matrix material. With the increase in the depth, the hardness was restored to that of the matrix material.

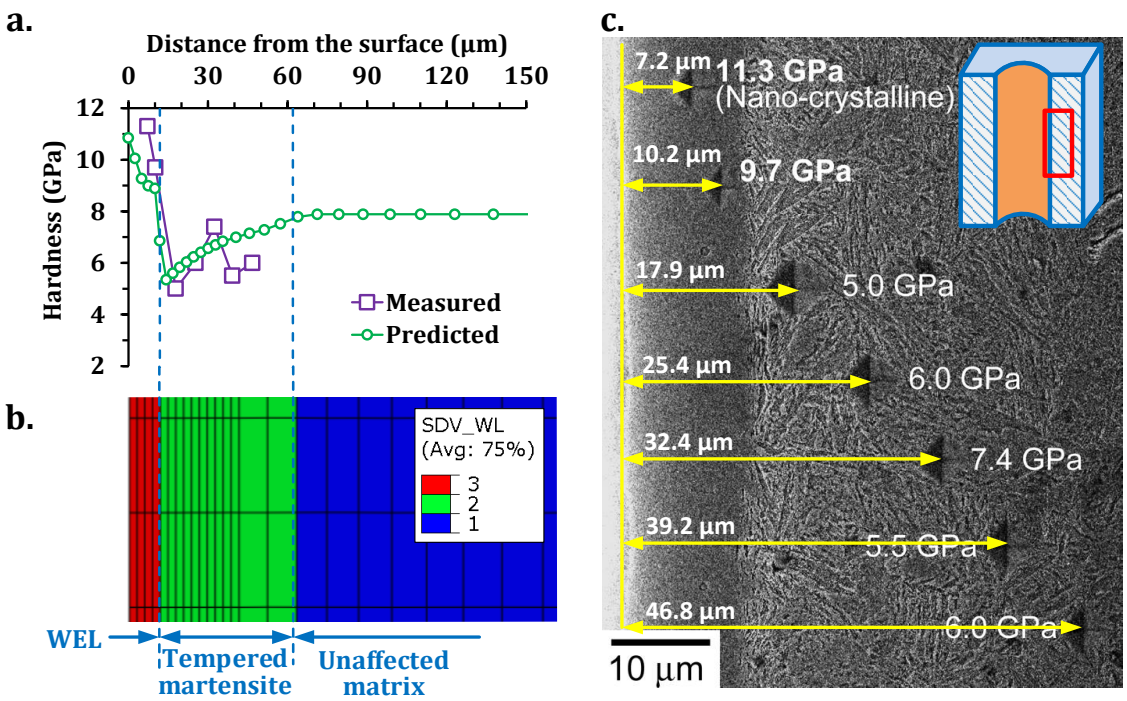

Figure 4.10 Predicted microhardness profile and transformed phases near the hole surface for Test-1: (a) the predicted microhardness profile; (b) the predicted phase distribution; (c) experimental measurement of microhardness (original images adapted from Todaka et al. [85]).

Figure 4.11 shows a series of exemplary visualizations to illustrate the grain refinement kinetics to form the nanocrystalline and UFG structures in the WEL based on the thermodynamic irreversibility. The distribution of Helmholtz free energy (*df*) near the deformation zone is shown in Figure 4.11a. The minimum of Helmholtz free energy was obtained in the primary deformation zone, and the maximum was observed on the machined surface below the tool tip. Figure 4.11b-c showed the distributions of two entropy terms $s \cdot dT$ and $T \cdot ds$, which is the formulation to calculate *df*. The distributions of both entropy terms showed maximums in the primary deformation zone. Hence, the most entropy was generated in the primary deformation zone, where the irreversible processes occurred, including plastic deformation, grain refinement and dynamic phase transformation. In addition, the minimums of both entropy terms were located on the machined surface, which was the same position as that of the maximum of *df*. Compared with the temperature distribution as shown in Figure 4.11d, it can be observed that the particular location on the machined surface corresponded to the location on the machined surface subjected to a drastic temperature drop due to the end of the frictional contact with the cutting tool. This finding indicated that the heat dissipation and material thermal loadings had a significant impact on the Helmholtz free energy.

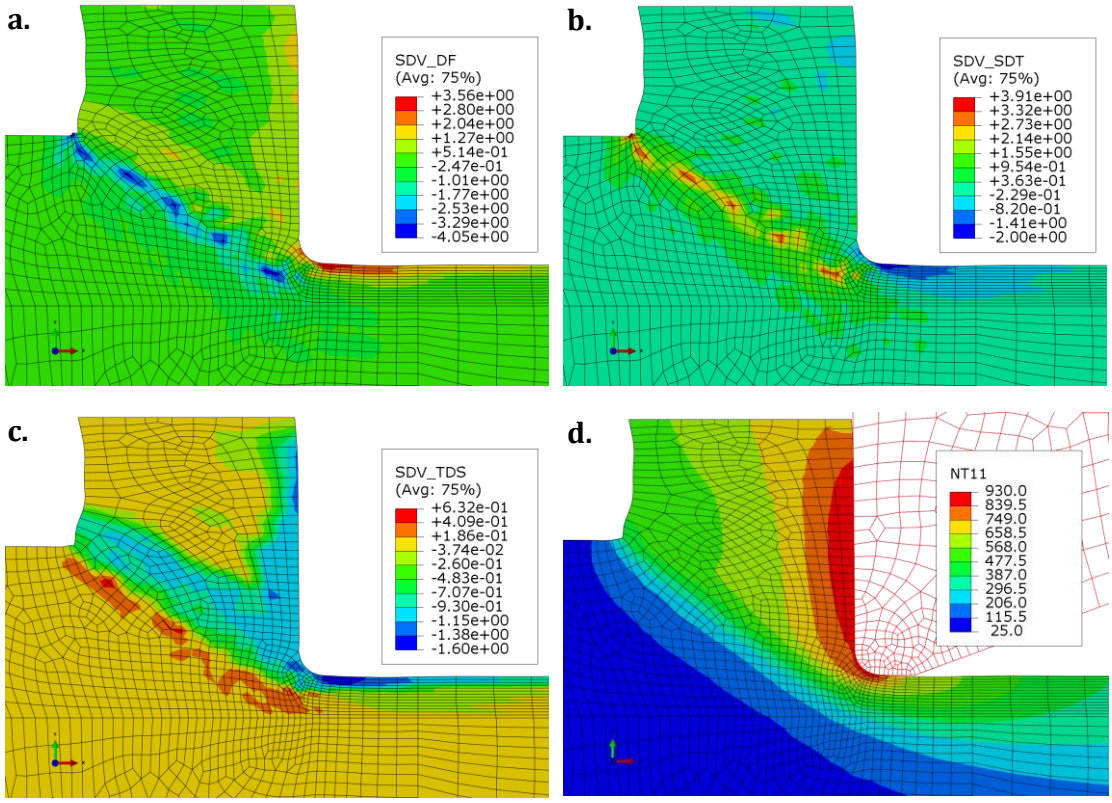

Figure 4.11 Typical FE simulated distributions near the primary deformation zone: (a) Helmholtz free energy; (b) the entropy term of s·dT; (c) the entropy term of T·ds; (d) temperature.

The influence of the cutting speed and feed on the thickness of the white layer of a drilled hole was studied. Figure 4.12a shows the effect of cutting speed on the nanocrystalline white layer thickness for cutting speeds of 60, 80, and 100 m/min and a constant feed of 0.05 mm/rev. A higher cutting speed can form thicker nanocrystalline white layers due to more severe heat generation. The thickness of the nanocrystalline white layer increased from 8 to 15 μm by 87.5% as the speed increased from 60 to 100 m/min, corresponding to the simulated peak surface temperature increase from 950 to 1,107 °C. Figure 4.12b shows the comparison of feed effect on the nanocrystalline white

layer thickness. The feed varied from 0.01 to 0.10 mm/rev with a constant cutting speed of 80 m/min. Greater feeds can form thicker nanocrystalline white layers in the tests. The thickness of the nanocrystalline white layer increased from 7.5 to 13 μm by 73.3% due to the greater heat generation as the feed increased from 0.01 to 0.1 mm/rev.

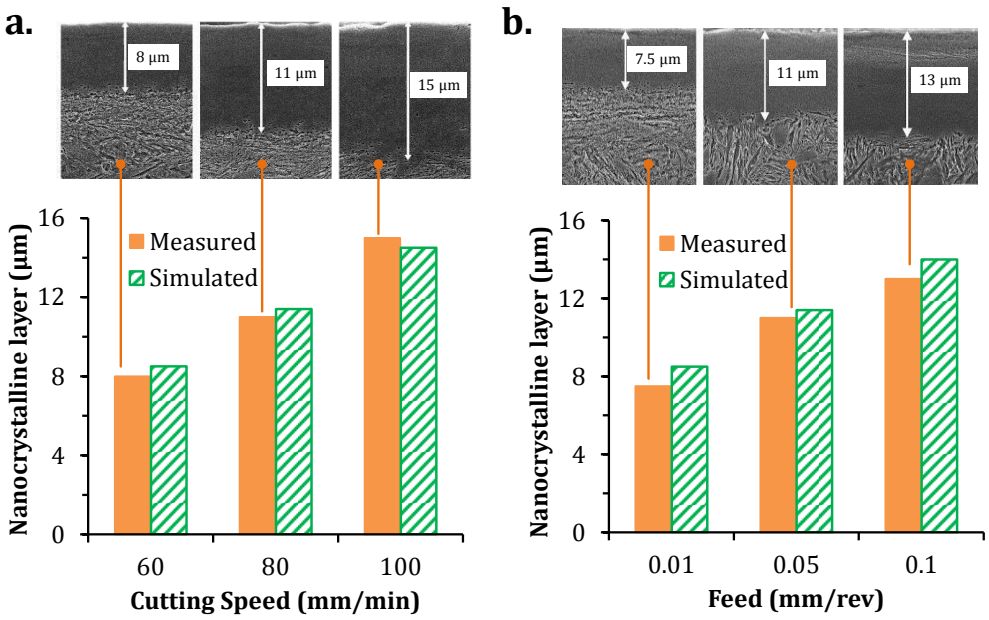

Figure 4.12 Effects of drilling parameters: (a) cutting speed and (b) feed.

4.5 Summary

A thorough analysis was conducted on hardened steel surface nanocrystallization during machining and other SPD processes under various strain rates and process durations. The SPD-induced grain refinement associated with strong dynamic recovery and thermally driven phase transformation effects should be the primary mechanism for the formation of UFG and nanocrystalline structures in the WEL during the machining of

hardened steels. Dynamic recrystallization, especially for the conventional discontinuous dynamic recrystallization induced by thermal diffusion, should not be the mechanism for grain refinement in a UFG or even nanocrystalline structure in the WEL.

A metallo-thermo-mechanically coupled grain refinement model was developed to predict the surface nanocrystallization and WEL formation during the machining of hardened steels associated with evolution of dislocation density and thermally driven phase transformation. In this model, a new kinetics was developed to capture the formation of a nanocrystalline structure in the WEL based on the thermodynamic irreversibility in the work material during the machining process. This metallo-thermo-mechanically coupled grain refinement model was implemented in an FE analysis of a drilling process of hardened AISI 1060 steel. An efficient multi-step FE model was developed for the drilling process, including a 3D drilling simulation using AdvantEdge™ and a 2D CEL orthogonal cutting simulation using ABAQUS. This model successfully captured the WEL formation and surface nanocrystallization during the drilling process of hardened AISI 1060 steel. The analysis based on the thermodynamic irreversibility may establish a new theoretical approach to evaluate the physics of surface nanocrystallization during the machining of hardened steels.

CHAPTER 5.

DISCONTINUOUS DYNAMIC RECRYSTALLIZTION SIMULATION USING CELLULAR AUTOMATON

As concluded in Chapter 4, dynamic recrystallization does not contribute to machined surface nanocrystallization or white etching layer formation during hard machining of steels. However, for bulk work materials subjected to severe plastic deformation at elevated temperatures, extensive experimental observations have provided direct evidence to support discontinuous dynamic recrystallization as the major microstructure evolution mechanism.

In this chapter, a new dislocation density-based cellular automaton model is developed for the first time to simulate microstructure evolution of bulk materials during dDRX-dominated SPD processes. Multiple microstructure evolution mechanisms, including severe plastic deformation, dynamic recovery, discontinuous dynamic recrystallization, and thermally driven grain growth, were coupled in the CA model.

Two SPD processes were studied using CA simulations, namely, orthogonal cutting and ultrasonic welding. The machining microstructure modeling analysis, as presented in Chapters 3 and 4, focused on grain refinement and white etching layer formation on the machined surface. In the orthogonal cutting case study, recrystallized grains by dDRX were observed within the bulk work material followed by a thermomechanical relaxation stage. The microstructure evolution mechanisms inside the chip material were directly simulated using CA method based on dislocation density evolution.

For the ultrasonic welding case study, the same set of experiments presented in Chapter 2 were simulated. The microstructure modeling analysis presented in Chapter 2 employed empirical relationships, such as the Zener–Hollomon equation and the Hall-Patch equation, to predict final bulk material microstructures, omitting the highly dynamic ultrasonic loading at 20 kHz and non-equilibrium dislocation dynamics during the ultrasonic welding process. In this chapter, a high-fidelity finite element-based numerical approach is developed for the first time to simulate dynamic material response under the 20-kHz horn vibration during ultrasonic welding. Using these dynamic responses, a direct simulation of the microstructure evolution inside the bulk material was performed using a CA method based on dislocation density evolution.

5.1 Review of Microstructure Simulation for dDRX in SPD Processes

Discontinuous dynamic recrystallization has been identified as the major microstructure evolution mechanism for the bulk material during SPD processes, e.g. ultrasonic welding of Cu [143] and orthogonal cutting of Al alloy 1100 [26]. There have been a significant number of researches on DRX in the SPD manufacturing processes. However, existing finite element-based SPD process models are inadequate because the process-microstructure relationship is traditionally modeled in an uncoupled manner, which relies on tabular databases and is unable to adequately capture the implicit, dynamic, non-equilibrium nature of the SPD processes. As reviewed in Section 1.3, phenomenological material constitutive models and empirical relationships, such as Zener–Hollomon equation and Hall-Patch equation, were implemented in these FE

modeling work [17–23] to predict final bulk material microstructure, which were unable of simulating the dynamic process of recrystallization.

In last two decades, the CA method has been used to simulate the microstructure evolution governed by DRX during hot forming processes of various metals, e.g., carbon and alloy steels [204–212], copper [213–219], magnesium alloys [220–222], and titanium alloy [223,224]. However, all these previous researches focused on the process conditions under a constant temperature and a constant low or quasi-static strain rate. Nonetheless, the development of CA technique has provided the capability of simulating the DRX process during SPD manufacturing processes under dynamic high-gradient thermomechanical loadings. In this chapter, the dislocation density-based numerical framework presented in Chapter 3 was integrated with the CA method to simulate the microstructure evolution under dynamic and high-gradient thermomechanical loadings during SPD processes.

5.2 Microstructure Evolution Modeling and Numerical Implementation using CA

In this work, the CA model was developed in MATLAB to simulate the microstructure evolution inside the bulk work material subjected to severe plastic deformation under elevated temperature and high strain rates. To capture the whole microstructure evolution procedure, a CA simulation consists of three stages: (1) generation of initial grain structure prior to the SPD process; (2) plastic deformation process; and (3) thermomechanical relaxation stage. The numerical framework of this CA model was developed by adopting the method presented by Ding and Guo [217], which

was applied to simulate the microstructure evolution of copper during a quasi-static hot forming process.

To construct the initial grain structure prior to the deformation process, average grain size and the total number of grains in the simulation domain are determined based on the experimental measurements of workpiece microstructures. The simulation domain is discretized into an array of equally spaced square lattice cells. In the initialization step, multiple CA cells are randomly picked as the nucleation sites for initial grains. The total number of these CA cells is equal to the previously determined total number of initial grains. Each nucleus included the picked CA cell and its neighbours. In this study, the 2D von Neumann's neighbouring rule was used, which defines the eight surrounding cells in a 2D Cartesian grid as the neighbours. Hence, each nucleus includes nine CA cells. This definition was achieved by assigning specific values to the following two state variables at each CA cell:

- Variable A - Grain orientation: an integer variable stands for the unique orientation of each grain. This variable is the same for all the cells within one grain. For each nucleus, a random non-zero positive integer is assigned to Variable A of all nine CA cells, whereas integer 0 is assigned to the rest simulation domain.
- Variable B - Index of grain boundary cells: an integer variable to distinguish a cell in the grain interior from a cell on the grain boundary. In this model, integer 1 is assigned to the eight surrounding CA cells, whereas integer 0 is specified for the center CA cell.

During the initialization, nuclei grow following a normal grain growth algorithm, where boundary motion is driven only by local curvature of the grain boundary. The initial structure is completely constructed as soon as the driving force reaches zero, i.e., positive Variable A populates over the whole simulation domain.

The microstructure simulation starts with the second stage deformation process. The following describes several basic assumptions implemented in this CA model for the microstructure evolution during the deformation process:

(1) A homogenous material structure without any crystalline defect is assumed as the initial condition. Grain rotation is not considered in this numerical model.

(2) Grain boundary energy based on the evolution of dislocation density is considered as the major driving force of recrystallization. Effects of elastic strain energy and surface energy are not considered in this model.

(3) dDRX is considered as the major recrystallization mechanism in this study. Grain nucleation happens only at the grain boundary including primary grain boundary and recrystallized grain boundary, and occurs as the dislocation density reaches the critical value. The critical value of dislocation density depends on the process thermomechanical loading conditions. It is assumed newly recrystallized grains have a low level of dislocation density.

(4) The process thermomechanical loading is uniformly distributed over the whole simulation domain, since only a small area, typically less than 500×500 μm^2 in size, is considered in this study.

The primary state variables are defined at each CA lattice cell as the following:

- Variable A - Grain orientation: an integer variable stands for the unique orientation of each grain, which is randomly generated during the formation of initial structure and dDRX nucleation. The value of this variable is the same for all the cells within one grain.
- Variable B - Index of grain boundary cells: an integer variable to distinguish a cell in the grain interior from a cell on the grain boundary. In this model, it was set to 0 and 1 for the cell in the grain interior and the cell on the grain boundary, respectively.
- Variable C - Total dislocation density: a double floating-point variable stands for the total dislocation density. A uniform initial dislocation density is defined over the initial grain structure.
- Variable D - Index of recrystallized grains: an integer variable with an initial value of zero for the primary matrix grains. For each recrystallized grain, this index is updated when its nucleus is formed in sequence. The maximum of this label is the total amount of recrystallized grains.

The evolution of material dislocation density greatly influenced the nucleation, dDRX and grain growth. Hence, the total dislocation density (Variable C) played the most important role in this CA microstructure evolution simulation. The dislocation density of work material evolves as it undergoes work hardening and dynamic recovery (softening), sometimes simultaneously, during a deformation process. In this framework, the internal state variables are used to evaluate the dislocation generation due to plastic

deformation, dislocation annihilation by dynamic recovery, and interaction between the dislocation cell interiors and cell walls, as detailed by Eqs. (3-3 to 3-9) in Section 3.3. The dislocation density evolutions at the cell interiors and cell walls are subjected to the comprehensive process loading conditions, which will be obtained from the finite element-based process simulations.

The occurrence of nucleation during DRX is determined based on the accumulation of dislocations. As the dislocation density in deformed work material reaches a critical dislocation density, nuclei will start to form on grain boundaries for DRX during the thermomechanical process [52,74,225–227]. The value of this critical level depends on the loading conditions, such as temperature and strain rate [215,217]. Roberts and Ahlblom [228] modeled the critical dislocation density and assumed the subgrain size as the dislocation mean-free path. In prior CA models for DRX during low-strain rate or quasi-static hot working processes, the subgrain size was estimated based on the steady-state creep stress [229]. Considering the dynamic thermomechanical loadings during ultrasonic welding and orthogonal cutting, the dislocation mean free path was estimated using the dislocation cell size d in this model. The critical dislocation density ρ_{crit} is given as:

$$\rho_{\text{crit}} = \left(\frac{20\Gamma_{gb}\dot{\varepsilon}}{3bdM_{gb}\xi^2} \right)^{1/3} \tag{5-1}$$

where Γ_{gb} is the grain boundary energy, M_{gb} is the grain boundary mobility, and ξ is the dislocation line energy. These are given by [217]:

$$\Gamma_{gb} = \frac{Gb\theta_{\mathrm{m}}}{4\pi(1-\nu)} \tag{5-2}$$

$$M_{gb} = \frac{\delta D_{0\mathrm{b}} b}{K_b T} \exp\left(-\frac{Q_{\mathrm{b}}}{RT}\right) \tag{5-3}$$

$$\xi = c_1 Gb^2 \tag{5-4}$$

where G is shear modulus, θ_m is misorientation for a high angle boundary (assumed as 15°), ν is Poisson's ratio, K_b is the Boltzmann constant, T is temperature in Kelvin, δ is the grain boundary thickness of the material, D_{ob} is the grain boundary self-diffusion coefficient at 0 K, Q_b is activation energy of grain boundary self-diffusion, R is the ideal gas constant, and c_1 is a material parameter.

As dislocation density ρ_{tot} exceeds ρ_{crit}, the nucleus of dynamic recrystallized grains can be formed on the pre-existing grain boundaries subjected to a probabilistic transformation rule to ensure a random distribution of DRX nucleus. A random number P ($0 \leq P \leq 1$) is assigned on the grain boundary cells, and compared with the nucleation probability, P_{nuc}. For P less than P_{nuc}, the cell becomes a dDRX nucleus, and all the state variables are updated accordingly. Otherwise, the cell maintains in the original grain without any change of state variables. P_{nuc} is given as [217]:

$$P_{\mathrm{nuc}} = \dot{n} \times \Delta t \times S_{\mathrm{CA}} \tag{5-5}$$

where Δt is the time increment and S_{CA} is the area of a lattice cell. For square cells in this study, $S_{CA} = L_{CA}^2$, where L_{CA} is a single cell length. The dDRX nucleation rate, $\dot{n}$, is a function of the activation energy for deformation (Q_{act}) given by [217]:

$$\dot{\rho}_{nu}(\dot{\varepsilon},T) = c_2 \dot{\varepsilon} \exp\left(-Q_{act}/RT\right) \quad (5\text{-}6)$$

where c_2 is a material parameter. Once this transformation rule is satisfied, the ρ_c and ρ_w will be reset to ρ_{co} and ρ_{wo} at the nucleation sites, i.e., a strain-free level. If the plastic strain is continuously increased, the dislocation density also increases due to the accumulation of dislocations during the further plastic deformation.

Grain growth at the nucleation sites is usually driven by reduction of the total grain boundary energy. A key gradient of dislocation energy presents due to the heterogeneity of dislocation density near the recrystallized grain. The grain boundary tends to move from the recrystallized grain with a low dislocation density to the adjacent matrix grain with a high dislocation density. For a certain recrystallized grain, the grain growth rate (V) is given by [217]:

$$V = M_{gb} F \quad (5\text{-}7)$$

where F is the growth driving force per unit area of the recrystallized grain, which is given by [217]:

$$F = \xi(\rho_{tot,m} - \rho_{tot,\mathrm{DRX}}) - 2\Gamma/r \quad (5\text{-}8)$$

where $\rho_{tot,DRX}$ and $\rho_{tot,m}$ are the total dislocation density of this recrystallized grain and its adjacent matrix grains, respectively; r is the radius of this recrystallized grain; Γ is the grain boundary energy between this recrystallized grain and its adjacent matrix grain. Γ is given by [217]:

$$\Gamma = \begin{cases} \Gamma_{\mathrm{m}} \dfrac{\theta}{\theta_m}[1-\ln(\dfrac{\theta}{\theta_m})] & for \quad \theta \le \theta_m \\ \Gamma_{\mathrm{m}} & for \quad \theta \le \theta_m \end{cases} \tag{5-9}$$

where θ is the orientation difference between this recrystallized grain and its adjacent matrix grains. Then, the grain boundary migration distance, L_G, is determined by:

$$L_G = V\Delta t \tag{5-10}$$

and the radius of this recrystallized grains r is given as [211]:

$$r = \sqrt{N_{DRX} \cdot S_{CA}/\pi} \tag{5-11}$$

where N_{DRX} is the total number of the CA cells held by this recrystallized grain. As the grain growth rate V is reduced to zero, the grain growth stops. The recrystallization progress is captured by the volume fraction of recrystallized grains, X_{RX}:

$$X_{\mathrm{RX}} = \frac{N_{\mathrm{RX}}}{N_X \cdot N_Y} \tag{5-12}$$

where N_{RX} is the total cell number in recrystallized grains, and N_X and N_Y are the total cell numbers along X-axis and Y-axis, respectively, in the 2D simulation domain.

CA grain growth will continue evolve following the grain growth kinetics in Eqs. (5-7, 8, 9), even as the deformation process stops. During this cooling stage, the workpiece material undergoes thermomechanical relaxation process, while recrystallized grains grow until the driving force F reduces to zero. Notably, the time duration for the cooling stage can be significantly longer than the deformation process duration, even as the simulation domain and spatial resolution remain the same.

The flowchart as shown in Figure 5.1 summarizes the principle of the numerical implementation of the CA microstructure simulation under the complex dynamic thermomechanical loading for SPD processes. The dynamic process thermomechanical loadings are obtained and extracted from FE-based process simulations.

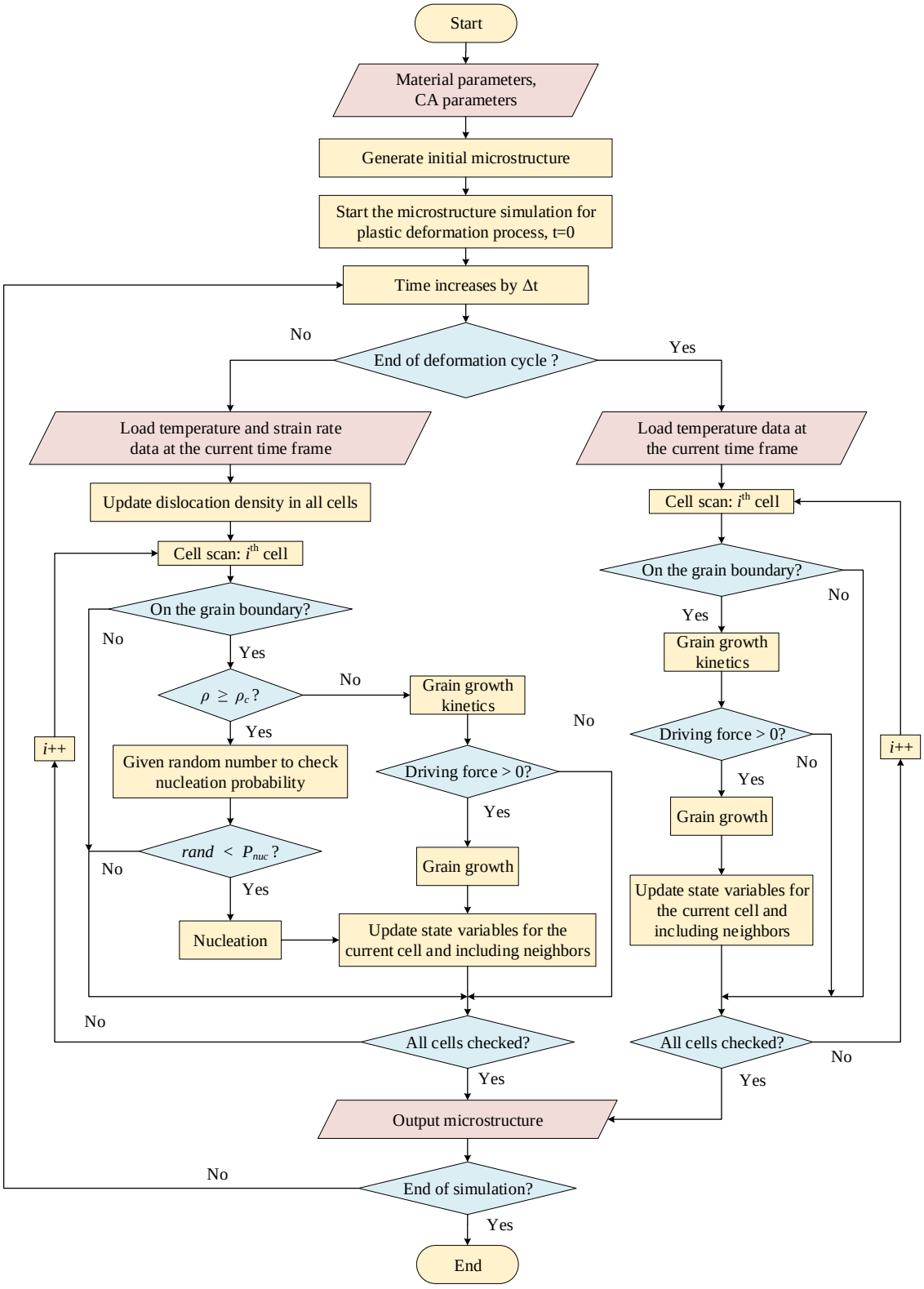

Figure 5.1 CA simulation flowchart.

5.3 Case Study I: Orthogonal Cutting of AA 1100

For the first case study of orthogonal cutting, recrystallized grains by dDRX were observed within the bulk work material processed by orthogonal cutting followed by a thermomechanical relaxation stage. The microstructure modeling analysis developed in this section is based on a previously published orthogonal cutting experimental study of aluminium alloy 1100 (AA 1100) by Ni et al. [26]. During their experiments, ceramic cutting tool inserts with a rake angle of -5° were used at a cutting speed of 0.6 m/s and a feed of 0.3 mm/rev. Both dry and wet cutting conditions were applied. To investigate the transitional microstructure change inside the bulk material during cutting, these orthogonal cutting tests were stopped as they reached the steady state, and the work material ahead of the tool tip was obtained for microstructural analysis.

By quickly stopping (freezing) the cutting process, the cutting deformation process stopped, while the workpiece material microstructure continued to evolve during thermomechanical relaxation. Very fine equiaxed grains about 50 nm in size were found in the cutting primary deformation zone, which were considered as the newly formed nuclei during the recrystallization process. Under a dry cutting condition, the grains in the secondary deformation zone were found to have experienced significant thermally driven grain growth, due to more dissipated heat induced by the friction at tool-chip interface. Under the wet cutting condition, thermally driven grain growth was suppressed in the secondary deformation zone due to the combined effects of lubrication and cooling.

The microstructure evolution mechanisms of the above process, including both orthogonal cutting and thermomechanical relaxation stages, were directly simulated

inside the chip material, particularly near the primary and secondary deformation zones, using CA method based on dislocation density evolution.

A 2D CA model is developed for the first time to model microstructure evolution during orthogonal cutting of AA 1100. Prior to the CA simulation, the dynamic thermomechanical loadings of work material induced by various orthogonal cutting conditions are firstly simulated by a FE-based cutting model. Multiple mechanisms of microstructure evolution are coupled through dislocation density dynamics in the CA model including SPD, dynamic recovery, DRX, and thermally driven grain growth. As shown in Figure 5.2, the microstructures at two selected locations were simulated in this study: location *A* in the primary deformation zone, and location *B* in the secondary deformation zone.

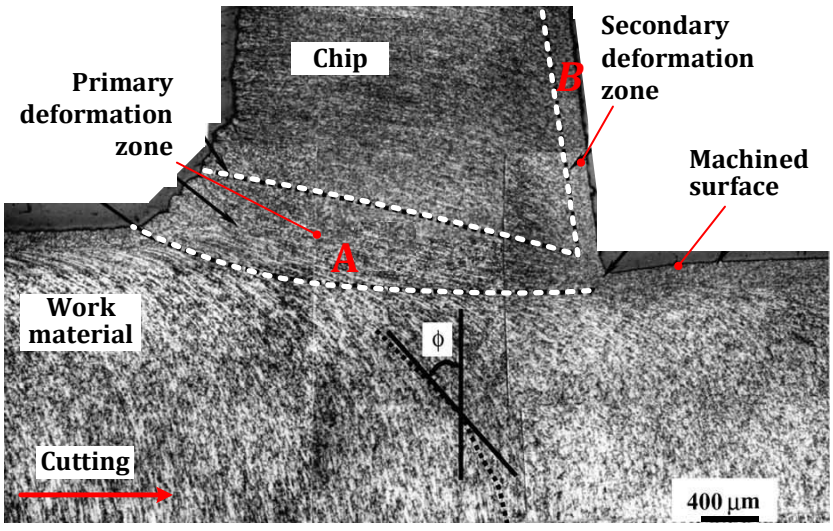

Figure 5.2 Optical micrograph of AA 1100 (original image adopted from Ni et al. [26]).

5.3.1 FE Cutting Process Simulations

A 2D FE model was developed using AdvantEdge™ to evaluate the dynamic thermomechanical loadings at steady state during the cutting process. A 12 mm length of cut was simulated to achieve the steady state status. The Johnson-Cook model of AA 1100 [230] and the silicon nitride-based ceramic tool material was applied in the AdvantEdge™ model. The coolant heat transfer coefficient was determined as 1500 W/m^2-K by a cutting simulation with immersed coolant enabled. The coefficient of friction was determined as 0.5 and 0.3 for the dry cutting and wet cutting, respectively. Figure 5.3 shows the simulated steady-state distributions of temperature and strain rate from the AdvantEdge™ simulation for the cutting stage. In a dry cutting simulation, the temperature was slightly above 100 °C at location *A* near the bottom of shear zone, whereas it could be as high as 247 °C for location *B* on the chip surface. For strain rate, it was about 1500 s^{-1} and 5200 s^{-1} at *A* and *B*, respectively. Due to the high cutting speed, the simulated plastic deformation was finished within 1 ms. Within this short duration, temperature was rapidly increased to the peak temperature, and the strain rate increased to the peak value but dropped to zero rapidly. The recrystallization process is unlikely to be finished within this short duration. Hence, the temperature history during cooling stage should also be considered. To obtain the temperature history during the cooling stage, an implicit ABAQUS heat transfer analysis was conducted to simulate the cooling temperature history under a natural convection. The steady-state cutting temperature distribution simulated by AdvantEdge™ was then imported into ABAQUS as the initial condition for the cooling stage simulation.

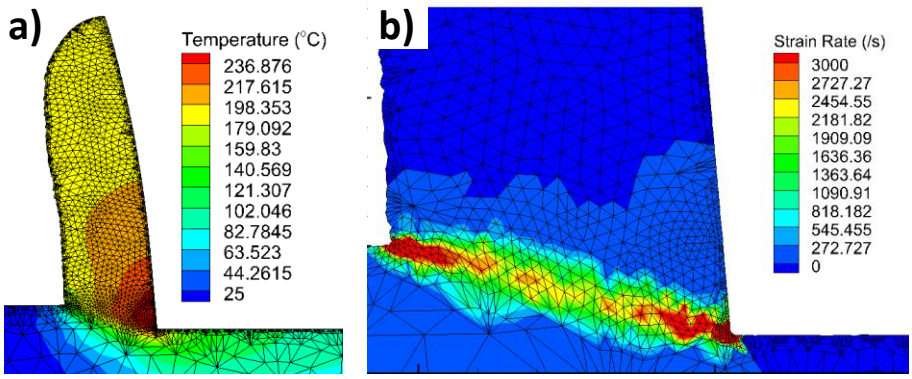

Figure 5.3 Steady-state dry cutting simulation: (a) temperature; (b) strain rate.

5.3.2 CA Simulation Results and Discussions

The formation of recrystallized microstructures in the primary (location A) and secondary (location B) deformation zones shown in Figure 5.2 is simulated using the CA simulations. Table 5.1 lists the simulation conditions. The thermomechanical loading histories during both cutting and cooling stage were extracted at each location from the corresponding FE simulations. All the CA model parameters are given in Table 5.2, and the material physical properties are given in Table 5.3.

Table 5.1 CA simulations.

No.	Location	Coolant	Simulation domain (μm^2)	L_{CA} (nm)
A1	A	No	4×2	10
A2	B	No	20×10	50
A3	B	Yes	4×2	10

Table 5.2 Model parameters for microstructure evolution model of AA 1100 [35].

α^*	β^*	k_o	$\dot{\gamma}_o$	f_o	f_∞	M_T	$\tilde{\gamma}^r$	K_d	c_1	c_2
0.061	0.011	6.3-7.8	6000	0.25	0.06	3.06	3.2	30	5	1e28

Table 5.3 Material physical properties of AA 1100 [231–233].

E (GPa)	G (GPa)	ν	b (nm)	ρ (kg/m^3)	T_m (°C)	α (10^{-6}/°C)	k_c (W/m·°C)	c_p (J/kg·°C)	Q_{act} (kJ/mol)	Q_b (kJ/mol)	δD_{ob} (m^3/s)
68.9	26	0.33	0.286	2710	660	23.6	222	896	142	82	5e-14

Figure 5.4 shows the simulated microstructures from the CA model and compares the simulation results with the experimental results from Ni et al. [26]. Under the dry cutting condition, different microstructures were simulated in the primary and secondary deformation zones. For the primary deformation zone (location *A*), Figure 5.4a shows small DRX nuclei are formed sporadically along the grain boundary of the pre-existing grains. The process of recrystallization was initiated but was not completed. A bimodal distribution of grain size as shown in Figure 5.4h captures both the DRX nuclei and pre-existing sheared grains. The peak near 50 nm corresponds to the small DRX nuclei. In the secondary deformation zone (location *B*), Figure 5.4b shows the process of recrystallization was completed and the whole domain were replaced by the recrystallized grains. The simulation results match well with the TEM micrograph as shown in Figure 5.4e.

The effect of cutting process temperature is further investigated by comparing the simulations in the secondary deformation zone under dry and wet cutting conditions. Under the wet cutting condition, an ultrafine grain structure was obtained as shown in Figure 5.4c, and the whole domain was occupied with submicron recrystallized grains. Under the dry cutting condition, grains were relatively larger (greater than 1 μm) and have undergone a more significant thermally driven grain growth process, i.e., grain

coarsening. These results are mainly caused by the different temperature loadings from the two cutting conditions.

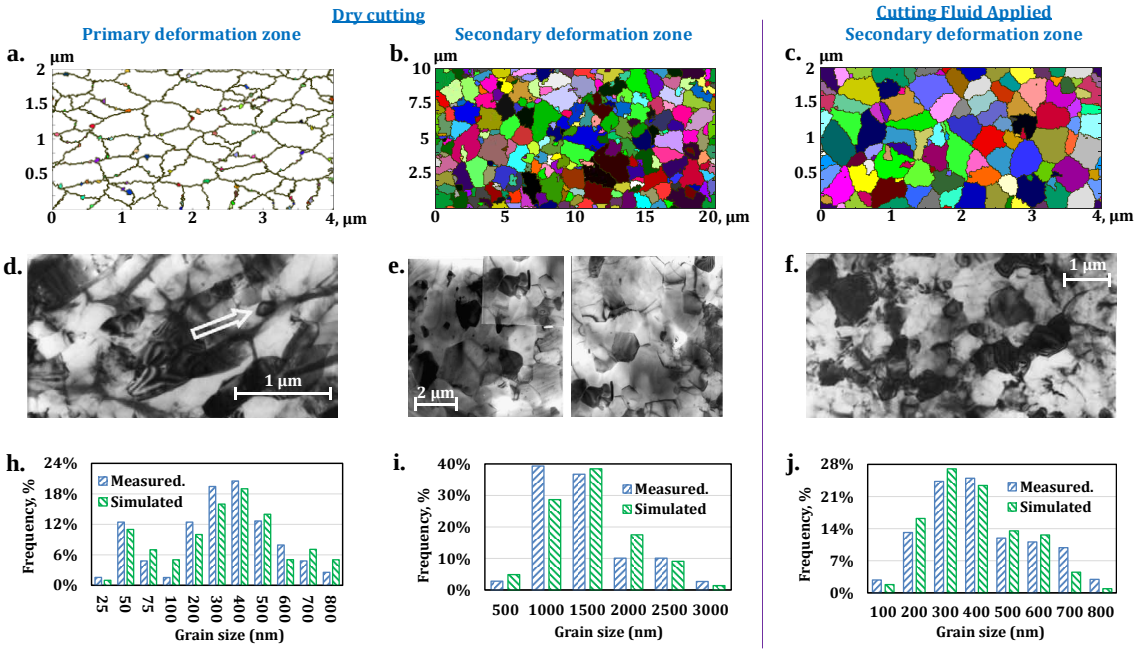

Figure 5.4 The (a-c) predicted microstructures, (d-f) TEM micrographs, and histograms of the measured and (h-j) predicted grain size distributions from the three CA simulations for the bottom of the shear zone in dry cutting, chip surface layer in dry cutting, and chip surface layer with cutting fluid. Experimental measured data and TEM graphs are adopted from Ni et al. [26].

The temperature histories in the secondary deformation zone were simulated as shown in Figure 5.5a for the two cutting conditions. During dry cutting, the work material temperature reached to 248 °C ($0.56T_m$) by the end of cutting process. Then, it maintains a high temperature greater than $0.5T_m$ for additional 2 s during the cooling process. In comparison, under the wet cutting condition, the work material temperature was much lower and never exceeded $0.5T_m$, due to a combined effect of cooling and lubrication of the cutting fluid. It has been extensively reported that the thermally driven

grain growth is more significant when temperature is above 0.5-0.6T_m [234]. Under the dry cutting condition, the work material in the secondary deformation zone underwent a more significant grain coarsening after the completion of recrystallization. In addition, the simulated evolutions of volume fraction of the recrystallized grains were significantly different under the two cutting conditions as shown in Figure 5.5b. During dry cutting, it took about 0.3 s to complete the recrystallization process, whereas it took about 0.6 s under the wet cutting condition.

In this study, the simulation results also show that recrystallization process is initiated as the work material passes through the primary deformation zone to the chip, and requires an additional time duration to complete. As shown in Figure 5.5b, as material passes to the secondary deformation zone after 1 ms, the volume fraction of recrystallized grains X_{RX} was only about 3% and 1% for dry and wet cutting conditions, respectively. Then, the recrystallization process continued and eventually formed the final microstructure inside the chip after the cutting process. Hence, the CA simulations quantitatively revealed that the discontinuous dynamic recrystallization process usually cannot be completed by the end of the rapid cutting process. A similar conclusion was also reported by McQueen [189], who noted nuclei formed just before the cessation of deformation can lead to rapid recrystallization as no incubation is required.

Notably, it was the first time to analyze the complete recrystalliztion even as the plastic deformation process stops. To the author's best knowledge, this phenomenon has not been captured or even considered in any previous modeling work for SPD manufacturing processes.

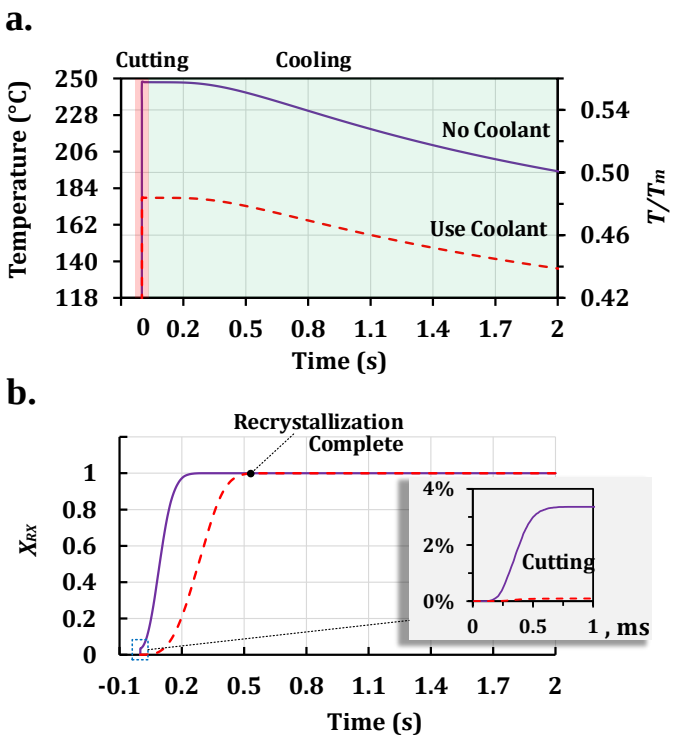

Figure 5.5 Effect of coolant on microstructure evolution: (a) temperature history simulated by the FE model in the chip surface layer over both cutting and cooling stages; (b) X_{RX} history simulated by the CA model in the chip surface layer simulated over both cutting and cooling stages.

5.4 Case Study II: Ultrasonic Welding of Copper

The numerical framework developed in Chapter 2 provided a computationally cost-effective approach to predict the final bulk material microstructures based on empirical dynamic recrystallization kinetics. However, this model is unable to capture either the material dynamic response under 20-kHz ultrasonic vibrations or non-equilibrium dislocation dynamics during the ultrasonic welding process. For the second case study of ultrasonic welding, a high-fidelity ultrasonic welding model was developed in ABAQUS/Explicit for the first time to simulate dynamic material response under the

actual process loading, namely, 20-kHz in-plane horn vibration and a constant vertical clamping force. Using these dynamic responses, a 2D CA model was for the first time developed to model microstructure evolution during ultrasonic welding of copper. The effects of welding duration were mainly evaluated on the microstructure evolution within the bulk material.

5.4.1 High-Fidelity FE Simulation of Ultrasonic Welding

A high-fidelity FE modeling approach was developed using ABAQUS/Explicit to simulate dynamic material response under the 20-kHz horn vibration during ultrasonic welding, and capture its effects on the bulk material microstructure evolution. The dynamic welding force response and vibrational behaviors of anvil and coupons can be directly simulated in this model.

Figure 5.6 shows the model configuration of the 3D ABAQUS/Explicit model. The high-frequency process loading condition was directly modeled by applying a 20 kHz in-plane vibration with 30 μm amplitude to the horn. A constant clamping force, equivalent to a clamping pressure ranged from 40 psi to 60 psi, was applied to the horn along the vertical during the whole welding duration. Stapla Gen-1 knurl pattern geometry and fine diamond anvil pattern were applied in this FE process model. The anvil was modeled as rigid, and all degrees of freedom (DoFs) were constrained on its bottom surface. The thickness of tab and bus work materials were 0.2 mm and 0.9 mm, respectively, and they were modeled as 30×30 mm^2 in area. The material constitutive model introduced in Section 2.4 was applied in this high-fidelity FE model, which considers the material response under high-frequency cyclic loading, thermal softening,

and acoustic softening. Cai et al. [235] conducted systematic experimental measurements of friction coefficient between battery tabs and coupons, and evaluated the effects of surface conditions, sliding frequency, and normal load on the friction coefficient using a reciprocating sliding apparatus. In this study, the friction coefficient between the horn and tab was determined to be 0.8, and the friction coefficient between the tab and bus was 1.2 adapted from Cai et al. [235].

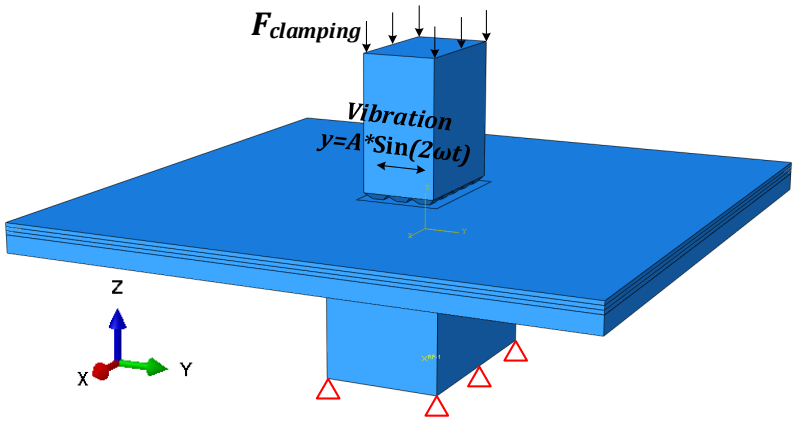

Figure 5.6 3D ABAQUS/Explicit model configuration for ultrasonic welding.

Unrealistic large equivalent plastic strains (PEEQ) are usually simulated in the ABAQUS/Explicit simulations for ultrasonic welding. For instance, Siddiq and Ghassemieh [151,152] presented an extremely large PEEQ simulation value of 80 for an ultrasonic consolidation process with a horn vibration amplitude of only 8.4 μm. PEEQ is the accumulation of increments calculated by the equivalent plastic strain rate, $\dot{\bar{\varepsilon}}^{pl}$ (scalar, always positive), and time increment, which is given by [236]:

$$PEEQ = \bar{\varepsilon}_0^{pl} + \int_0^t \dot{\bar{\varepsilon}}^{pl} dt \,, where\ \dot{\bar{\varepsilon}}^{pl} = \sqrt{\frac{2}{3}\dot{\boldsymbol{\varepsilon}}^{pl} : \dot{\boldsymbol{\varepsilon}}^{pl}} \qquad (5\text{-}13)$$

PEEQ is the time integral of a nonnegative quantity, and its value at a certain material point can only increase even when a high-speed vibration is applied bi-directionally. Multiple ABAQUS simulations were performed to simulate PEEQ using various material hardening rules, such as linear kinematic hardening model and non-linear combined isotropic/kinematic hardening model with cyclic hardening rules. Artificially high values of PEEQ, e.g., over 50, were obtained from all these simulations. Therefore, in this study, it is concluded that it is not correct to use PEEQ to describe the equivalent plastic strain by the ultrasonic welding process.

To correctly account for the magnitude of equivalent plastic strain during ultrasonic welding, a new state variable, plastic strain magnitude, was developed in ABAQUS/Explicit by adopting an ABAQUS/Standard state variable. The plastic strain magnitude, PEmag, is calculated based on the plastic strain components and given by:

$$PEmag = \sqrt{\frac{2}{3}\boldsymbol{\varepsilon}^{pl}:\boldsymbol{\varepsilon}^{pl}} \tag{5-14}$$

A user subroutine VUSDFLD was developed to output the plastic strain magnitude and calculate the PEmag in the simulation. Another user subroutine of VUHARD was also developed for material constitutive model to calculate the flow stress using PEmag from VUSDFLD rather than PEEQ. In this way, correct equivalent plastic strain distribution can be obtained from simulations, and strain was correctly accounted in the constitutive model.

Figure 5.7 shows the simulation contours of Von Mises stress, temperature, displacement and equivalent plastic strain distribution in the tab after 0.2 s welding. The large deformation due to the tool knurl pattern can be clearly seen in the welding zone,

where bulges can be seen at the area between two adjacent knurl tip imprints along both the X- and Y-direction.

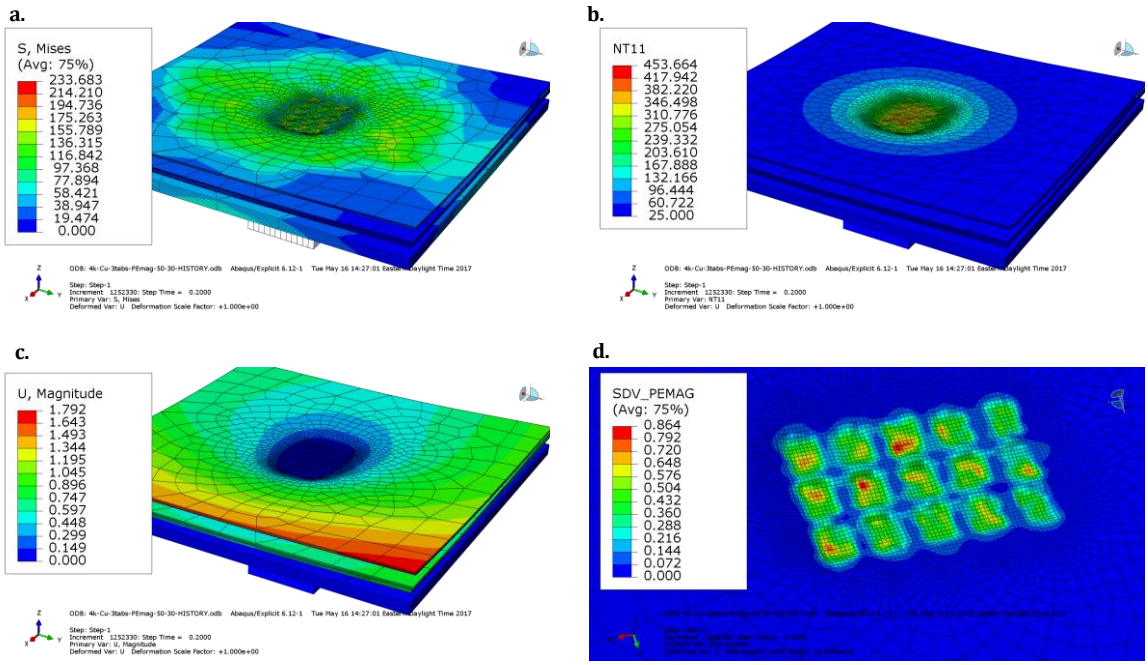

Figure 5.7 3D FE simulation contours: (a) Von Mises stress in MPa; (b) temperature in °C; (c) displacement in mm; (d) equivalent plastic strain (PEmag).

In addition, the 3D ABAQUS/Explicit model can simulate the real-time deformation, frictional heat generation and dynamic welding force behaviors under the 20-kHz horn vibration. This model can be also used to predict the coupon slippage and anvil vibration in all directions by using proper boundary conditions.

The dynamic welding force under the 20-kHz in-plane horn vibration can be well captured by this high-fidelity process model. Figure 5.8 shows the dynamic force histories in the vertical (out-of-plane) direction obtained from the simulation for different time durations. To avoid an extremely large ABAQUS output file, a low output rate, e.g.,

6 frames/100 cycles, was usually applied over the ultrasonic welding simulation. However, as shown in Figure 5.8a, the low frequency cannot properly capture the dynamic trends under the high frequency loading, and caused aliasing in dynamic force output. To properly capture the high-frequency dynamic force responses under the 20-kHz vibration, a high output rate must be applied, e.g., 200 kHz (10 frames per cycle). Due to the limitation on the output file size, the high-frequency dynamic force responses were captured over a short period of time, e.g., 5 ms, in the middle of a simulation. This was achieved by pausing a simulation with low output rate at a certain time frame, then restarting the simulation with a high output rate for 5 ms. Figure 5.8b-e show the high-frequency dynamic force responses captured with a 200-kHz output rate over 0.100-0.105 s, 0.200-0.205 s, 0.300-0.305 s, and 0.400-0.405 s, respectively.

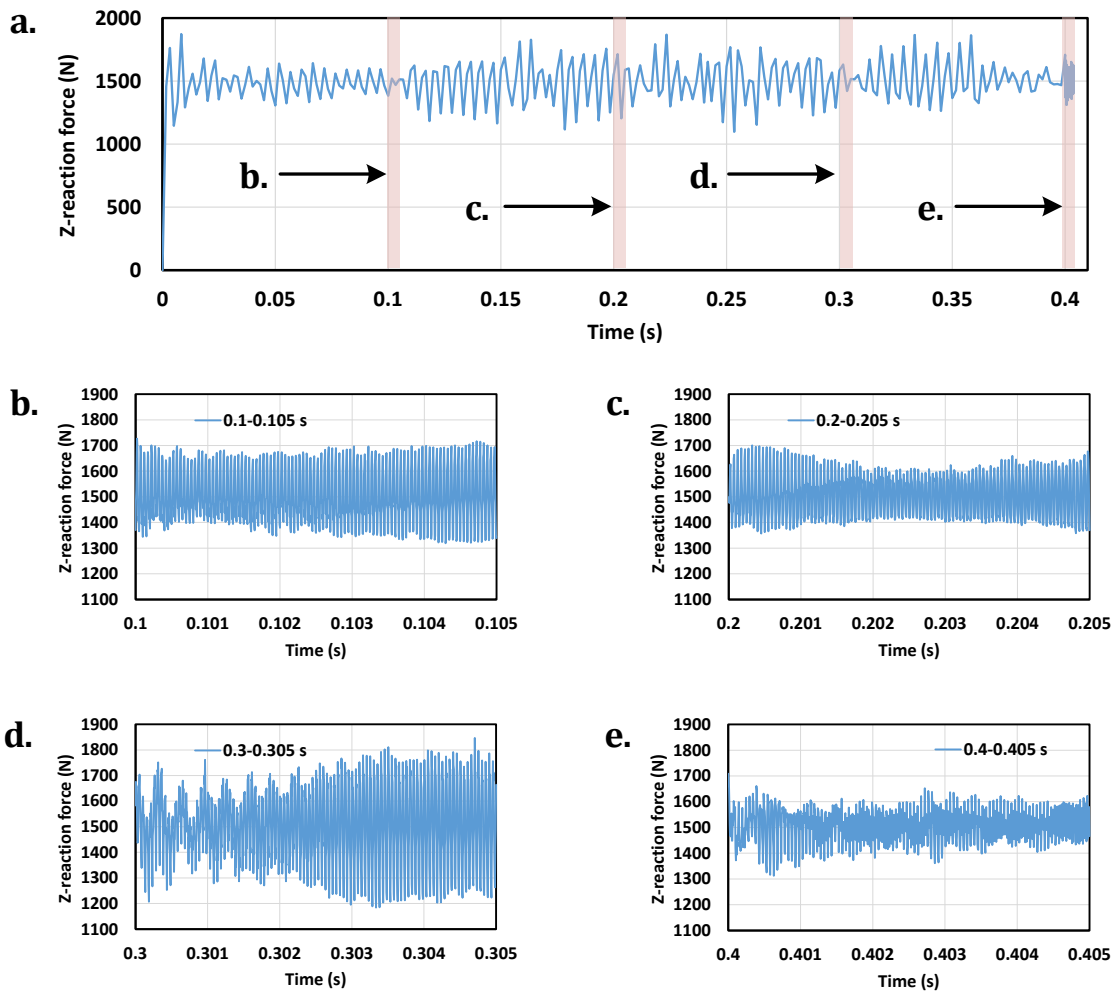

Figure 5.8 The simulated dynamic welding force histories under 20 kHz horn vibration in a 3D ABAQUS simulation: (a) the simulated welding force history over 0.4 s with a low output rate of 6 frames/100 cycles; the simulated welding force history over a short duration of 5 ms with a high output rate of 10 frames/cycles during (b) 0.100-0.105 s, (c) 0.200-0.205 s, (d) 0.300-0.305 s, and (e) 0.400-0.405 s.

Fast Fourier Transform (FFT) analysis was carried out to analyze the dynamic welding force in frequency domain. As shown in Figure 5.9a, a high peak was observed at 20 kHz, corresponding to the 20-kHz ultrasonic horn vibration loading, while the other minor peaks corresponded to its high-frequency variants. These analysis results indicate

the high-fidelity FE process model can correctly capture the dynamic tool-material interactions under ultrasonic loading.

In this study, the dynamic welding force prediction was for the first time compared with the experimental force measurements in the vertical (out-of-plane) direction, which was obtained using Kistler® SlimLine dynamometer [237]. The predicted average force magnitude agreed very well with the experimental measured force data as shown in Figure 5.9b. The predicted welding force oscillated around 1500 N with an amplitude of about 150 N to 300 N over different time durations as shown in Figure 5.8b-d. The simulated force oscillation amplitudes were much smaller than those experimentally obtained in Figure 5.9b, which was about 1000 N (oscillating between 500 N and 2500 N). This discrepancy was mainly attributed to the effect of a reduced system stiffness by introducing the dynamometer between the anvil and back plate. The reduced system stiffness not only generated a high-amplitude force oscillation, but also drastically increased the horn vibration amplitude in the out-of-plane direction. Due to the limitation of current experimental approach, it is extremely difficult to capture the high-frequency dynamic welding force history without significantly compromising the system stiffness. Using a laser vibrometer dynamic displacement measurement, Wu et al. [237] found the out-of-plane horn vibration amplitude increased from a few microns under the normal working condition to 0.6 mm under the system with the dynamometer inserted. Therefore, during a normal working condition, the ultrasonic welding system has a high stiffness, and is expected to have a much less force oscillation. Based on these experimental analysis, the high-fidelity ABAQUS model developed in this study has been proven to be a useful numerical tool, which can capture the high-frequency dynamic

welding force behavior by predicting the frequency, mean value, and amplitude of the force oscillation during the process.

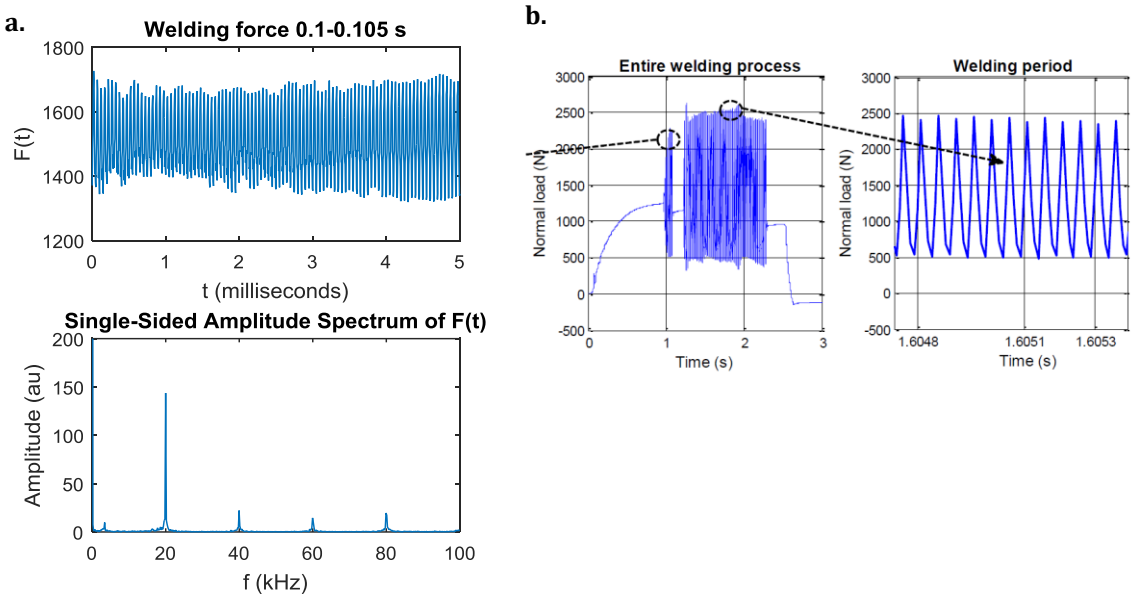

Figure 5.9 The frequency analysis of simulated dynamic welding force under 20 kHz horn vibration: (a) the FFT results over 0.100-0.105 s; (b) the experimental measured dynamic welding force during UW.

The high-fidelity 3D ABAQUS/Explicit model can provide the dynamic thermomechanical loadings for a short welding duration of 0.2 sec. To simulate the loading histories over a long welding duration, e.g., about 1 s, the DEFORM-based computationally cost-effective model as developed in Section 2.5 can be integrated with the high-fidelity ABAQUS model to provide an analysis of thermal and deformation histories over the whole welding process. The input loadings for DEFORM are: (1) equivalent horn Z-displacement history from ABAQUS; (2) 50 Hz in-plane (Y-direction) horn vibration; and (3) equivalent heat fluxes from ABAQUS. To compensate the high-frequency vibration for this low frequency model, the flow stress model was modified to

account for the high strain rate due to the 20kHz vibration. In addition, heat generation term is applied to compensate the frictional heat generation under 20kHz vibration.

5.4.2 CA Simulation Results and Discussion

The discontinuous dynamic recrystallization process at the center of the weld zone, as shown in Figure 2.1, was simulated using CA for the ultrasonic welding process of copper. Three welding durations were applied during the simulations, namely, 0.6 s, 0.8 s, and 1.0 s. All the simulation conditions are listed in Table 5.1 The simulation domain was 160×160 μm^2, and the CA cell size was 0.4 μm. The thermomechanical loading histories over both the welding and cooling stages were extracted at the specific location from the corresponding FE simulations. All the CA model parameters are given in Table 5.5, and the material physical properties are given in Table 5.6.

Table 5.4 CA simulations for the ultrasonic welding of Cu.

No.	Welding duration (s)	Cooling stage (s)	Time increment (s)	Simulation domain (μm^2)	L_{CA} (μm)
B1	1.0	4	0.005	160×160	0.4
B2	0.8	4	0.005	160×160	0.4
B3	0.6	4	0.005	160×160	0.4

Table 5.5 Model parameters for microstructure evolution model of Cu [35].

α^*	β^*	k_o	$\dot{\gamma}_o$	f_o	f_∞	M_T	$\tilde{\gamma}^r$	K_d	c_1	c_2
0.04	0.01	9.0–10.2	200	0.25	0.077	3.06	3.2	10	5	2.5e24

Table 5.6 Material physical properties of Cu [231,233].

E (GPa)	G (GPa)	ν	b (nm)	ρ (kg/m^3)	T_m (°C)	α (10^{-6}/°C)	k_c (W/m·°C)	c_p (J/kg·°C)	Q_{act} (kJ/mol)	Q_b (kJ/mol)	δD_{ob} (m^3/s)
116	48	0.34	0.256	8960	1083	16.6	400	385	261	104	5e-15

The microstructure evolution was captured by the histories of the simulated evolution of the grain structure and dislocation density. Figure 5.10 shows the simulated dDRX microstructure evolution during ultrasonic welding of 1 s welding duration and 4 s cooling stage. As shown in Figure 5.10a, nuclei started to form sporadically at high-angle grain boundaries after 0.3 s welding with a significantly accumulated strain. This simulation result of dDRX initiation agreed well with the experimental observations as discussed in Section 2.1. Recrystallized grains can be seen in the work material after 0.4 s ultrasonic welding, while no sign of DRX nucleation can be observed within the microstructure processed by 0.2 s ultrasonic welding. The CA simulation confirms that dDRX initiation occurred at around 0.3 s ultrasonic welding. With the increase of welding time and accumulated deformation strain, these nuclei underwent a rapid grain growth and started to replace the original grain structure, as shown in Figure 5.10b. In addition, more nuclei continuously form at high-angle grain boundaries of the original and recrystallized structures. These nuclei provide additional sites for grain growth and significantly accelerated the recrystallization process, as shown in Figure 5.10c. As a result, the recrystallized structure almost replaced the whole initial structure by the end of welding process, i.e., t = 1.0 s.

Nucleation of recrystallization stopped as the welding loading was released at the end of the process; however, the recrystallization process continued during the cooling

stage. The accumulated thermal and mechanical energies provided the driving force for grain growth during this stage as shown in Figure 5.10d-e. It can be seen in Figure 5.10d that the original structure had been completely replaced by the recrystallized grains by 0.5 s cooling time. Finally, significantly grown grains were simulated (Figure 5.10e) as the driving force of grain growth gradually became zero. The simulated grain structure and size are in a good agreement with the optical micrograph of final microstructure as shown in Figure 5.10f.

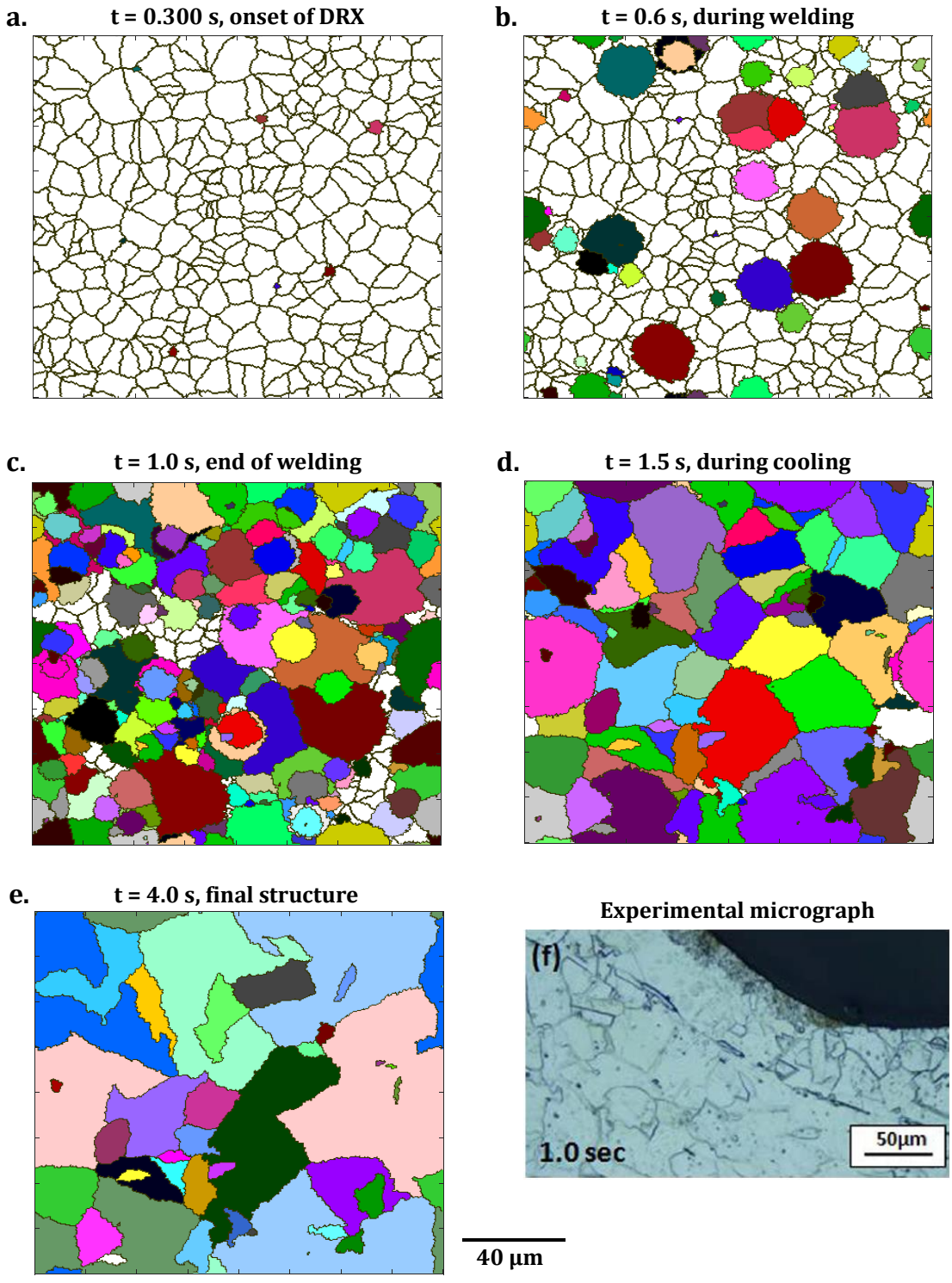

Figure 5.10 CA simulated grain structure evolution for welding duration of 1.0 s over both welding duration and cooling stage: (a) 0.3 s; (b) 0.6 s; (c)1.0 s; (d) 1.5 s; (e) 4.0 s; (f) experimental micrograph of final microstructure.

The driving force for microstructure evolution was examined using the simulation of dislocation density evolution as shown in Figure 5.11. In Figure 5.11a, sporadic dark areas with a low dislocation density started to form, while a uniform high-dislocation density distribution at the rest the simulation domain due to the accumulation of mechanical strains. These dark sports corresponded to the newly formed nuclei as shown in Figure 5.10a. As welding time increased to 0.6 s with further accumulation of plastic deformation, these dark areas for nuclei continued to grow with dislocation density increased to an intermediate level as shown in Figure 5.11b. By the end of welding process, addition recrystallization nuclei started to form at the boundaries of previously recrystallized and initial grains as shown in Figure 5.11c. The simulation shows that significant dislocation density gradients still exists at most grain boundaries by the end of welding process, which provides the driving force for grain growth during the cooling stage. Figure 5.11d shows the dislocation density distribution subjected to thermally driven grain growth during the cooling stage. Since the dislocation accumulation stops at the end of welding process, dislocation density gradients start to diminish over the whole simulation domain. Figure 5.11e shows the final dislocation density distribution, which was uniform over most area of the simulation domain.

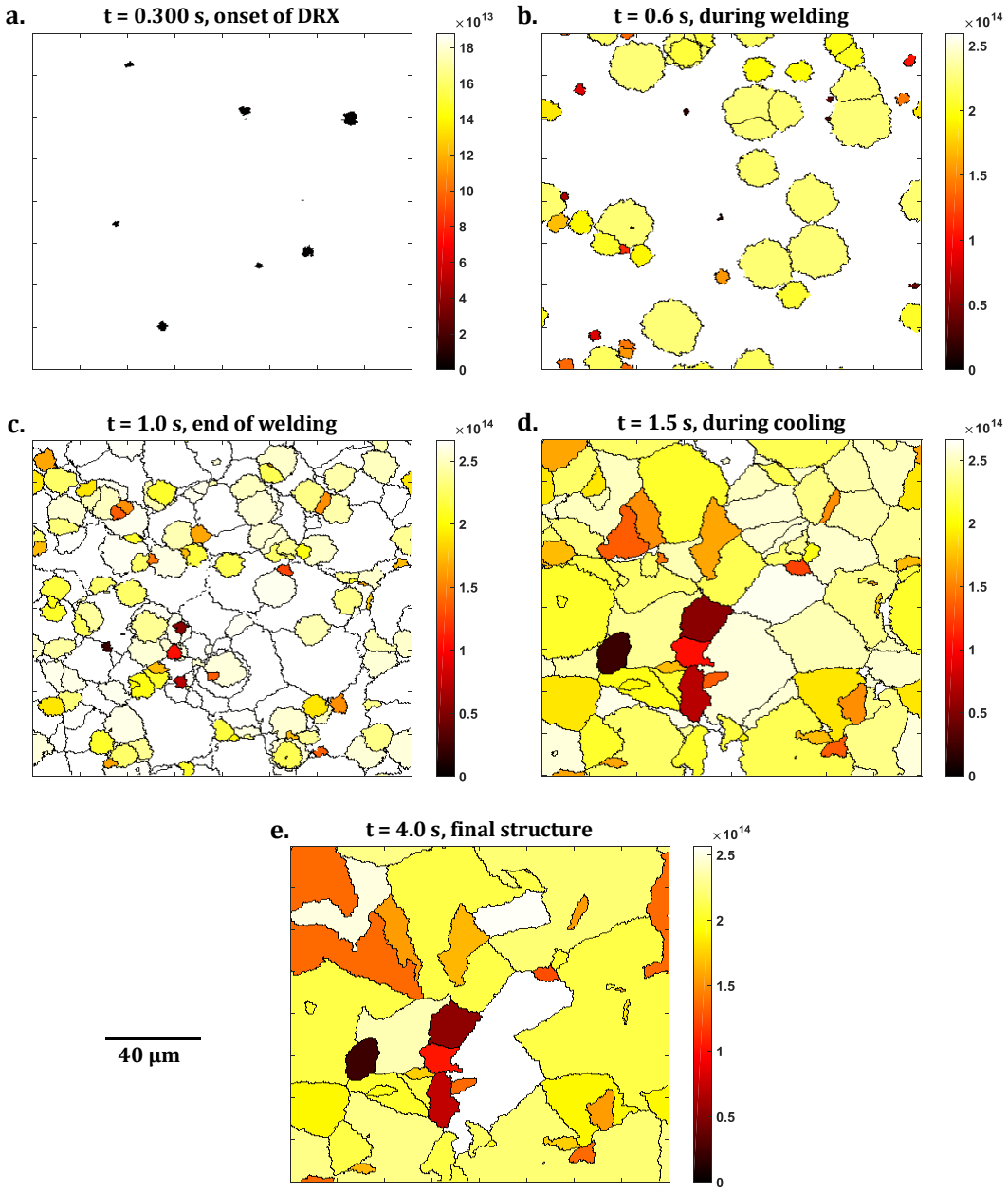

Figure 5.11 Simulated evolution of dislocation density for Case A1 by CA over both welding duration and cooling stage: (a) 0.3 s; (b) 0.6 s; (c)1.0 s; (d) 1.5 s; (e) 4.0 s.

Quantitative assessment of CA simulation results was performed for different welding durations of 0.6 s, 0.8 s, and 1.0 s, in terms of volume fraction of recrystallized grains, dislocation density, and grain size. Figure 5.12a shows the histories of volume

fraction of recrystallized grains X_{RX} for the three welding durations. At the end of welding process, X_{RX} stopped at 0.25, 0.67, and 0.93, for welding durations of 0.6 s, 0.8 s, and 1 s, respectively. Hence, the recrystallization process cannot be completed during the welding stage. During the cooling stage, X_{RX} stopped at 0.77 for the welding duration of 0.6 s, whereas it reached 1.0 for both welding durations of 0.8 s and 1.0 s. This indicated that the initial microstructure was completely replaced by the recrystallized grains for the welding durations of 0.8 s and 1.0 s, whereas the recrystallization process stopped before the recrystallized structure completely replaced the initial structure for welding duration of 0.6 s. Although X_{RX} reached 1.0 for welding durations of 0.8 s and 1.0 s, grain growth continued during the cooling stage, which can be captured by the evolution of average total dislocation density (Figure 5.12b) and average grain size (Figure 5.12c).

Figure 5.12b shows the history of the average total dislocation density over the simulation domain. For all conditions, the dislocation density started to increase with plastic deformation until about 0.3 s, where a plateau can be observed along the history profile of average dislocation density for all three welding durations. This plateau corresponds to the dDRX initiation occurred at around 0.3 s ultrasonic welding. The stall of dislocation density is attributed to significant reduction of work hardening rate induced by dDRX, which greatly decrease the dislocation accumulation rate subjected to plastic deformation as discussed in Section 1.3. As more plastic strain accumulated, the dislocation density started to increase again until the end of welding stage. During this period, dislocations were rapidly accumulated in the recrystallized grains due to the plastic strain increase, and the dislocation densities in these grains increased rapidly to a level comparable to the surrounding grains. During the cooling stage, the average

dislocation density started to decrease due to thermally driven grain growth until a stable level was reached gradually. The slope change of the dislocation density profile can elucidate the decrease of the grain growth driving force during the cooling stage. A stable dislocation density was obtained, when the driving force decreased to zero. In all three conditions, the minimum dislocation density was obtained for 1 s welding duration, because the material was subjected to the longest recrystallization and grain growth process under this condition.

Figure 5.12c shows the history of the average grain size over the whole simulation domain. For welding duration of 0.6 s, the grain growth process stopped soon after the welding stage. For welding durations of 0.8 s and 1.0 s, simulation results show that grain growth mainly occurred during the cooling stage. The final average grain size was 12.0 μm, 20.7 μm, and 25.9 μm for the three welding durations of 0.6 s, 0.8 s, and 1.0 s, respectively. These final grain size values are in a good agreement with the experimental measurement presented in Figure 2.2.

It can be found that these CA simulation results were highly related to process temperature history. Figure 5.12d shows the process temperature history in the welding zone over both welding and cooling stages obtained from FE simulations. Nucleation of dDRX started when the process temperature increased to about $0.4T_m$. In addition, the thermally driven grain growth during the cooling stage was usually ceased when the temperature dropped to about $0.5T_m$. This was also close to the observations in the existing experimental analysis. Hence, for welding duration of 0.6 s, the recrystallization process ceased early due to its lowest process temperature. In comparison, due to the

highest process temperature, recrystallization process stopped latest for 1 s welding duration with the coarsest final microstructure.

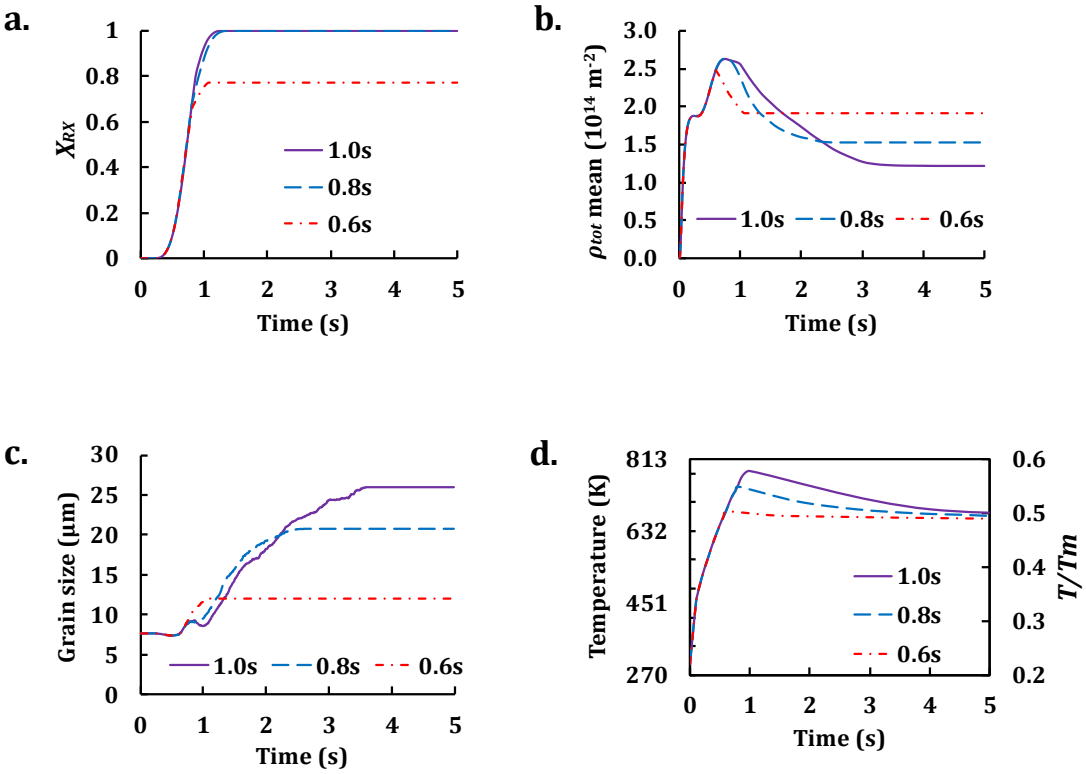

Figure 5.12 CA simulated recrystallization progress histories of (a) volume fraction of the recrystallized domain, (b) mean dislocation density, and (c) average grain size in the weld zone of UW experiments using different welding durations compared with (d) the simulated weld zone temperature history under each condition.

5.5 Summary

A new dislocation density-based CA model was developed for the first time to simulate bulk material microstructure evolution during dDRX-dominated SPD processes under intermediate to high strain rates. The recrystallization processes occurring for two SPD processes, namely, orthogonal cutting of aluminium alloy 1100 and ultrasonic welding of copper, were successfully simulated using the CA method.

For the orthogonal cutting case study, microstructure changes in the primary and secondary deformation zones under dry or wet cutting conditions were evaluated. The microstructure evolution of bulk work material processed by orthogonal cutting followed by a thermomechanical relaxation stage was directly simulated using a CA method based on dislocation density evolution. The CA simulation results agreed with experimental results reported in literature very well. In this study, the CA simulations quantitatively revealed for the first time that the discontinuous dynamic recrystallization process usually cannot be completed by the end of the rapid cutting process. Based on experimental analysis and simulation results, for the fully recrystallized domain (e.g., the secondary deformation zone), temperature was found to be the primary factor in determining microstructure evolution.

For the ultrasonic welding case study, a high-fidelity finite element model was developed for the first time to simulate dynamic material response under the 20-kHz in-plane horn vibration and a constant vertical clamping force during ultrasonic welding. Using these dynamic responses, a direct simulation of the microstructure evolution inside the weld zone was performed using a CA method based on dislocation density evolution. As well as the grain structure evolution, the CA simulation also captured the dislocation density evolution in the grain structure, which provides the driving force for grain growth during both welding and cooling stages. The effects of welding duration on bulk material microstructure evolution were the primary focus of this analysis. Based on the experimental analysis and simulation results, temperature was found to be the major factor in determining the microstructure evolution regime for ultrasonic welding.

CHAPTER 6.

CONCLUSIONS AND FUTURE WORK

6.1 Conclusions

A physics-based dislocation density-based numerical framework has been developed to simulate the microstructure evolution during SPD manufacturing processes for different materials, including copper, Mg alloys, hardened steels, and Al alloys. The simulation results demonstrate the developed model capability of capturing multiple microstructure evolution mechanisms under dynamic or high strain rates over a wide range of temperature during the SPD manufacturing processes, including ultrasonic welding, cryogenic machining, hard drilling, and orthogonal cutting.

Under high temperature and intermediate dynamic strain rate conditions, a metallo-thermo-mechanically coupled 3D FE model has been, for the first time, successfully developed for ultrasonic spot welding to model both weld formation and microstructural evolution. The actual knurl pattern was modeled for the first time to simulate the large deformation in the weld zone during ultrasonic spot welding. A combined isotropic/kinematic hardening flow stress model with an acoustic softening term was implemented to predict material response under high-frequency ultrasonic vibration. Using a post-processing user routine, a kinetics model was implemented to predict the material microstructure evolution governed by DRX and grain growth. The simulated weld zone geometry agreed well with experiment results. The simulations demonstrated that process temperature during ultrasonic welding was highly dependent on the welding time duration. For a welding time duration longer than 0.8 sec, the weld material experienced three different stages of SPD, dynamic recrystallization, and grain

growth. Final distributions of grain size and consequential microhardness were predicted based on the thermomechanical solution fields and agreed well with the experimental measurements.

Under low temperature and high strain rate conditions, a thorough literature review and experimental analysis were performed to elucidate the complicated microstructure evolution mechanism for UFG surface layer formation during cryogenic machining of Mg alloys for the first time. A 2D FE model was then developed in AdvantEdge™ to simulate the enhanced surface integrity of AZ31B Mg alloy by cryogenic machining in two cutting passes, in terms of nanocrystalline grain refinement, increased surface hardness, and compressive residual stress. Based on both slip and twinning mechanisms, a novel physics-based constitutive model has been developed and implemented as a user-defined subroutine to capture material response and grain refinement of AZ31B Mg alloy under cryogenic conditions. Quantitative assessments were carried out with simulated in-depth profiles for all the solution fields – temperature, plastic strain, dislocation density, grain size, UFG layer thickness, microhardness change, and residual stress distribution. Compared with the microstructure and texture below the machined surface before and after cryogenic machining, the FE model also accurately predicted the slip/twinning transition and twinning lamellas resolving in the topmost surface layer of about 20 μm in thickness.

Under high temperature and high strain rate conditions, a thorough review was conducted on the surface nanocrystallization of hardened steels in machining and other SPD processes under various strain rates and process durations for the first time. It is concluded that the surface nanocrystallization and WEL formation of steels during the

machining process are governed by SPD-induced grain refinement accompanied by a strong dynamic recovery effect and thermally driven phase transformation. Dynamic recrystallization does not contribute to machined surface nanocrystallization or WEL formation. A new metallo-thermo-mechanically coupled grain refinement kinetics model based on the evolution of dislocation density was then developed to simulate both SPD-induced grain refinement associated with a strong dynamic recovery effect and thermally driven DPT simultaneously during hard machining of steels. This new kinetics model was developed based on thermodynamic irreversibility in the work material during machining. This MTM coupled grain refinement model was implemented in an FE analysis for a drilling process of hardened AISI 1060 steel. The FE simulation results showed that this MTM coupled grain refinement model successfully captured the surface nanocrystallization and WEL formation of AISI 1060 steel during hard drilling. The analysis based on the thermodynamic irreversibility has the potential to yield a new theoretical approach in studying the physics of surface nanocrystallization during machining of steels.

A new dislocation density-based CA model was developed for the first time to simulate bulk material microstructure evolution during two dDRX-dominated SPD processes, namely orthogonal cutting of AA 1100 and ultrasonic welding of Cu, under intermediate to high strain rates. For the orthogonal cutting case study, CA simulations for the first time quantitatively revealed that discontinuous dynamic recrystallization process usually cannot be completed by the end of the rapid cutting process. For the ultrasonic welding case study, a high-fidelity finite element model was developed for the first time to simulate dynamic material responses under the 20-kHz in-plane horn

vibration during ultrasonic welding. Using these dynamic responses, a direct simulation of microstructure evolution inside the weld zone was performed using a CA method based on dislocation density evolution. In addition to the grain structure evolution, the CA simulation also captured the dislocation density evolution in the grain structure, which constitutes the driving force for grain growth during both welding and cooling stages. In both case studies, experimental analysis and simulation results found temperature to be the major factor in determining the microstructure evolution.

6.2 Recommendations for Future Work

Possible avenues for future research with respect to both computational modeling and experimentation are proposed as follows:

1. Microscopic phase-field models are needed to simulate solid-state phase transformation and nanocrystallization during hard machining of steels. These microscopic models can capture critical physics-based characterization of the metallurgical process, and can be integrated with the metallo-thermo-mechanical coupled numerical framework developed in this dissertation.
2. Discrete dislocation dynamics models are also needed to simulate exact positions and velocities of all dislocation segments subjected to SPD process loading conditions at each instant. Dislocation motion and multiplication in response to external loading, dislocation interactions (material strength) and the track topology evolution of dislocation networks (microstructure) can be simulated from these models. These modeling results can provide critical

information to the dislocation density evolution model developed from this study.

3. Additional experimental and modeling work is needed to evaluate the effects of acoustic waves on dislocation accumulation at the microscopic level. Current state-of-the-art modeling approaches are predominantly empirical; a fundamental microscopic modeling effort can provide a physics-based evaluation of the acoustic softening effect.

REFERENCES

[1] Wei, Q., Cheng, S., Ramesh, K. ., and Ma, E., 2004, "Effect of Nanocrystalline and Ultrafine Grain Sizes on the Strain Rate Sensitivity and Activation Volume: Fcc versus Bcc Metals," Materials Science and Engineering: A, **381**(1–2), pp. 71–79.

[2] Sun, S., Brandt, M., and Dargusch, M. S., 2010, "Thermally Enhanced Machining of Hard-to-Machine materials—A Review," International Journal of Machine Tools and Manufacture, **50**(8), pp. 663–680.

[3] Jawahir, I. S., Attia, H., Biermann, D., Duflou, J., Klocke, F., Meyer, D., Newman, S. T., Pusavec, F., Putz, M., Rech, J., Schulze, V., and Umbrello, D., 2016, "Cryogenic Manufacturing Processes," CIRP Annals - Manufacturing Technology, **65**(2), pp. 713–736.

[4] Ezugwu, E. O., 2005, "Key Improvements in the Machining of Difficult-to-Cut Aerospace Superalloys," International Journal of Machine Tools and Manufacture, **45**(12–13), pp. 1353–1367.

[5] Grzesik, W., and Wanat, T., 2005, "Comparative Assessment of Surface Roughness Produced by Hard Machining with Mixed Ceramic Tools Including 2D and 3D Analysis," Journal of Materials Processing Technology, **169**(3), pp. 364–371.

[6] Field, R., Kahles, J. F., and Canmett, J. T., 1972, "A Review of Measuring Methods for Surface Integrity," Annals of the CIRP, **21**, pp. 219–238.

[7] Field, M., Kahles, J. F., and Koster, W. P., 1989, "Surface Finish and Surface Integrity," *Machining, Vol 16, ASM Handbook*, ASM International, Materials Park, Ohio, USA, pp. 19–36.

[8] Inoue, T., 2002, "Metallo-Thermo-mechanics—Application to Quenching," *Handbook of Residual Stress and Deformation of Steel, ASM Handbook*, G.E. Totten, M.A.H. Howes, and T. Inoue, eds., ASM International, Materials Park, Ohio, USA, pp. 296–311.

[9] Denis, S., Archambault, P., Gautier, E., Simon, A., and Beck, G., 2002, "Prediction of Residual Stress and Distortion of Ferrous and Non-Ferrous Metals: Current Status and Future Developments," Journal of Materials Engineering and Performance, **11**(1), pp. 92–102.

[10] Bailey, N. S., Tan, W., and Shin, Y. C., 2009, "Predictive Modeling and Experimental Results for Residual Stresses in Laser Hardening of AISI 4140 Steel by a High Power Diode Laser," Surface and Coatings Technology, **203**, pp. 2003–2012.

[11] Ding, H., and Shin, Y. C., 2012, "A Metallo-Thermomechanically Coupled Analysis of Orthogonal Cutting of AISI 1045 Steel," ASME Journal of Manufacturing Science and Engineering, **134**(5), p. 51014.

[12] Arrazola, P. J., Özel, T., Umbrello, D., Davies, M., and Jawahir, I. S., 2013, "Recent Advances in Modelling of Metal Machining Processes," CIRP Annals - Manufacturing Technology, **62**(2), pp. 695–718.

[13] Ehmann, K. F., Kapoor, S. G., DeVor, R. E., and Lazoglu, I., 1997, "Machining Process Modeling: A Review," Journal of Manufacturing Science and Engineering, **119**(4B), p. 655.

[14] Prangnell, P. B., Harris, C., and Roberts, S. M., 1997, "Finite Element Modelling of Equal Channel Angular Extrusion," Scripta Materialia, **37**(7), pp. 983–989.

[15] Guo, Y. Q., Batoz, J. L., Detraux, J. M., and Duroux, P., 1990, "Finite Element Procedures for Strain Estimations of Sheet Metal Forming Parts," International Journal for Numerical Methods in Engineering, **30**(8), pp. 1385–1401.

[16] Bergman, G., and Oldenburg, M., 2004, "A Finite Element Model for Thermomechanical Analysis of Sheet Metal Forming," International Journal for Numerical Methods in Engineering, **59**(9), pp. 1167–1186.

[17] Rotella, G., Dillon, O. W., Umbrello, D., Settineri, L., and Jawahir, I. S., 2013, "Finite Element Modeling of Microstructural Changes in Turning of AA7075-T651 Alloy," Journal of Manufacturing Processes, **15**(1), pp. 87–95.

[18] Tabei, A., Shih, D. S., Garmestani, H., and Liang, S. Y., 2016, "Dynamic Recrystallization of Al Alloy 7075 in Turning," Journal of Manufacturing Science and Engineering, **138**(7), p. 71010.

[19] Jafarian, F., Imaz Ciaran, M., Umbrello, D., Arrazola, P. J., Filice, L., and Amirabadi, H., 2014, "Finite Element Simulation of Machining Inconel 718 Alloy Including Microstructure Changes," International Journal of Mechanical Sciences, **88**, pp. 110–121.

[20] Pu, Z., Umbrello, D., Dillon, O. W., Lu, T., Puleo, D. a., and Jawahir, I. S., 2014, "Finite Element Modeling of Microstructural Changes in Dry and Cryogenic Machining of AZ31B Magnesium Alloy," SME Journal of Manufacturing Processes, **16**(2), pp. 335–343.

[21] Outeiro, J. C., Rossi, F., Fromentin, G., Poulachon, G., Germain, G., and Batista, A. C., 2013, "Process Mechanics and Surface Integrity Induced by Dry and Cryogenic Machining of AZ31B-O Magnesium Alloy," Procedia CIRP, **8**, pp. 487–492.

[22] Umbrello, D., Caruso, S., and Imbrogno, S., 2016, "Finite Element Modelling of Microstructural Changes in Dry and Cryogenic Machining AISI 52100 Steel," Materials Science and Technology, pp. 1–9.

[23] Özel, T., Arısoy, Y. M., and Guo, C., 2016, "Identification of Microstructural Model Parameters for 3D Finite Element Simulation of Machining Inconel 100 Alloy," Procedia CIRP, **46**, pp. 549–554.

[24] Ni, H., and Alpas, A. T., 2003, "Sub-Micrometer Structures Generated during Dry Machining of Copper," Materials Science and Engineering: A, **361**(1–2), pp. 338–349.

[25] Stolyarov, V. V, Zhu, Y. T., Alexandrov, I. V, Lowe, T. C., and Valiev, R. Z., 2003, "Grain Refinement and Properties of Pure Ti Processed by Warm ECAP and Cold Rolling," Materials Science and Engineering A, **343**(1–2), pp. 43–50.

[26] Ni, H., Elmadagli, M., and Alpas, A. T., 2004, "Mechanical Properties and Microstructures of 1100 Aluminum Subjected to Dry Machining," Materials Science and Engineering: A, **385**(1–2), pp. 267–278.

[27] Swaminathan, S., Shankar, M. R., Lee, S., Hwang, J., King, A. H., Kezar, R. F., Rao, B. C., Brown, T. L., Chandrasekar, S., Compton, W. D., and Trumble, K. P., 2005, "Large Strain Deformation and Ultra-Fine Grained Materials by Machining," Materials Science and Engineering: A, **410**–**411**, pp. 358–363.

[28] Shekhar, S., Cai, J., Wang, J., and Shankar, M. R., 2009, "Multimodal Ultrafine Grain Size Distributions from Severe Plastic Deformation at High Strain Rates," Materials Science and Engineering: A, **527**(1–2), pp. 187–191.

[29] Shankar, M. R., Rao, B. C., Lee, S., Chandrasekar, S., King, A. H., and Compton, W. D., 2006, "Severe Plastic Deformation (SPD) of Titanium at near-Ambient Temperature," Acta Materialia, **54**(14), pp. 3691–3700.

[30] Estrin, Y., Tóth, L. S., Molinari, A., and Bréchet, Y., 1998, "A Dislocation-Based Model for All Hardening Stages in Large Strain Deformation," Acta Materialia, **46**, pp. 5509–5522.

[31] Tóth, L. S., Molinari, A., and Estrin, Y., 2002, "Strain Hardening at Large Strains as Predicted by Dislocation Based Polycrystal Plasticity Model," ASME Journal of Engineering Materials and Technology, **124**(1), pp. 71–77.

[32] Baik, S. C., Hellmig, R. J., Estrin, Y., and Kim, H. S., 2003, "Modeling of Deformation Behavior of Copper under Equal Channel Angular Pressing," Zeitschrift fur Metallkunde, **94**(Copyright 2003, IEE), pp. 754–760.

[33] Baik, S. C., Estrin, Y., Kim, H. S., and Hellmig, R. J., 2003, "Dislocation Density-Based Modeling of Deformation Behavior of Aluminium under Equal Channel Angular Pressing," Materials Science and Engineering A, **351**, pp. 86–97.

[34] Baik, S. C., Estrin, Y., Kim, H. S., Jeong, H.-T., and Hellmig, R. J., 2002, "Calculation of Deformation Behavior and Texture Evolution during Equal Channel Angular Pressing of IF Steel Using Dislocation Based Modeling of Strain Hardening," Materials Science Forum, **408**–**412**, pp. 697–702.

[35] Ding, H., Shen, N., and Shin, Y. C., 2011, "Modeling of Grain Refinement in Aluminum and Copper Subjected to Cutting," Computational Materials Science, **50**(10), pp. 3016–3025.

[36] Ding, H., and Shin, Y. C., 2014, "Dislocation Density-Based Grain Refinement Modeling of Orthogonal Cutting of Titanium," ASME Journal of Manufacturing Science and Engineering, **136**(4), p. 41003.

[37] Shen, N., Ding, H., Pu, Z., Jawahir, I. S., and Jia, T., 2017, "Enhanced Surface Integrity from Cryogenic Machining of AZ31B Mg Alloy: A Physics-Based Analysis with Microstructure Prediction," ASME Journal of Manufacturing Science and Engineering, **139**(6), p. 61012.

[38] Ding, H., and Shin, Y. C., 2013, "Multi-Physics Modeling and Simulations of Surface Microstructure Alteration in Hard Turning," Journal of Materials Processing Technology, **213**(6), pp. 877–886.

[39] Ding, H., Shen, N., and Shin, Y. C., 2012, "Predictive Modeling of Grain Refinement during Multi-Pass Cold Rolling," Journal of Materials Processing Technology, **212**(5), pp. 1003–1013.

[40] Ding, H., and Shin, Y. C., 2012, "Dislocation Density-Based Modeling of Subsurface Grain Refinement with Laser-Induced Shock Compression," Computational Materials Science, **53**(1), pp. 79–88.

[41] Shen, N., Ding, H., Bowers, R., Yu, Y., Pence, C. N., Ozbolat, I. T., and Stanford, C. M., 2015, "Surface Micropatterning of Pure Titanium for Biomedical Applications Via High Energy Pulse Laser Peening," ASME Journal of Micro and Nano-Manufacturing, **3**(1), p. 11005.

[42] Liu, R., Salahshoor, M., Melkote, S. N., and Marusich, T., 2014, "A Unified Internal State Variable Material Model for Inelastic Deformation and Microstructure Evolution in SS304," Materials Science and Engineering: A, **594**, pp. 352–363.

[43] Liu, R., Salahshoor, M., Melkote, S. N., and Marusich, T., 2014, "The Prediction of Machined Surface Hardness Using a New Physics-Based Material Model," Procedia CIRP, **13**, pp. 249–256.

[44] Liu, R., Salahshoor, M., Melkote, S. N., and Marusich, T., 2015, "A Unified Material Model Including Dislocation Drag and Its Application to Simulation of Orthogonal Cutting of OFHC Copper," Journal of Materials Processing Technology, **216**, pp. 328–338.

[45] Ding, L., Zhang, X., and Richard Liu, C., 2014, "Dislocation Density and Grain Size Evolution in the Machining of Al6061-T6 Alloys," Journal of Manufacturing Science and Engineering, **136**(4), p. 41020.

[46] Fernandez-Zelaia, P., Melkote, S., Marusich, T., and Usui, S., 2017, "A Microstructure Sensitive Grain Boundary Sliding and Slip Based Constitutive Model for Machining of Ti-6Al-4V," Mechanics of Materials, **109**, pp. 67–81.

[47] Arısoy, Y. M., and Özel, T., 2015, "Prediction of Machining Induced Microstructure in Ti–6Al–4V Alloy Using 3-D FE-Based Simulations: Effects of Tool Micro-Geometry, Coating and Cutting Conditions," Journal of Materials Processing Technology, **220**, pp. 1–26.

[48] Atmani, Z., Haddag, B., Nouari, M., and Zenasni, M., 2016, "Combined Microstructure-Based Flow Stress and Grain Size Evolution Models for Multi-Physics Modelling of Metal Machining," International Journal of Mechanical Sciences, **118**, pp. 77–90.

[49] Meyers, M. A., Vöhringer, O., and Lubarda, V. A., 2001, "The Onset of Twinning in Metals: A Constitutive Description," Acta Materialia, **49**(19), pp. 4025–4039.

[50] Meyers, M. A., Benson, D. J., Vöhringer, O., Kad, B. K., Xue, Q., and Fu, H.-H., 2002, "Constitutive Description of Dynamic Deformation: Physically-Based Mechanisms," Materials Science and Engineering: A, **322**(1–2), pp. 194–216.

[51] Knezevic, M., Levinson, A., Harris, R., Mishra, R. K., Doherty, R. D., and Kalidindi, S. R., 2010, "Deformation Twinning in AZ31: Influence on Strain Hardening and Texture Evolution," Acta Materialia, **58**(19), pp. 6230–6242.

[52] Sun, H. Q., Shi, Y.-N., Zhang, M.-X., and Lu, K., 2007, "Plastic Strain-Induced Grain Refinement in the Nanometer Scale in a Mg Alloy," Acta Materialia, **55**(3), pp. 975–982.

[53] Pu, Z., Outeiro, J. C., Batista, A. C., Dillon, O. W., Puleo, D. A., and Jawahir, I. S., 2012, "Enhanced Surface Integrity of AZ31B Mg Alloy by Cryogenic Machining towards Improved Functional Performance of Machined Components," International Journal of Machine Tools and Manufacture, **56**, pp. 17–27.

[54] Pu, Z., Song, G.-L., Yang, S., Outeiro, J. C., Dillon, O. W., Puleo, D. a., and Jawahir, I. S., 2012, "Grain Refined and Basal Textured Surface Produced by Burnishing for Improved Corrosion Performance of AZ31B Mg Alloy," Corrosion Science, **57**, pp. 192–201.

[55] Ulacia, I., Salisbury, C. P., Hurtado, I., and Worswick, M. J., 2011, "Tensile Characterization and Constitutive Modeling of AZ31B Magnesium Alloy Sheet over Wide Range of Strain Rates and Temperatures," Journal of Materials Processing Technology, **211**(5), pp. 830–839.

[56] Watanabe, H., Ishikawa, K., and Mukai, T., 2007, "High Strain Rate Deformation Behavior of Mg–Al–Zn Alloys at Elevated Temperatures," Key Engineering Materials, **340**–**341**, pp. 107–112.

[57] Ulacia, I., Dudamell, N. V., Gálvez, F., Yi, S., Pérez-Prado, M. T., and Hurtado, I., 2010, "Mechanical Behavior and Microstructural Evolution of a Mg AZ31 Sheet at Dynamic Strain Rates," Acta Materialia, **58**(8), pp. 2988–2998.

[58] Koike, J., Kobayashi, T., Mukai, T., Watanabe, H., Suzuki, M., Maruyama, K., and Higashi, K., 2003, "The Activity of Non-Basal Slip Systems and Dynamic Recovery at Room Temperature in Fine-Grained AZ31B Magnesium Alloys," Acta Materialia, **51**(7), pp. 2055–2065.

[59] Koike, J., and Ohyama, R., 2005, "Geometrical Criterion for the Activation of Prismatic Slip in AZ61 Mg Alloy Sheets Deformed at Room Temperature," Acta Materialia, **53**(7), pp. 1963–1972.

[60] Agnew, S. R., and Duygulu, Ö., 2005, "Plastic Anisotropy and the Role of Non-Basal Slip in Magnesium Alloy AZ31B," International Journal of Plasticity, **21**(6), pp. 1161–1193.

[61] Keshavarz, Z., and Barnett, M. R., 2006, "EBSD Analysis of Deformation Modes in Mg–3Al–1Zn," Scripta Materialia, **55**(10), pp. 915–918.

[62] Li, B., Joshi, S., Azevedo, K., Ma, E., Ramesh, K. T., Figueiredo, R. B., and Langdon, T. G., 2009, "Dynamic Testing at High Strain Rates of an Ultrafine-Grained Magnesium Alloy Processed by ECAP," Materials Science and Engineering: A, **517**(1–2), pp. 24–29.

[63] Sakai, T., Belyakov, A., Kaibyshev, R., Miura, H., and Jonas, J. J., 2014, "Dynamic and Post-Dynamic Recrystallization under Hot, Cold and Severe Plastic Deformation Conditions," Progress in Materials Science, **60**(1), pp. 130–207.

[64] Sellars, C. M., 1978, "Recrystallization of Metals during Hot Deformation," Philosophical Transactions of the Royal Society of London. Series A, Mathematical and Physical Sciences, **288**(1350), pp. 147–158.

[65] Mcqueen, H. J., and Jonas, J. J., 1984, "Recent Advances in Hot Working: Fundamental Dynamic Softening Mechanisms," Journal of Applied Metalworking, **3**(3), pp. 233–241.

[66] Sakai, T., 1995, "Dynamic Recrystallization Microstructures under Hot Working Conditions," Journal of Materials Processing Technology, **53**(1–2), pp. 349–361.

[67] Quan, G.-Z., "Characterization for Dynamic Recrystallization Kinetics Based on Stress-Strain Curves," *Recent Developments in the Study of Recrystallization*.

[68] Yanagimoto, J., Karhausen, K., Brand, A. J., and Kopp, R., 1998, "Incremental Formulation for the Prediction of Flow Stress and Microstructural Change in Hot Forming," ASME Journal of Manufacturing Science and Engineering, **120**(2), p. 316.

[69] Sellars, C. M., 1990, "Modelling Microstructural Development during Hot Rolling," Materials Science and Technology, **6**(11), pp. 1072–1081.

[70] Yada, H., 1988, "Prediction of Microstructural Changes and Mechanical Properties in Hot Strip Rolling," *Proceedings of the Metallurgical Society of the Canadian Institute of Mining and Metallurgy,* Elsevier, pp. 105–119.

[71] Laasraoui, A., and Jonas, J. J., 1991, "Recrystallization of Austenite after Deformation at High Temperatures and Strain Rates - Analysis and Modeling," Metallurgical transactions. A, Physical metallurgy and materials science, **22 A**(1), pp. 151–160.

[72] Kim, S.-I., and Yoo, Y.-C., 2001, "Dynamic Recrystallization Behavior of AISI 304 Stainless Steel," Materials Science and Engineering: A, **311**(1–2), pp. 108–113.

[73] Serajzadeh, S., and Karimi Taheri, A., 2003, "Prediction of Flow Stress at Hot Working Condition," Mechanics Research Communications, **30**(1), pp. 87–93.

[74] Xu, Y., Hu, L. X., and Sun, Y., 2014, "Dynamic Recrystallization Kinetics of as-Cast AZ91D Alloy," Transactions of Nonferrous Metals Society of China (English Edition), **24**(6), pp. 1683–1689.

[75] Kocks, U. F., 1976, "Laws for Work-Hardening and Low-Temperature Creep," Journal of Engineering Materials and Technology, **98**(1), p. 76.

[76] Mecking, H., and Kocks, U. F., 1981, "Kinetics of Flow and Strain-Hardening," Acta Metallurgica, **29**(11), pp. 1865–1875.

[77] Burns, T. J., Mates, S. P., Rhorer, R. L., Whitenton, E. P., and Basak, D., 2011, "Effect on Flow Stress of a Rapid Phase Transition in AISI 1045 Steel," *ASME 2011 International Manufacturing Science and Engineering Conference, Volume 1*, ASME, pp. 261–266.

[78] Burns, T. J., Mates, S. P., Rhorer, R. L., Whitenton, E. P., and Basak, D., 2011, "Dynamic Properties for Modeling and Simulation of Machining: Effect of Pearlite to Austenite Phase Transition on Flow Stress in AISI 1075 Steel," Machining Science and Technology, **15**, pp. 1–20.

[79] Chou, Y. K., and Evans, C. J., 1999, "White Layers and Thermal Modeling of Hard Turned Surfaces," International Journal of Machine Tools and Manufacture, **39**(12), pp. 1863–1881.

[80] Barry, J., and Byrne, G., 2002, "TEM Study on the Surface White Layer in Two Turned Hardened Steels," Materials Science and Engineering: A, **325**(1–2), pp. 356–364.

[81] Han, S., Melkote, S. N., Haluska, M. S., and Watkins, T. R., 2008, "White Layer Formation due to Phase Transformation in Orthogonal Machining of AISI 1045 Annealed Steel," Materials Science and Engineering: A, **488**(1–2), pp. 195–204.

[82] Akcan, S., Shah, W. S., Moylan, S. P., Chandrasekar, S., Chhabra, P. N., and Yang, H. T. Y., 2002, "Formation of White Layers in Steels by Machining and Their Characteristics," Metallurgical and Materials Transactions A, **33**(4), pp. 1245–1254.

[83] Jawahir, I. S. S., Brinksmeier, E., M'Saoubi, R., Aspinwall, D. K. K., Outeiro, J. C. C., Meyer, D., Umbrello, D., and Jayal, A. D. D., 2011, "Surface Integrity in Material Removal Processes: Recent Advances," CIRP Annals - Manufacturing Technology, **60**(2), pp. 603–626.

[84] Ramesh, A., Melkote, S. N., Allard, L. F., Riester, L., and Watkins, T. R., 2005, "Analysis of White Layers Formed in Hard Turning of AISI 52100 Steel," Materials Science and Engineering A, **390**, pp. 88–97.

[85] Todaka, Y., Umemoto, M., Li, J., and Tsuchiya, K., 2005, "Nanocrystallization of Drill Hole Surface by High Speed Drilling," Journal of Metastable and Nanocrystalline Materials, **24–25**, pp. 601–604.

[86] Li, J. G., Umemoto, M., Todaka, Y., and Tsuchiya, K., 2007, "A Microstructural Investigation of the Surface of a Drilled Hole in Carbon Steels," Acta Materialia, **55**, pp. 1397–1406.

[87] Thakur, A., Mohanty, A., and Gangopadhyay, S., 2014, "Comparative Study of Surface Integrity Aspects of Incoloy 825 during Machining with Uncoated and CVD Multilayer Coated Inserts," Applied Surface Science, **320**, pp. 829–837.

[88] Thakur, A., Gangopadhyay, S., and Maity, K. P., 2014, "Effect of Cutting Speed and Tool Coating on Machined Surface Integrity of Ni-Based Super Alloy," Procedia CIRP, **14**, pp. 541–545.

[89] Umbrello, D., 2013, "Investigation of Surface Integrity in Dry Machining of Inconel 718," International Journal of Advanced Manufacturing Technology, **69**(9–12), pp. 2183–2190.

[90] Bushlya, V., Zhou, J. M., Lenrick, F., Avdovic, P., and Ståhlan, J. E., 2011, "Characterization of White Layer Generated When Turning Aged Inconel 718," Procedia Engineering, **19**, pp. 60–66.

[91] Zhou, J. M., Bushlya, V., Peng, R. L., Johansson, S., Avdovic, P., and Stahl, J. E., 2011, "Effects of Tool Wear on Subsurface Deformation of Nickelbased Superalloy," Procedia Engineering, **19**, pp. 407–413.

[92] Du, J., Liu, Z., and Lv, S., 2014, "Deformation-Phase Transformation Coupling Mechanism of White Layer Formation in High Speed Machining of FGH95 Ni-Based Superalloy," Applied Surface Science, **292**, pp. 197–203.

[93] M'Saoubi, R., Axinte, D., Herbert, C., Hardy, M., and Salmon, P., 2014, "Surface Integrity of Nickel-Based Alloys Subjected to Severe Plastic Deformation by Abusive Drilling," CIRP Annals - Manufacturing Technology, **63**(1), pp. 61–64.

[94] Herbert, C. R. J., Axinte, D. A., Hardy, M. C., and Brown, P. D., 2011, "Investigation into the Characteristics of White Layers Produced in a Nickel-Based Superalloy from Drilling Operations," Procedia Engineering, **19**, pp. 138–143.

[95] Imran, M., Mativenga, P. T., Gholinia, A., and Withers, P. J., 2011, "Evaluation of Surface Integrity in Micro Drilling Process for Nickel-Based Superalloy," International Journal of Advanced Manufacturing Technology, **55**(5–8), pp. 465–476.

[96] Veldhuis, S. C., Dosbaeva, G. K., Elfizy, A., Fox-Rabinovich, G. S., and Wagg, T., 2010, "Investigations of White Layer Formation During Machining of Powder Metallurgical Ni-Based ME 16 Superalloy," Journal of Materials Engineering and Performance, **19**(7), pp. 1031–1036.

[97] Che-Haron, C. H., and Jawaid, A., 2005, "The Effect of Machining on Surface Integrity of Titanium Alloy Ti–6% Al–4% V," Journal of Materials Processing Technology, **166**(2), pp. 188–192.

[98] Hasçalık, A., and Çaydaş, U., 2007, "Electrical Discharge Machining of Titanium Alloy (Ti–6Al–4V)," Applied Surface Science, **253**(22), pp. 9007–9016.

[99] Che-Haron, C. ., 2001, "Tool Life and Surface Integrity in Turning Titanium Alloy," Journal of Materials Processing Technology, **118**(1–3), pp. 231–237.

[100] Ezugwu, E. O., and Wang, Z. M., 1997, "Titanium Alloys and Their Machinability—a Review," Journal of Materials Processing Technology, **68**(3), pp. 262–274.

[101] Machado, A. R., and Wallbank, J., 1990, "Machining of Titanium and Its Alloys—a Review," Proceedings of the Institution of Mechanical Engineers, Part B: Journal of Engineering Manufacture, **204**(1), pp. 53–60.

[102] Long, M., and Rack, H. ., 1998, "Titanium Alloys in Total Joint Replacement—a Materials Science Perspective," Biomaterials, **19**(18), pp. 1621–1639.

[103] Griffiths, B. J., 1987, "Mechanisms of White Layer Generation with Reference to Machining and Deformation Processes," Journal of Tribology, **109**(86), pp. 525–530.

[104] Shi, J., and Liu, C. R., 2006, "On Predicting Chip Morphology and Phase Transformation in Hard Machining," The International Journal of Advanced Manufacturing Technology, **27**(7–8), pp. 645–654.

[105] Umbrello, D., and Filice, L., 2009, "Improving Surface Integrity in Orthogonal Machining of Hardened AISI 52100 Steel by Modeling White and Dark Layers Formation," CIRP Annals - Manufacturing Technology, **58**(1), pp. 73–76.

[106] Umbrello, D., Jayal, A. D., Caruso, S., Dillon, O. W., and Jawahir, I. S., 2010, "Modeling of White and Dark Layer Formation in Hard Machining of AISI 52100 Bearing Steel," Machining Science and Technology, **14**, pp. 128–147.

[107] Ramesh, A., and Melkote, S. N., 2008, "Modeling of White Layer Formation under Thermally Dominant Conditions in Orthogonal Machining of Hardened AISI 52100 Steel," International Journal of Machine Tools and Manufacture, **48**(3–4), pp. 402–414.

[108] Caruso, S., Imbrogno, S., Rotella, G., Ciaran, M. I., Arrazola, P. J., Filice, L., and Umbrello, D., 2015, "Numerical Simulation of Surface Modification During Machining of Nickel-Based Superalloy," Procedia CIRP, **31**, pp. 130–135.

[109] Jafarian, F., Umbrello, D., and Jabbaripour, B., 2016, "Identification of New Material Model for Machining Simulation of Inconel 718 Alloy and the Effect of Tool Edge Geometry on Microstructure Changes," Simulation Modelling Practice and Theory, **66**, pp. 273–284.

[110] Caruso, S., Imbrogno, S., Rinaldi, S., and Umbrello, D., 2017, "Finite Element Modeling of Microstructural Changes in Waspaloy Dry Machining," The International Journal of Advanced Manufacturing Technology, **89**(1–4), pp. 227–240.

[111] Özel, T., and Arisoy, Y. M., 2014, "Experimental and Numerical Investigations on Machining Induced Surface Integrity in Inconel-100 Nickel-Base Alloy," Procedia CIRP, **13**, pp. 302–307.

[112] Rana, K., Rinaldi, S., Imbrogno, S., Rotella, G., Umbrello, D., Saoubi, R. M., and Ayvar-Soberanis, S., 2016, "2D FE Prediction of Surface Alteration of Inconel 718 under Machining Condition," Procedia CIRP, **45**, pp. 227–230.

[113] Caruso, S., Di Renzo, S., Umbrello, D., Jayal, A. D., Dillon, O. W., and Jawahir, I. S., 2011, "Finite Element Modeling of Microstructural Changes in Hard Turning," Advanced Materials Research, **223**, pp. 960–968.

[114] Arısoy, Y. M., and Özel, T., 2015, "Investigations on Machining Induced Microstructural Changes in Inconel 100," *Volume 2: Materials; Biomanufacturing; Properties, Applications and Systems; Sustainable Manufacturing*, ASME, p. V002T01A002.

[115] Buchkremer, S., and Klocke, F., 2017, "Modeling Nanostructural Surface Modifications in Metal Cutting by an Approach of Thermodynamic Irreversibility: Derivation and Experimental Validation," Continuum Mechanics and Thermodynamics, **29**(1), pp. 271–289.

[116] Umemoto, M., 2003, "Nanocrystallization of Steels by Severe Plastic Deformation," MATERIALS TRANSACTIONS, **44**(10), pp. 1900–1911.

[117] Todaka, Y., Umemoto, M., Li, J. G., and Tsuchiya, K., 2005, "Nanocrystallization of Carbon Steels by Shock Peening and Drilling," Reviews on Advanced Materials Science, **10**, pp. 409–416.

[118] Todaka, Y., Umemoto, M., Tanaka, S., and Tsuchiya, K., 2004, "Formation of Nanocrystalline Structure at the Surface of Drill Hole in Steel," MATERIALS TRANSACTIONS, **45**(7), pp. 2209–2213.

[119] Wittman, C. L., Meyers, M. A., and Pak, H.-R., 1990, "Observation of an Adiabatic Shear Band in AISI 4340 Steel by High-Voltage Transmission Electron Microscopy," Metallurgical Transactions A, **21**(2), pp. 707–716.

[120] Beatty, J. H., Meyer, L. W., Meyers, M. A., and Nemat- Nasser, S., 1991, "Formation of Controlled Adiabatic Shear Bands in AISI 4340 High Strength Steel," U.S. Army Materials Technology Laboratry Metals Research Branch Report, MTL TR 90-54.

[121] Mgbokwere, C. O., Nutt, S. R., and Duffy, J., 1994, "Shear Band Formation in 4340 Steel: A TEM Study," Mechanics of Materials, **17**(2–3), pp. 97–110.

[122] Zhang, B., Shen, W., Liu, Y., Tang, X., and Wang, Y., 1997, "Microstructures of Surface White Layer and Internal White Adiabatic Shear Band," Wear, **211**(2), pp. 164–168.

[123] Cho, K.-M., Lee, S., Nutt, S. R., and Duffy, J., 1993, "Adiabatic Shear Band Formation during Dynamic Torsional Deformation of an HY-100 Steel," Acta Metallurgica et Materialia, **41**(3), pp. 923–932.

[124] Zhou, Y., Peng, J. F., Luo, Z. P., Cao, B. B., Jin, X. S., and Zhu, M. H., 2016, "Phase and Microstructural Evolution in White Etching Layer of a Pearlitic Steel during Rolling–sliding Friction," Wear, **362**–**363**, pp. 8–17.

[125] Umemoto, M., Todaka, Y., and Tsuchiya, K., 2003, "Formation of Nanocrystalline Structure in Steels by Air Blast Shot Peening," MATERIALS TRANSACTIONS, **44**(7), pp. 1488–1493.

[126] Wang, W. Z., Tang, L. X., and Qu, B. J., 2003, "Mechanical Properties and Morphological Structures of Short Glass Fiber Reinforced PP/EPDM Composite," European Polymer Journal, **39**(11), pp. 2129–2134.

[127] Ohsaki, S., Hono, K., Hidaka, H., and Takaki, S., 2005, "Characterization of Nanocrystalline Ferrite Produced by Mechanical Milling of Pearlitic Steel," Scripta Materialia, **52**(4), pp. 271–276.

[128] Zhou, L., He, W., Luo, S., Long, C., Wang, C., Nie, X., He, G., Shen, X., and Li, Y., 2016, "Laser Shock Peening Induced Surface Nanocrystallization and Martensite Transformation in Austenitic Stainless Steel," Journal of Alloys and Compounds, **655**, pp. 66–70.

[129] Lu, J. Z., Luo, K. Y., Zhang, Y. K., Sun, G. F., Gu, Y. Y., Zhou, J. Z., Ren, X. D., Zhang, X. C., Zhang, L. F., Chen, K. M., Cui, C. Y., Jiang, Y. F., Feng, A. X., and Zhang, L., 2010, "Grain Refinement Mechanism of Multiple Laser Shock Processing Impacts on ANSI 304 Stainless Steel," Acta Materialia, **58**(16), pp. 5354–5362.

[130] Chen, A. Y., Ruan, H. H., Wang, J., Chan, H. L., Wang, Q., Li, Q., and Lu, J., 2011, "The Influence of Strain Rate on the Microstructure Transition of 304 Stainless Steel," Acta Materialia, **59**(9), pp. 3697–3709.

[131] Ye, C., Suslov, S., Lin, D., and Cheng, G. J., 2012, "Deformation-Induced Martensite and Nanotwins by Cryogenic Laser Shock Peening of AISI 304 Stainless Steel and the Effects on Mechanical Properties," Philosophical Magazine, **92**(11), pp. 1369–1389.

[132] Luo, K. Y., Lu, J. Z., Zhang, Y. K., Zhou, J. Z., Zhang, L. F., Dai, F. Z., Zhang, L., Zhong, J. W., and Cui, C. Y., 2011, "Effects of Laser Shock Processing on Mechanical Properties and Micro-Structure of ANSI 304 Austenitic Stainless Steel," Materials Science and Engineering: A, **528**(13–14), pp. 4783–4788.

[133] Gerland, M., and Hallouin, M., 1994, "Effect of Pressure on the Microstructure of an Austenitic Stainless Steel Shock-Loaded by Very Short Laser Pulses," Journal of Materials Science, **29**(2), pp. 345–351.

[134] Korznikov, A. V., Ivanisenko, Y. V., Laptionok, D. V., Safarov, I. M., Pilyugin, V. P., and Valiev, R. Z., 1994, "Influence of Severe Plastic Deformation on Structure and Phase Composition of Carbon Steel," Nanostructured Materials, **4**(2), pp. 159–167.

[135] Ivanisenko, Y., Lojkowski, W., Valiev, R. Z., and Fecht, H.-J., 2003, "The Mechanism of Formation of Nanostructure and Dissolution of Cementite in a Pearlitic Steel during High Pressure Torsion," Acta Materialia, **51**(18), pp. 5555–5570.

[136] Valiev, R. ., Islamgaliev, R. ., and Alexandrov, I. ., 2000, "Bulk Nanostructured Materials from Severe Plastic Deformation," Progress in Materials Science, **45**(2), pp. 103–189.

[137] Valiev, R. Z., Korznikov, A. V., and Mulyukov, R. R., 1993, "Structure and Properties of Ultrafine-Grained Materials Produced by Severe Plastic Deformation," Materials Science and Engineering: A, **168**(2), pp. 141–148.

[138] Valiev, R. Z., Ivanisenko, Y. V., Rauch, E. F., and Baudelet, B., 1996, "Structure and Deformaton Behaviour of Armco Iron Subjected to Severe Plastic Deformation," Acta Materialia, **44**(12), pp. 4705–4712.

[139] Gunduz, I., Ando, T., Shattuck, E., Wong, P., and Doumanidis, C., 2005, "Enhanced Diffusion and Phase Transformations during Ultrasonic Welding of Zinc and Aluminum," Scripta Materialia, **52**(9), pp. 939–943.

[140] Zhao, J., Li, H., Choi, H., Cai, W., Abell, J. A., and Li, X., 2013, "Insertable Thin Film Thermocouples for in Situ Transient Temperature Monitoring in Ultrasonic Metal Welding of Battery Tabs," SME Journal of Manufacturing Processes, **15**(1), pp. 136–140.

[141] Li, H., Choi, H., Ma, C., Zhao, J., Jiang, H., Cai, W., Abell, J. A., and Li, X., 2013, "Transient Temperature and Heat Flux Measurement in Ultrasonic Joining of Battery Tabs Using Thin-Film Microsensors," ASME Journal of Manufacturing Science and Engineering, **135**(5), p. 51015.

[142] Xu, L., Wang, L., Chen, Y.-C., Robson, J. D., and Prangnell, P. B., 2016, "Effect of Interfacial Reaction on the Mechanical Performance of Steel to Aluminum Dissimilar Ultrasonic Spot Welds," Metallurgical and Materials Transactions A, **47**(1), pp. 334–346.

[143] Lee, S. S., Kim, T.-H., Hu, S. J., Cai, W. W., Abell, J. A., and Li, J., 2013, "Characterization of Joint Quality in Ultrasonic Welding of Battery Tabs," ASME Journal of Manufacturing Science and Engineering, **135**(2), p. 21004.

[144] Bakavos, D., and Prangnell, P. B., 2010, "Mechanisms of Joint and Microstructure Formation in High Power Ultrasonic Spot Welding 6111 Aluminium Automotive Sheet," Materials Science and Engineering: A, **527**(23), pp. 6320–6334.

[145] Chen, J., Zhang, W., Feng, Z., and Cai, W., 2014, "Determination of Thermal Contact Conductance between Thin Metal Sheets of Battery Tabs," International Journal of Heat and Mass Transfer, **69**, pp. 473–480.

[146] Langenecker, B., 1966, "Effects of Ultrasound on Deformation Characteristics of Metals," IEEE Transactions on Sonics and Ultrasonics, **13**(1), pp. 1–8.

[147] Langenecker, B., 1961, "Work-Softening of Metal Crystals by Alternating the Rate of Glide Strain," Acta Metallurgica, **9**(10), pp. 937–940.

[148] Elangovan, S., Semeer, S., and Prakasan, K., 2009, "Temperature and Stress Distribution in Ultrasonic Metal welding—An FEA-Based Study," Journal of Materials Processing Technology, **209**(3), pp. 1143–1150.

[149] De Vries, E., 2004, "Mechanics and Mechanisms of Ultrasonic Metal Welding," The Ohio State University.

[150] Lee, D., Kannatey-Asibu, E., and Cai, W., 2013, "Ultrasonic Welding Simulations for Multiple Layers of Lithium-Ion Battery Tabs," ASME Journal of Manufacturing Science and Engineering, **135**(6), p. 61011.

[151] Siddiq, A., and Ghassemieh, E., 2008, "Thermomechanical Analyses of Ultrasonic Welding Process Using Thermal and Acoustic Softening Effects," Mechanics of Materials, **40**(12), pp. 982–1000.

[152] Siddiq, A., and Ghassemieh, E., 2009, "Theoretical and FE Analysis of Ultrasonic Welding of Aluminum Alloy 3003," ASME Journal of Manufacturing Science and Engineering, **131**(4), p. 41007.

[153] Siddiq, A., and El Sayed, T., 2011, "Acoustic Softening in Metals during Ultrasonic Assisted Deformation via CP-FEM," Materials Letters, **65**(2), pp. 356–359.

[154] Siddiq, A., and Sayed, T. El, 2012, "A Thermomechanical Crystal Plasticity Constitutive Model for Ultrasonic Consolidation," Computational Materials Science, **51**(1), pp. 241–251.

[155] *DEFORM V11.0 (PC) Documentation, 2014*, Scientific Forming Technologies Corporation, Columbus, OH.

[156] Sellars, C. M., and Whiteman, J. A., 1979, "Recrystallization and Grain Growth in Hot Rolling," Metal Science, **13**(3–4), pp. 187–194.

[157] Callister, W. D., and Rethwisch, D. G., 2012, *Fundamentals of Materials Science and Engineering: An Integrated Approach, 4th Edition*, John Wiley & Sons, Hoboken, New Jersey, USA.

[158] Brown, A. A., and Bammann, D. J., 2012, "Validation of a Model for Static and Dynamic Recrystallization in Metals," International Journal of Plasticity, **32**–**33**, pp. 17–35.

[159] Erickson, S. C., 1990, "Properties of Pure Metals," *Properties and Selection: Nonferrous Alloys and Special-Purpose Materials, Vol 2, ASM Handbook*, ASM International, Materials Park, Ohio, USA, pp. 1099–1201.

[160] Krishna, S., 2009, *Unified Constitutive Modeling for Proportional and Nonproportional Cyclic Plasticity Responses*, North Carolina State University.

[161] Johnson, G., and Cook, W., 1983, "A Constitutive Model and Data for Metals Subjected to Large Strains, High Strain Rates and High Temperatures," Proceedings of the 7th International Symposium on Ballistics, p. 541.

[162] Bower, A. F., 1989, "Cyclic Hardening Properties of Hard-Drawn Copper and Rail Steel," Journal of the Mechanics and Physics of Solids, **37**(4), pp. 455–470.

[163] Lee, S. S., Kim, T.-H., Hu, S. J., Cai, W. W., and Abell, J. A., 2015, "Analysis of Weld Formation in Multilayer Ultrasonic Metal Welding Using High-Speed Images," ASME Journal of Manufacturing Science and Engineering, **137**(3), p. 31016.

[164] Zhang, C., Zhu, X., and Li, L., 2006, "A Study of Friction Behavior in Ultrasonic Welding (Consolidation) of Aluminum," *Proceedings of the AWS Conference, Session 7: Friction & Resistance Welding/Materials Bonding Processes*, pp. 151–156.

[165] Rabinowicz, E., 1951, "The Nature of the Static and Kinetic Coefficients of Friction," Journal of Applied Physics, **22**(11), p. 1373.

[166] Wang, Z. Y., and Rajurkar, K. P., 2000, "Cryogenic Machining of Hard-to-Cut Materials," Wear, **239**(2), pp. 168–175.

[167] Paul, S., Dhar, N. ., and Chattopadhyay, A. ., 2001, "Beneficial Effects of Cryogenic Cooling over Dry and Wet Machining on Tool Wear and Surface Finish in Turning AISI 1060 Steel," Journal of Materials Processing Technology, **116**(1), pp. 44–48.

[168] Pusavec, F., Hamdi, H., Kopac, J., and Jawahir, I. S., 2011, "Surface Integrity in Cryogenic Machining of Nickel Based alloy—Inconel 718," Journal of Materials Processing Technology, **211**(4), pp. 773–783.

[169] Ambrosy, F., Zanger, F., Schulze, V., and Jawahir, I. S., 2014, "An Experimental Study of Cryogenic Machining on Nanocrystalline Surface Layer Generation," Procedia CIRP, **13**, pp. 169–174.

[170] Umbrello, D., Yang, S., Dillon, O. W., and Jawahir, I. S., 2012, "Effects of Cryogenic Cooling on Surface Layer Alterations in Machining of AISI 52100 Steels," Materials Science and Technology, **28**(11), pp. 1320–1331.

[171] Turnbull, A., Mingard, K., Lord, J. D., Roebuck, B., Tice, D. R., Mottershead, K. J., Fairweather, N. D., and Bradbury, A. K., 2011, "Sensitivity of Stress Corrosion Cracking of Stainless Steel to Surface Machining and Grinding Procedure," Corrosion Science, **53**(10), pp. 3398–3415.

[172] Bermingham, M. J., Kirsch, J., Sun, S., Palanisamy, S., and Dargusch, M. S., 2011, "New Observations on Tool Life, Cutting Forces and Chip Morphology in Cryogenic Machining Ti-6Al-4V," International Journal of Machine Tools and Manufacture, **51**(6), pp. 500–511.

[173] Denkena, B., and Lucas, A., 2007, "Biocompatible Magnesium Alloys as Absorbable Implant Materials – Adjusted Surface and Subsurface Properties by Machining Processes," CIRP Annals - Manufacturing Technology, **56**(1), pp. 113–116.

[174] Wang, H., Estrin, Y., Fu, H., Song, G., and Zúberová, Z., 2007, "The Effect of Pre-Processing and Grain Structure on the Bio-Corrosion and Fatigue Resistance of Magnesium Alloy AZ31," Advanced Engineering Materials, **9**(11), pp. 967–972.

[175] Wang, L., Fan, Y., Huang, G., and Huang, G., 2003, "Flow Stress and Softening Behavior of Wrought Magnesium Alloy AZ31B at Elevated Temperature," Transactions of Nonferrous Metals Society of China, **13**(2), pp. 335–338.

[176] Liu, J., Cui, Z., and Li, C., 2008, "Modelling of Flow Stress Characterizing Dynamic Recrystallization for Magnesium Alloy AZ31B," Computational Materials Science, **41**(3), pp. 375–382.

[177] Li, W., Zhao, G., Ma, X., and Gao, J., 2012, "Flow Stress Characteristics of AZ31B Magnesium Alloy Sheet at Elevated Temperatures," International Journal of Applied Physics and Mathematics, **2**(2), pp. 83–88.

[178] Giraud, E., Rossi, F., Germain, G., and Outeiro, J. C., 2013, "Constitutive Modelling of AZ31B-O Magnesium Alloy for Cryogenic Machining," *14th CIRP Conference on Modeling of Machining Operations (CIRP CMMO)*, Italy, pp. 522–527.

[179] Barnett, M. R., Keshavarz, Z., Beer, A. G., and Atwell, D., 2004, "Influence of Grain Size on the Compressive Deformation of Wrought Mg–3Al–1Zn," Acta Materialia, **52**(17), pp. 5093–5103.

[180] Shen, N., and Ding, H., 2014, "Physics-Based Microstructure Simulation for Drilled Hole Surface in Hardened Steel," ASME Journal of Manufacturing Science and Engineering, **136**(4), p. 44504.

[181] Hasenpouth, D., 2010, "Tensile High Strain Rate Behavior of AZ31B Magnesium Alloy," University of Waterloo.

[182] Lemiale, V., Estrin, Y., Kim, H. S., and O'Donnell, R., 2010, "Grain Refinement under High Strain Rate Impact: A Numerical Approach," Computational Materials Science, **48**(1), pp. 124–132.

[183] Hibbins, S. G., 1998, "Investigation of Heat Transfer in DC Casting of Magnesium Alloys," Proceedings of the International Symposium on Light Metals, pp. 265–280.

[184] Calamaz, M., Coupard, D., and Girot, F., 2008, "A New Material Model for 2D Numerical Simulation of Serrated Chip Formation When Machining Titanium Alloy Ti–6Al–4V," International Journal of Machine Tools and Manufacture, **48**(3–4), pp. 275–288.

[185] Pu, Z., Umbrello, D., Dillon, O. W., and Jawahir, I. S., 2014, "Finite Element Simulation of Residual Stresses in Cryogenic Machining of AZ31B Mg Alloy," Procedia CIRP, **13**, pp. 282–287.

[186] Bergman, T. L., Incropera, F. P., DeWitt, D. P., and Lavine, A. S., 2011, *Fundamentals of Heat and Mass Transfer*, Wiley, Hoboken, New Jersey, USA.

[187] Lide, D. R., 1994, *Handbook of Chemistry and Physics, 1994 Special Student Edition*, CRC Press, Boca Raton, Florida, USA.

[188] LESLIE, W. C., and HORNBOGEN, E., 1996, "PHYSICAL METALLURGY OF STEELS," *Physical Metallurgy*, R.W. Cahn, P. Haasen, and P. Haasen, eds., Elsevier, pp. 1555–1620.

[189] McQueen, H. J., 1977, "The Production and Utility of Recovered Dislocation Substructures," Metallurgical Transactions A, **8**(6), pp. 807–824.

[190] Zener, C., and Hollomon, J. H., 1944, "Effect of Strain Rate Upon Plastic Flow of Steel," Journal of Applied Physics, **15**(1).

[191] Caccialupi, A., 2003, "Systems Development for High Temperature, High Strain Rate Material Testing of Hardened Steels for Plasticity Behavior Modeling," Geogia Insititute of Technology.

[192] Hodowany, J., Ravichandran, G., Rosakis, A. J., and Rosakis, P., 2000, "Partition of Plastic Work into Heat and Stored Energy in Metals," Experimental Mechanics, **40**(2), pp. 113–123.

[193] Murr, L. E., 1975, *Interfacial Phenomena in Metals and Alloys*, Addison-Wesley Pub. Co., Advanced Book Program.

[194] Chandler, H., 1995, *Heat Treater's Guide - Practices and Procedures for Irons and Steels (2nd Edition)*, ASM International, Novelty, Ohio.

[195] Lakhkar, R. S., Shin, Y. C., and Krane, M. J. M., 2008, "Predictive Modeling of Multi-Track Laser Hardening of AISI 4140 Steel," Materials Science and Engineering: A, **480**(1–2), pp. 209–217.

[196] Lee, C.-H., and Chang, K.-H., 2011, "Prediction of Residual Stresses in High Strength Carbon Steel Pipe Weld Considering Solid-State Phase Transformation Effects," Computers & Structures, **89**, pp. 256–265.

[197] Simsir, C., and Gür, C. H., 2008, "A FEM Based Framework for Simulation of Thermal Treatments: Application to Steel Quenching," Computational Materials Science, **44**, pp. 588–600.

[198] Yaghi, A. H., Hyde, T. H., Becker, A. A., and Sun, W., 2008, "Finite Element Simulation of Welding and Residual Stresses in a P91 Steel Pipe Incorporating Solid-State Phase Transformation and Post-Weld Heat Treatment," Journal of Strain Analysis for Engineering Design, **43**, pp. 275–293.

[199] Bono, M., and Ni, J., 2001, "The Effects of Thermal Distortions on the Diameter and Cylindricity of Dry Drilled Holes," International Journal of Machine Tools and Manufacture, **41**, pp. 2261–2270.

[200] Kalidas, S., Kapoor, S. G., and DeVor, R. E., 2002, "Influence of Thermal Effects on Hole Quality in Dry Drilling, Part 1: A Thermal Model of Workpiece Temperatures," ASME Journal of Manufacturing Science and Engineering, **124**(2), p. 258.

[201] Tai, B. L., Stephenson, D. A., and Shih, A. J., 2012, "An Inverse Heat Transfer Method for Determining Workpiece Temperature in Minimum Quantity Lubrication Deep Hole Drilling," ASME Journal of Manufacturing Science and Engineering, **134**(2), p. 21006.

[202] Strenkowski, J. S., Hsieh, C. C., and Shih, A. J., 2004, "An Analytical Finite Element Technique for Predicting Thrust Force and Torque in Drilling," International Journal of Machine Tools and Manufacture, **44**, pp. 1413–1421.

[203] Nath, A. K., Gupta, A., and Benny, F., 2012, "Theoretical and Experimental Study on Laser Surface Hardening by Repetitive Laser Pulses," Surface and Coatings Technology, **206**, pp. 2602–2615.

[204] Zheng, C., Xiao, N., Li, D., and Li, Y., 2008, "Microstructure Prediction of the Austenite Recrystallization during Multi-Pass Steel Strip Hot Rolling: A Cellular Automaton Modeling," Computational Materials Science, **44**(2), pp. 507–514.

[205] Yazdipour, N., Davies, C. H. J., and Hodgson, P. D., 2008, "Microstructural Modeling of Dynamic Recrystallization Using Irregular Cellular Automata," Computational Materials Science, **44**(2), pp. 566–576.

[206] Jin, Z., and Cui, Z., 2010, "Investigation on Strain Dependence of Dynamic Recrystallization Behavior Using an Inverse Analysis Method," Materials Science and Engineering: A, **527**(13–14), pp. 3111–3119.

[207] Jin, Z., and Cui, Z., 2012, "Investigation on Dynamic Recrystallization Using a Modified Cellular Automaton," Computational Materials Science, **63**, pp. 249–255.

[208] Chen, F., Cui, Z., Liu, J., Zhang, X., and Chen, W., 2009, "Modeling and Simulation on Dynamic Recrystallization of 30Cr2Ni4MoV Rotor Steel Using the Cellular Automaton Method," Modelling and Simulation in Materials Science and Engineering, **17**(7), p. 75015.

[209] Chen, F., Cui, Z., Liu, J., Chen, W., and Chen, S., 2010, "Mesoscale Simulation of the High-Temperature Austenitizing and Dynamic Recrystallization by Coupling a Cellular Automaton with a Topology Deformation Technique," Materials Science and Engineering: A, **527**(21–22), pp. 5539–5549.

[210] Chen, F., and Cui, Z., 2012, "Mesoscale Simulation of Microstructure Evolution during Multi-Stage Hot Forging Processes," Modelling and Simulation in Materials Science and Engineering, **20**(4), p. 45008.

[211] Chen, F., Qi, K., Cui, Z., and Lai, X., 2014, "Modeling the Dynamic Recrystallization in Austenitic Stainless Steel Using Cellular Automaton Method," Computational Materials Science, **83**, pp. 331–340.

[212] Qian, M., and Guo, Z. X., 2004, "Cellular Automata Simulation of Microstructural Evolution during Dynamic Recrystallization of an HY-100 Steel," Materials Science and Engineering: A, **365**(1–2), pp. 180–185.

[213] Hallberg, H., Wallin, M., and Ristinmaa, M., 2010, "Simulation of Discontinuous Dynamic Recrystallization in Pure Cu Using a Probabilistic Cellular Automaton," Computational Materials Science, **49**(1), pp. 25–34.

[214] Goetz, R., 2005, "Particle Stimulated Nucleation during Dynamic Recrystallization Using a Cellular Automata Model," Scripta Materialia, **52**(9), pp. 851–856.

[215] Kugler, G., and Turk, R., 2004, "Modeling the Dynamic Recrystallization under Multi-Stage Hot Deformation," Acta Materialia, **52**(15), pp. 4659–4668.

[216] Xiao, N., Zheng, C., Li, D., and Li, Y., 2008, "A Simulation of Dynamic Recrystallization by Coupling a Cellular Automaton Method with a Topology Deformation Technique," Computational Materials Science, **41**(3), pp. 366–374.

[217] Ding, R., and Guo, Z. X., 2001, "Coupled Quantitative Simulation of Microstructural Evolution and Plastic Flow during Dynamic Recrystallization," Acta Materialia, **49**(16), pp. 3163–3175.

[218] Gao, W., Belyakov, a., Miura, H., and Sakai, T., 1999, "Dynamic Recrystallization of Copper Polycrystals with Different Purities," Materials Science and Engineering: A, **265**, pp. 233–239.

[219] Cram, D. G., Zurob, H. S., Brechet, Y. J. M., and Hutchinson, C. R., 2009, "Modelling Discontinuous Dynamic Recrystallization Using a Physically Based Model for Nucleation," Acta Materialia, **57**(17), pp. 5218–5228.

[220] Ding, H., Liu, L., Kamado, S., Ding, W., and Kojima, Y., 2009, "Investigation of the Hot Compression Behavior of the Mg–9Al–1Zn Alloy Using EBSP Analysis and a Cellular Automata Simulation," Modelling and Simulation in Materials Science and Engineering, **17**(2), p. 25009.

[221] Liu, X., Li, L., He, F., Zhou, J., Zhu, B., and Zhang, L., 2013, "Simulation on Dynamic Recrystallization Behavior of AZ31 Magnesium Alloy Using Cellular Automaton Method Coupling Laasraoui–Jonas Model," Transactions of Nonferrous Metals Society of China, **23**(9), pp. 2692–2699.

[222] Yin, H., and Felicelli, S. D., 2009, "A Cellular Automaton Model for Dendrite Growth in Magnesium Alloy AZ91," Modelling and Simulation in Materials Science and Engineering, **17**(7), p. 75011.

[223] Wu, C., Yang, H., and Li, H., 2013, "Modeling of Static Coarsening of Two-Phase Titanium Alloy in the A+β Two-Phase Region at Different Temperature by a Cellular Automata Method," Chinese Science Bulletin, **58**(24), pp. 3023–3032.

[224] Zhang, Y., Jiang, S., Liang, Y., and Hu, L., 2013, "Simulation of Dynamic Recrystallization of NiTi Shape Memory Alloy during Hot Compression Deformation Based on Cellular Automaton," Computational Materials Science, **71**, pp. 124–134.

[225] Sakai, T., and Jonas, J. J., 1984, "Dynamic Recrystallization: Mechanical and Microstructural Considerations," Acta Metallurgica, **32**(2), pp. 189–209.

[226] Mirzadeh, H., Roostaei, M., Parsa, M. H., and Mahmudi, R., 2015, "Rate Controlling Mechanisms during Hot Deformation of Mg–3Gd–1Zn Magnesium Alloy: Dislocation Glide and Climb, Dynamic Recrystallization, and Mechanical Twinning," Materials & Design, **68**, pp. 228–231.

[227] Sakai, T., Akben, M. G., and Jonas, J. J., 1983, "Dynamic Recrystallization during the Transient Deformation of a Vanadium Microalloyed Steel," Acta Metallurgica, **31**(4), pp. 631–641.

[228] Roberts, W., and Ahlblom, B., 1978, "A Nucleation Criterion for Dynamic Recrystallization during Hot Working," Acta Metallurgica, **26**, pp. 801–813.

[229] Takeuchi, S., and Argon, A. S., 1976, "Steady-State Creep of Single-Phase Crystalline Matter at High Temperature," Journal of Materials Science, **11**(8), pp. 1542–1566.

[230] Asghar, S. A., Mousavi, A., and Bahador, S. R., 2011, "Investigation and Numerical Analysis of Strain Distribution in the Twist Extrusion of Pure Aluminum," JOM, **63**(2), pp. 69–76.

[231] Davis, J. R., 1990, *Properties and Selection: Nonferrous Alloys and Special-Purpose Materials*, ASM International.

[232] Holt, J. M., Mindlin, H., Ho, C. Y., University., P., and Synthesis., C. for I. and N. D. A. and, 1997, *Structural Alloys Handbook*, CINDAS/Purdue University, West Lafayette, Ind., Ind.

[233] Frost, H. J., and Ashby, F., 1982, *Deformation-Mechanism Maps: The Plasticity and Creep of Metals and Ceramics*, Pergamon Press, Kidlington, Oxford, United Kingdom.

[234] Shen, N., Samanta, A., Ding, H., and Cai, W. W., 2016, "Simulating Microstructure Evolution of Battery Tabs during Ultrasonic Welding," SME Journal of Manufacturing Processes, **23**, pp. 306–314.

[235] Cai, W., Blau, P. J., and Qu, J., 2013, "Friction Coefficients of Battery Metals and the Usage in Ultrasonic Welding Simulations," Electric Vehicle Symposium and Exhibition (EVS27), 2013 World, pp. 1–10.

[236] ABAQUS, 2014, "Inelastic Mechanical Properties," *Abaqus Analysis User's Guide*, Dassault Systèmes.

[237] Wu, T., Wu, Y., and Cai, W. W., 2012, *Ultrasonic Welding Attributes Measurement for Battery Tabs Joining (MSR-402)*.